NUCLEAR SPIN DETECTION AND OPTICAL PUMPING IN SEMICONDUCTOR QUANTUM DOTS

A DISSERTATION
SUBMITTED TO THE DEPARTMENT OF PHYSICS
AND THE COMMITTEE ON GRADUATE STUDIES
OF STANFORD UNIVERSITY
IN PARTIAL FULFILLMENT OF THE REQUIREMENTS
FOR THE DEGREE OF
DOCTOR OF PHILOSOPHY

Jonathan R. Goldman
September 2005

I certify that I have read this dissertation and that, in my opinion, it is fully adequate in scope and quality as a dissertation for the degree of Doctor of Philosophy.

Yoshihisa Yamamoto Principal Adviser

I certify that I have read this dissertation and that, in my opinion, it is fully adequate in scope and quality as a dissertation for the degree of Doctor of Philosophy.

David Goldhaber-Gordon

I certify that I have read this dissertation and that, in my opinion, it is fully adequate in scope and quality as a dissertation for the degree of Doctor of Philosophy.

Daniel Rugar
(IBM Almaden Research Labs)

Approved for the University Committee on Graduate Studies.

Abstract

Quantum memory devices and scalable quantum computers are important objectives of current research efforts. Quantum computers promise to solve certain problems which are intractable on classical computers and may provide insight into unanswered questions in computational theory. Quantum memory would provide coherent storage of a 'qubit' and could be used in conjunction with a quantum computer or in a quantum communication system. Both systems require a way of preparing qubits in a known state, a mechanism for measuring their states and addressing capability. Nuclear spins within a solid-state system have been proposed as one means for realizing a quantum computer. The preparation of nuclear spins in a known state and qubit readout remain a formidable challenge. Quantum dots provide a means of polarizing and measuring nuclear spins. We have observed the energy level shifts due to the nuclear spins in InAs quantum dots and we have measured the timescale for nuclear polarization to develop.

Quantum dots are nano-scale regions of a small band-gap semiconductor embedded in a larger band-gap semiconductor which can trap a single electron-hole pair or exciton. The energy levels for the exciton are quantized and are affected by many parameters including hyperfine interactions with the nuclei from the lattice. There are between 10^4 and 10^5 nuclei within the dot and it is possible through optical pumping to align the nuclear spins in one direction. We can also use the interaction of the nuclear spins with the exciton to determine the average nuclear spin direction. Future work in this area may ultimately lead to useful applications for nuclear spins in the area of quantum information processing devices.

In this thesis I will present results demonstrating nuclear polarization in InAs

quantum dots. In addition, I will present background material and experimental details with the basic goal that a reader of this thesis could reproduce the results we have obtained. There is also a theoretical discussion in which I present a model for the nuclear polarization process and compare the predicted timescales to the measured results. I will also discuss some work I carried out using sculpted ferromagnets with the goal of creating large magnetic field gradients. Such devices could be used in conjunction with quantum dots in order to do atomic plane imaging as discussed in Chapter 9. Chapter 4 provides a background to the discussion regarding magnetic field gradient calculations.

Preface

Quantum Computer
A Beautiful Creation
Spins flip or we flop

Acknowledgments

There are many people who I would like to thank for their kindness and support. First, I would like to thank my advisor, Professor Yoshihisa Yamamoto for providing me with the opportunity to work on a subject matter I find so interesting. Over the past seven years he has given me the freedom to pursue on a variety of projects and at the same time also guided me towards those projects which will have a greater impact within the community.

I would like also like to thank my committee members, Professors Yoshihisa Yamamoto, David Goldhaber-Gordon, Daniel Rugar, Jelena Vuckovic, and Mark Brongersma for attending my defense and for the first three for their feedback on my written thesis. I would also like to thank Professors Goldhaber-Gordon and Rugar for the valuable advice and encouragement they have given me. In particular Dr. Rugar spent considerable time advising me about how to build a magnetic resonance force microscope (MRFM) which I spent about 1-2 years on. Prof. Goldhaber-Gordon, who I have known since our days at MIT, has provided me with encouragement with my research and recently pushed that I focus on the timescale measurements of nuclear polarization in quantum dots.

The results reported in this thesis were performed using MBE samples grown by Bingyang Zhang and Glenn Solomon. Without these samples and the expertise they provided none of this work would have been possible. Fortunately, I never had to wait for samples while carrying out my research as I had plenty of wafers with quantum dots to work with. I was also fortunate to carry out my research at Stanford University and Nippon Telegraph and Telephone (NTT) where there exist extensive resources and support for fabrication and clean room processing. In

particular the Stanford Nanofabrication Facility (SNF), supported in part by the National Science Foundation's National Nanotechnology Infrastructure Network, has extensive equipment and expertise that assisted me in developing my process. I would like to thank the kind support of the SNF staff including Margaret Prisbie, Paul Jerabek, Mary Tang, Mahnaz Mansourpour, James Conway, Uli Thumser, Mario Vilanova and Maurice Stevens. In addition, Eric Perozziello, helped me understand various processing techniques and reminded me of how to use various equipment in the wee hours of the night. Rohit Shenoy, who did is PhD in Electrical Engineering, was very knowledgeable about the Hitachi HL-700F Electron Beam Lithography Machine and helped me perform multi-layer lithography with alignment on a rather ancient tool. Without his knowledge and assistance it would have taken much longer to make my devices. Kai-Mei Fu and Na Young Kim were also invaluable in helping me with my work in the lab and in particular Kai-Mei helped me become comfortable with the Raith 150 E-Beam Lithography System where the later devices were fabricated. I am also indebted to the kind help of Myles Steiner and Bob Hammond from the Kapitulnik-Geballe-Beasley (KGB) group, who kindly allowed me to use their metal deposition chamber when no one else on campus was willing. I used their chamber almost 10 times to deposit dysprosium over the past 7 years on various samples and without their generosity I could not have made any progress on the creation of large magnetic field gradients using sculpted ferromagnets.

I would also like to thank Tom Carver in the Ginzton clean room for doing many depositions for me and on short notice and with time pressure. He, too, had years of wisdom with processing and from our numerous discussions I learned a lot about processing and to solve the puzzles of which steps in a process are leading to the undesirable outcome. Finally, I would like to thank Tim Brand in the Ginzton Crystal Shop for his help in a number of areas. Although I did not pursue a MRFM he machined a beautiful sample holder out of quartz that included a novel optical fiber alignment system. Recently, he helped me find a suitable wax to use for mounting my quantum dot samples to glass handle wafers that would withstand the harsh acid etch I did to remove the substrate. He had a lot of expertise and I came to appreciate yet another aspect of sample preparation and processing.

I would also like to thank Jungsang Kim and Aykutlu Dana, former group members, who early on in my PhD served as a mentors for clean-room processing techniques and helped me think about the design of scientific apparatus. The design of an experimental setup has been an area I enjoy and their expertise was invaluable as began my work at Stanford. As I worked on various projects I frequently had to design and machine all sorts of parts and I owe many thanks to the Karlheinz Merkle, John Kirk, Mehmet Solyali, and Matthew Chuck from the Physics Machine Shop. Each of them helped me become a more efficient machinist and a better designer of parts. I spent many days discussing and designing parts with help from each of them. They have been good friends as well and I really enjoyed visiting the shop.

Charles Santori was instrumental with my recent projects in quantum dot spectroscopy. He had both hands-on knowledge and deep physical intuition and from him I learned a lot about physics and optics. I think that without his assistance I would have been lost. I learned a lot from other group members and I want to thank Kai-Mei Fu, Anne Verhulst, Hui Deng, David Fattal, and Gregor Weihs for all their help and patience. Fumiko Yamaguchi, a researcher in our group, was my first mentor and over the years has been a source of encouragement and advice and I really enjoyed the many discussions we have had. I also would like to thank Thaddeus Ladd who joined the group with me at the same time and over the years was a constant source of ideas and we had many useful discussions about physics and I think from him I learned a lot of theory. Cyrus Master and Will Oliver, also have been friends and office-mates who have kept the experience enjoyable and entertaining. Stephan Gotzinger, Patrik Recher, and Masayuki Shirane are all recent visitors to our group who I have enjoyed working with and have been wonderful friends. Masa and I built the initial timing system for controlling the pump polarization and I really enjoyed working with him. The rest of the Yamamoto group and visitors over the years have provided useful feedback and assistance over the years. Finally, I want to thank Shinichi Koseki and Wenzheng Yao who made the last month of data collection a wonderful experience. We devised some very useful experiments and together we created a team for collecting, processing and interpreting the data. I think without this arrangement my PhD would have take much more time and for me this was one of the best experiences

during the course of my PhD.

I want to thank all the support staff whose kindness I friendliness made the work environment so pleasant. In particular, Yurika Peterman was so instrumental in keeping the group running and in some many ways was so kind to me. Mayumi Hakkaku and Rieko Sasaki were also very helpful and kind to me while I was in the group. I also want to thank Maria Frank from the physics department who shepherded me through the graduation process and who quickly helped me out whenever I needed it.

I also want to thank Allan Bracker and Dan Gammon at the Naval Research Lab who spent a number of hours answering my questions and talking to me in person over the phone about nuclear polarization in semiconductor quantum dots. Their assistance in July 2005 helped me confirm my understanding and further develop the model I used for nuclear polarization in InAs quantum dots.

I want to thank all my friends at Stanford and outside who made the experience enjoyable. I also want to thank my parents and family for their continued support of my interests. Both my mother and father in different ways shaped my interest in math and science. In addition, my grandfather received his PhD in physics and served as an inspiration to me. It is also interesting to note how connected the community is–he worked with Albert Overhauser whose discovery for bulk systems is reproduced in this thesis on semiconductor quantum dots. I also want to thank my wife, Anuranjita Tewary, who has always been supportive and caring. Our relationship developed while in graduate school and I could not imagine this experience without her. Anu's parents and her sister's family have been very warm and I feel fortunate to have their and all of our family's support.

Contents

Abstract **v**

Preface **vii**

Acknowledgments **viii**

1 Introduction **1**

1.1 Quantum Information Processing 2

1.1.1 Implementation of Quantum Computers 2

1.2 Quantum Memory 6

1.3 Fundamental Physics 6

1.3.1 Decoherence 7

1.3.2 Nuclear Magnetic Ordering 7

1.3.3 Physical Processes within semiconductor quantum dots 8

2 Physics of Quantum Dots **9**

2.1 Quantum Confinement & Envelope Wavefunction 11

2.2 Coulombic Interaction 12

2.2.1 Exchange Splitting 13

2.3 Charge States 13

2.4 Zeeman Hamiltonian 15

2.4.1 Faraday Geometry 16

2.4.2 Voigt Geometry 18

2.5 Hyperfine Structure 20

2.5.1 Diamagnetic Shift 20
2.5.2 Bloch Wavefunction 21
2.5.3 Overhauser Effect 21
2.5.4 Ionicity and Nuclei-Electron Wavefunction Overlap 28
2.5.5 g-factor 29

3 Nuclear Spin Dynamics 32
3.1 Fermi's Golden Rule 33
3.2 Nuclear Polarization Rate 34
3.3 Nuclear Depolarization 37
3.4 Rate equations 38
3.5 Charged States 40
3.6 Nuclear Magnetic Resonance 40
3.6.1 Nano-NMR in quantum dots 41
3.6.2 Quadrupole Effects 41
3.6.3 Strain in Quantum Dots 41

4 Magnetic Field Gradient Generation 43
4.1 Introduction 43
4.2 Design Considerations 43
4.3 Magnetic Field Calculation 46
4.4 Magnet Designs 50
4.4.1 1-dimensional quantum computer with a field gradient in one dimension: Type I 50
4.4.2 2-dimensional and 1-dimensional quantum computers with field gradients in 2 dimensions: Types II & III 53
4.5 Edge Fluctuations 62
4.6 Conclusion 65

5 Instrumentation And Experimental Setup 66
5.1 SQUID measurement 67
5.2 NMR Magnet Setup 67

5.2.1 Variable Temperature Insert (VTI) . . . 71
5.2.2 Sample Holder . . . 72
5.2.3 Optical Setup . . . 72
5.2.4 Variable Field Access . . . 74
5.3 Spectromag Magnet System . . . 77
5.3.1 Sample Holder . . . 78
5.3.2 NMR coil . . . 78
5.4 Optical Instrumentation . . . 78
5.4.1 Photoluminescence Setup . . . 78
5.4.2 Titanium-Sapphire Laser . . . 79
5.4.3 Monochrometer and Detection . . . 81
5.4.4 Polarization Optics . . . 81
5.4.5 Polarization Optics . . . 82
5.4.6 Timescale Measurements . . . 83

6 Fabrication **85**
6.1 Quantum Dot Creation . . . 85
6.1.1 Molecular Beam Epitaxy (MBE) . . . 85
6.1.2 Isolation . . . 87
6.2 Magnet Fabrication . . . 90
6.2.1 Electron Beam Evaporation . . . 90
6.2.2 Lift-off Process . . . 92
6.3 Clean Room Processing . . . 92

7 Magnetophotoluminescence of Quantum Dots **95**
7.1 Sample Spectra for Faraday Geometry . . . 95
7.2 g-factor variation . . . 98
7.3 Diamagnetic Shift . . . 98
7.4 Voigt Geometry . . . 99
7.5 Quantum dots with magnets . . . 99
7.5.1 Faraday orientation . . . 100
7.5.2 Voigt orientation . . . 103

7.6 Blinking and Spectral Stability 110

8 Optical Pumping Measurements 112

8.1 Measurements 112

8.1.1 Typical Results 113

8.1.2 Expected Shift 114

8.1.3 Power Dependence of observed shift 115

8.1.4 Resonant Excitation 119

8.2 Time-scale measurements 120

8.2.1 Polarization Timescale Measurement I 121

8.2.2 Polarization Timescale vs. Laser Pump Power 123

8.2.3 Polarization Timescale vs. External Magnetic Field 123

8.2.4 Polarization Timescale Measurement II 124

8.2.5 Relaxation/Diffusion Timescale 125

8.3 Nuclear magnetic Resonance 126

8.3.1 Past NMR efforts 126

8.3.2 Problems with RF 129

8.4 Trion States 132

8.4.1 Nuclear Polarization 132

8.4.2 Summary of Timescale Behavior 132

9 Future Directions 141

9.1 Interferometer 141

9.2 Increased Collection Efficiency 141

9.3 Feedback Stabilization 142

9.4 5-layer structure 144

9.5 GaP quantum computer 145

9.6 Magnetic Resonance Force Microscopy 145

9.7 Nanowires 145

10 Conclusions 148

A Fluorapatite based quantum computer **150**
A.1 Introduction 150
A.2 Decoupling and Quantum Logic 153
A.3 Candidate Crystalline Systems 154
A.4 Initialization and achieving an low spin temperature 155
A.5 Field Gradient 156
A.6 Readout 156
A.7 Scalability 158
A.8 Summary 159

B Matlab Rate Equation Code **160**

Bibliography **165**

List of Tables

2.1 Values for gyromagnetic ratio and isotope abundance 25
2.2 Values for A, A_{eff} and β^* and the equivalent magnetic fields 28
2.3 Ionicities for III-V semiconductors 28
2.4 Lattice constants for GaAs and InAs. 29
2.5 Wavefunction overlap for various III-V semiconductors 29

List of Figures

2.1 This figure shows the various effects on the fine structure of the excitons energy levels. The exciton itself is created by exciting an electron from the valence band into the conduction band. This energy difference, or the bandgap, is 1.52eV for GaAs and between 1.3 and 1.44eV for InAs. The first effect diagrammed is the quantum confinement of a particle in a box. Then, the first correction is electostatic attraction between the electron and hole which reduces the energy of the lowest occupied excitonic level by ∼10-20 meV. An exchange interaction, $\delta_0 \sim 100\mu$ev, splits the excitonic levels into bright and dark excitons. In addition, due to dot asymmetry, these states split further. Finally, the application of magnetic field further moves the levels. Interaction between the trapped electron spin and the nuclear spin can be considered a manifestation of magnetic field, but in the diagram here it is given the label of hyperfine coupling. 10

2.2 This diagram shows the different particle-complexes that can exist in the quantum dot. Included are the single exciton, X^0 which traps a single electron and hole. The X^- and the X^+ correspond to single charge states which include an excess electron and hole respectively. In addition, the neutral biexciton state, XX^0 can occur under large pump powers. 14

2.3 This schematic shows the band structure of the quantum dot, wetting layer and the surrounding GaAs semiconductor and pure InAs [1]. The energies shown are the numbers associated with low temperature operation near 4 K. Typically, the emitted light from radiative exciton recombination correspons to between 1.3 and 1.44 eV. 15

2.4 This diagram depicts the convention for the g-factor and shows which direction the energy levels shift for $g_e < 0$ and $g_h < 0$. Also, here the exciton states $|+1\rangle$ and $|-1\rangle$ are shown. For example, the state $|+1\rangle$ corresponds to a transition between a conduction state with angular momentum (all from spins) of $-1/2$ and a valence state with total angular of $-3/2$. In order to conserve angular momentum a photon (σ_+) with angular momentum of $+1$ is emitted. The exciton state can also be described by the state of the electron and the hole, where the hole has opposite the angular momentum to what the electron has when it relaxes to the valence band. 17

2.5 This plot shows the Zeeman levels in the Faraday configuration, including the bright and dark states for $g_{e,z} = -1.5$ and $g_{h,z} = -0.5$. . . 19

2.6 This figure shows the bandgap for $In_{1-x}Ga_xAs$ and the corresponding wavelength. 31

4.1 Shown are three different forms of quantum computers using nuclei in crystal lattices. The circles represent the nuclei and the shading identifies the Zeeman energy. **a**) Type 1: The quantum computer lies in one dimension with a plane of equivalent qubits which have identical shading. Interactions are meant to occur only along the dashed lines shown. **b**) Type II: This design has a 2-dimensional field gradient and therefore distinct qubits along 2 dimensions. The interactions among distinct qubits as meant to be limited to the dashed lines. The requirement that their be no overlap in the Zeeman energies in the distinct qubits is shown by the anisotropic shading of the two gradient directions. In this design a single nuclei can interact with 4 neighboring or more if next-nearest neighbors are also considered. **c**) Type III: This design is identical to Type II but by use of the proper pulse sequence only the interactions along one dimension are permitted, as shown by the dashed lines. 45

4.2 A single crystal situated near a 2-dimensional anisotropic field gradient creates a distribution of frequencies as shown in the first line. The larger field gradient separates the qubits into groups whose centers could be separated by 100 kHz, for example. Within each group the smaller field gradient will separate quantum bits by an order of magnitude less or smaller (e.g. 10 kHz). With the proper pulse sequence the quantum computer labeled β could be the operational computer while the remaining qubits are decoupled entirely. The last line shows how the qubits experience frequency shifts due to dipole couplings with nearest neighbors; These shifts serve as the basis for logic operations in crystalline systems [2]. 47

4.3 A single dipole is shown to be aligned along the z-axis. The standard spherical coordinates r and θ are used. To calculate the field due to a rectangular slab of material one integrates this expression along the 3 dimensions, as shown. 49

4.4 A long, thin slab of material is placed in an external field as shown. The sample is placed at $z \sim 0$ and the gradient is along the x-axis. In this realization of the Type I configuration the yz-plane houses equivalent qubits. 51
4.5 For a design with $L = 3\mu$m, and $W = 0.3\mu$m, one can achieve a field gradient of ~ 1 T/μm for over a 1 micron distance. 53
4.6 This plot shows the inhomogeneity for the 1-dimensional configuration described in Fig. 4.5 at different x positions and as functions of the z-coordinate. The plots show that 10 ppm homogeneity can be achieved over a 0.02 μm range. 54
4.7 W, and L are the dimensions which characterize the cross-section of magnet and (x_o, z_o) locate the center of the quantum computer (Note, drawing is not to scale). The change in shape and shading is meant to show the change in the Zeeman energy. 56
4.8 Two identical magnets are aligned as shown and the crystal is placed between the magnets. S is the spacing between the magnets and is typically much less than W. Again the shapes and shading are meant to show an anistropy in the field gradients. 57
4.9 For the design drawn in Fig. 4.7 the field and gradient are plotted versus x with $W = 10$ μm and $L = 0.1$ μm. Here z_0 is chosen to be 0.3 μm. 58
4.10 This plot shows the field and gradient along the z axis for the parameters desribed in Fig. 4.9. x_0, shown in Fig. 7, is chosen to be 5.03 μm. 59
4.11 Using two magnets side-by-side as shown in Fig. 8 one can get enhanced field gradients. With $W = 10$ μm, $L = 0.1$ μm, $x_0 = 5.35$ μm and S, the spacing, set to 0.5 μm a field gradient along z can be made to be small if the crystalline nuclei are situated near $z = 0$. 60
4.12 This plot shows the field gradient along x for the design described in Fig. 4.8 and with parameters listed in Fig. 4.11. z_0 is set to 0, and thus one can get gradients on the order of 20 T/μm. 61

4.13 The geometry considered for calculating the effect of imperfections in the physical edge. The edge is modelled with some sinusoidal oscillation of wavelength λ, and amplitude A_o. Spectral linewidths are determined by creating a histogram in the distribution of Zeeman energies for equivalent spins situated at coordinates (x_o, z_o) as shown in Fig. 4.7. The circles along the y-axis represent the equivalent qubits whose Zeeman energies are calculated. 63

4.14 Shown is the inhomogeneity in ppb as a function of z for a 1 nm and 10 nm and amplitude fluctuation. The chosen design has $\lambda = 1$ μm, $W = 10$ μm, $L = 0.1$ μm, $D = 200$ μm and $x_0 = 5.03\mu$m. 64

5.1 This photograph shows a fabricated micromagnet of dysprosium. Above the dysprosium we covered the sample with polyamide and an layer of patterned aluminum. The purpose of the aluminum was to use NMR to measure the effect of the dysprosium magnet and in this way determine if a field gradient was present. This experiment revealed that the aluminum nuclei were too broadly distributed to provide a NMR signal. 68

5.2 Dysprosium magnetization vs temperature and magnetic field. The dysprosium magnetization reaches near saturation ($\sim$350 emu/g) for microfabricated dysprosium. 69

5.3 7 T NMR magnet made by Oxford Instruments. We installed an optical breadboard below the magnet to mount the necessary optics. Aluminum supports screwed into holes on the bottom of the magnet. The laser and monochrometer are located on a standard optical table and all the light to and from those equipment are fiber coupled. 70

5.4 This photograph shows the modified sample holder that allowed us to probe the sample in the Voigt configuration. The 45^o portion had a mirror mounted on it and the sample can be seen mounted on the vertical slab. Also note the wires lead to the hall probe which was mounted on the back of the bottom circular plate. 73

5.5 Working distance for this system totaled 65mm. The inserted photograph shows the bottom of cryostat with the windows and the sample located in the center region. The lens we used was attached to a lens-tube which then was mounted on a sturdy XYZ stage. 75

5.6 This photograph shows the optical breadboard attached to the bottom of the 7T NMR magnet 76

5.7 This is the Spectromag magnet. Ours is a maximum of 11.5 T magnet. The coils are located in the bottom portion and the upper portion houses a the liquid nitrogen bath and the vacuum space. 77

5.8 Schematic showing optical setup. The laser light is reflected off a wedge and focused via the two lenses onto the sample. The PL is filtered from any scattered and reflected laser light and sent to a CCD camera from which we form an image or toward a monochrometer where it is dispersed. 80

5.9 By sending the laser through a polarizing beam splitter (PBS) the laser is split into horizontally (H) and vertically (V) polarized light. Each path of the split laser light has a shutter installed which is controlled with TTL pulses. The light is recombined on a non-polarizing beam splitter (NPBS). The light then passes through a quarter-wave plate which converts the H and V light to $\sigma_+$and σ_-light. The light entering the monochrometer also passes through an identical mechanical shutter also controlled by TTL pulses. 84

6.1 AFM images of InAs QDs grown on (100) GaAs substrate with 1.89ML InAs coverage by MBE at growth temperatures of (a) 475, (b) 482, (c) 505, and (d) 525. The growth rate of InAs QDs is 0.07ML/s, and ratio of As to In is about 50. The measured area is 1x1 μm^2. 88

6.2 This procedure diagrams the method we use to etch mesas for isolating a small number of quantum dots. 1) We coat the positive e-beam resist which we expose using electron beam lithography. After developing in the e-beam developer a region of the resist is removed. 2) We can deposit a thin layer of metal such as nickel which covers the entire wafer. After using acetone to perform lift-off the nickel that adhered directly to the wafer remains while the nickel that was deposited on the resist is removed. 3) We can now etch into the wafer and etch past the layer containing quantum dots except where the metal protects the substrate. We can subsequently remove the nickel with a nickel etch and we are left with isolated mesas with dimensions as small as 100nm X 100nm containing just a few quantum dots. 89

6.3 This diagram shows the major steps necessary to make an integrated device to introduce a magnetic field gradient across the quantum dot. 1) After obtaining a sample with suitable mesas we can deposit a buffer layer of SiO_2 using the STS chemical vapor deposition chamber. This layer can be of variable thickness and helps ensure that the quantum dots are located near the center of the void within the magnet. Also, it can help with providing a smooth surface on which deposit dysprosium (Dy). 2)Here we deposit sufficient magnetic material by evaporating Dy on to the wafer. An alternative is to sputter a material such as FeCo which would ensure better sidewall coverage. Sputtering heats the sample more and this could damage the sample. 3) Finally, we use wax to attach the wafer to a handle wafer such as quartz. Then we do a wet chemical etch as outlined below. The material that remains is very thin and the quartz is necessary to handle the sample without damaging the quantum dots. 91

7.1 This data shows typical spectra from a single quantum do as a function of magnetic field. The data are taken from 0 to 7T every 0.5T. The spectra clearly curve towards shorter wavelengths which is due to the diamagnetic shift. 96

7.2 This plot shows the splitting from the data in Fig. [?]. The data lie on a staight line and have a g_{eff}-factor of 152 μeV/T. This corresponds to a g-factor of -2.62 97

7.3 A histogram of the distribution of g-factors for the dots we have measured. This data can only tell us the effective g-factor, or $g_{e,z} + g_{h,z}$. If the dark states could be measured then it would be possible to determine the contribution from the electron and hole separately. The best way to do this is to apply the magnetic field slightly off a normal axis and this introduces a mixing of the bright and dark states. 99

7.4 This SEM shows a full view of a magnetic that capped a mesa containing quantum dots. The dysprosium metal deposited was 1μm thick and tremendous strain developed in this film causing it to curl. Also noticeable is what we believe is a dynamical shadow-masking effect. This is evident in the region of metal deposited around the edge. We believe that the magnet curled up while deposition was underway and after curling it acted as a mask for further material that was deposited directly onto the substrate. 100

7.5 The original intent of the experiment was to place micromagnetic material near to mesas containing quantum dots. This SEM shows a triangular magnetic structure we fabricated near the mesa. The mesa is the oval- shaped region and the triangular magnet is pointing toward the mesa. 101

7.6 The original intent of the experiment was to place micromagnetic material near to mesas containing quantum dots. This SEM shows a rectangular magnetic structure we fabricated near the mesa, which is the small mesa that appears whitish in the SEM micrograph. 102

7.7 The SEM shows a magnet with a region protruding out due to the mesa below. The mesa was roughly 0.5μm tall and with the magnet deposited on the mesa and surrounding region 103

7.8 This SEM shows the metal directly above the mesa was removed. This effect is due to a dynamical shadowmasking effect which cause the region above the mesa to form a mushroom-like cap. When we performed lift-off this small region of material was removed. This was not universal and roughly 50% of the structures had caps removed. With the cap removed it was possible to perform photoluminescence studies. . . 104

7.9 This simulation is for the Faraday geometry. Notice that the magnetic field is decreased inside the void region. The blue region is missing magnetic material while the surrounding yellow region contains dysprosium. 105

7.10 106

7.11 Simulation showing Voigt Simulation 107

7.12 Simulation showing Voigt geometry. Notice that hear the void has an increase in the magnetic field strength instead. This simulated result was confirmed by our experiments. 108

7.13 Here we observed that indeed the magnetic field produced by the void in the Voigt gemoetry was additive. This can be seen by finding the x-intercept of the lines drawn. At this point the observed Δ would be 0 and thus $B_{\mu m} = B_0$ and so we can extrapolate what $B_{\mu m}$ assuming that it does not change with external magnetic field, B_0. 109

7.14 These spectra are from a dot who we noticed had an unstable emission spectra. The spectra shown are 5 second acquisitions taken roughly every 5 seconds. The emission appears to be hoping around. It appears that the emission is mostly stable for a few seconds and then jumps but over a 5 second interval it doesn't jump much. In that case we would see many more doublets in each acquisition. 111

8.1 A typical PL spectrum under $\sigma_+$and σ_-pump polarization. These data was taken at 0.8 T. 113

8.2 This flow-chart shows the effect of the nuclear spins on the emitted photon energy for g_{eff} <0. If excitons are created in the wetting layer under σ_+illumination predominantly $|+1\rangle$ excitons are created. Thus the grey peaks shown have a large intensity for the $|+1\rangle$ state which is at larger energy or shorter wavelength. Hole spins can easily flip which leads to dark exciton population build-up in the wetting layer. Alternatively, the hole-spin can flip even while the dot is populated by a bright exciton state. In any event once the hole relaxes, there is a possibility for the nuclear spin and electron spin to exchange spin direction via a hyperfine process as discussed in Chapter 3. In the case of σ_+pumping the nuclei tend to become negatively polarized after repeated spin flips. Then if a $|+1\rangle$ is present in the dot the nuclei that are spin-down and the electron that is spin down lead to a net positive hyperfine interaction. This means that the higher energy peak blue-shifts. Alternatively, if a $|-1\rangle$ exciton is trapped in the dot the hyperfine interaction is negative and thus it red-shifts. In summary the peaks become further separated under σ_+illumination. We can go through a similar analysis for pumping under σ_-polarization which leads to a compression of the peaks. Also note the longer wavelength peak, associated with the $|-1\rangle$ exciton state is dominant in this case. 116

8.3 For the case of $g < 0$ similar spectra are observed but instead the peaks compress for σ_+pumping. Also note that now longer wavelength peak (smaller energy) peaks is more prevalent due to the lower probability of electron spin-flipping events. Thus, the peaks shift and the dominant peak is the higher energy peak to the right. For the case of σ_-pumping the peaks move further apart and the shorter wavelength peak (higher energy) has a greater intensity. Thus, the spectrum are completely reversed. 117

8.4 This diagram provides an pictorial model for the nuclear polarization under σ_+pumping. The bright state is populated in the dot and then the hole spin relaxes which causes the exciton the relax to the $|-2\rangle$ state. A flip-flop processe occurs which causes the electron and nucleus to exchange spin directions and this leads to a change in the nuclear spin direction to be in the downward direction. The process of the electron-spin flip and simultaneous nuclear-spin flip does not conserve energy and so the process is virtual and called a spin-flip assisted radiative recombination. To conserve energy the emitted photon will have an increase or decrease in its energy corresponding to the energy mismatch between the $|-2\rangle$ and the $|-1\rangle$ state. The 118

8.5 Power dependence of Δ. Typically, we would run the experiment at laser powers of 1-3mW, which is below the saturated region. At higher laser power the emission from the quantum dot becomes more broadband and biexciton peaks begin to appear and eventually dwarf the single exciton peak. At large pump powers the total shift Δ approaches 0.09nm, which can be converted to a nuclear polarization of 10% for indium and 30% for arsenic. 119

8.6 A two-state model for the system. P_{ss} is the steady-state polarization and P_0 is the thermal equilibrium polarization. 120

8.7 These data were taken under wetting layer excitation (852nm). NOtice that the longer wavelength (lower energy) peak is dominant under σ_-pumping. Under $\sigma_+$the higher energy peak is more dominant but the asymmetry in the peak heights is quite pronounced. Comare this to Figure 8.8 121

8.8 These data were taken from the same dot shown in Figure 8.7 but instead the dot was pumped with the laser tuned to 875.6nm. Notice now that the peak asymmetry is more symmetric. That is, when the laser is set to σ_+mostly σ_+light is emitted and vice-versa and this "spin-conservation" exists relatively equally for both pump polarizations. . 122

8.9 Timing Diagram for laser pump polarization 123

8.10 Timing diagram to collect σ_+ photoluminescence. The shutters controlling the laser path that creates σ_+ is synchronized with shutter controlling the PL collected. 124
8.11 Timing diagram to collect σ_-photoluminescence. The shutters controlling the laser path that creates $\sigma_-$is synchronized to with shutter controlling the PL collected. 125
8.12 Plot of Δ vs. laser pump frequency f for dot located in mesa#1175 . 126
8.13 Plot of Δ vs. laser pump frequency f for multiple dots. 127
8.14 Plot of the dependence of the polarization timescale for different pump power condition 128
8.15 Plot of the dependence of the polarization timescale for different external magnetic field values. The laser pump power was kept constant for these measurements 129
8.16 Plot of the theoretical polarization timescale for different external magnetic field values. The laser pump power was kept constant for this model. An important point to note is that σ_+pumping always polarizes the nuclei faster than $\sigma_-$and this can be explained from the difference in the energy mismatch between the dark state and the bright state involved in the second-order recombination. The insert shows the energy dependence of the exciton states versus magnetic field 130
8.17 Snapshot of shift as it develops 131
8.18 This is the timing diagram for Polarization Timescale Measurement II. We either collect after the start of the σ_+laser pulse or the σ_-laser pulse. 132
8.19 A plot showing the peak evolution of the peaks under different pump polarization 135
8.20 A plot of Δ_{σ_+} vs. delay τ. 136
8.21 A plot of Δ_{σ_-} vs. delay τ. 136
8.22 Idea behind nuclear relaxation and spin decay 137
8.23 Relaxation timescale measurement timing diagram. 137
8.24 A plot of the raw data from the relaxation experiment with $T_w = (0.1s, 5s, 10s, 20s)$ 138

8.25 Charge State 139
8.26 Nuclear Relaxation/decay for charge state. This plot shows the peak splitting under σ_-pumping as a function of wait time according to Figure 8.23 140

9.1 5 Layer device 144
9.2 SEM showing the gold nanowires. 146
9.3 Field and Field gradient near a nanowire 147

Chapter 1

Introduction

Semiconductor quantum dots have proven useful for studying fundamental science-related questions of quantum mechanics and were recently shown to be useful for the generation of non-classical light [3, 4, 5]. Some types of quantum dots have been used in bio-labeling [6, 7] and are the basis for products offered by companies. Their continued usefulness to fundamental science and their future applications will likely grow. In this thesis we focus on two aspects of InAs (indium arsenide) self-assembled quantum dots: 1) their use as a magnetic field sensor and 2) the optical pumping of nuclear spins within a quantum dot and their interaction with a trapped electron spin.

The use of quantum dots as a means of exploring nuclear spin dynamics is of great interest for possible applications in quantum information processing. For quantum computing proposals using coupled electron spins in quantum dots the objective is to polarize all the nuclei within a dot and suppress their decoherence effects on the electron spin. For proposals using nuclear spins for quantum memory storage or for quantum computing, the interaction between the electron and the nuclear spins is a necessity. This chapter briefly reviews the interest in quantum memory and quantum computing, explores the magnetic field gradient requirements for solid-state nuclear spin quantum computing, and further motivates the interest in studying a small ensemble of nuclear spins.

1.1 Quantum Information Processing

The successful demonstration of a scalable quantum computer is the current focus of numerous research groups. Such a quantum computer could have profound impact on our understanding of computational theory and may lead to practical applications, such as faster database searching [8]. We have proposed an all-silicon based quantum computer based on nuclear spins in a solid state system [9] which we modeled after the a previous proposal for using nuclear spins in a solid [2]. Both of these proposals require that we have single nuclear-spin detection, optical pumping of nuclear spins, and large magnetic field gradients. The generation of large magnetic field gradients is a challenging engineering problem and a problem that I spent considerable effort in solving. The results of these efforts are presented in this thesis in Chapters 4 and 7.

Detecting a small number of nuclear spins and preparing them in a known initial state remains a challenge. For our proposal [9, 10] we rely on Magnetic Resonance Force Microscopy (MRFM) for nuclear spin detection. Another means of doing direct optical detection was proposed by our research group [11] and involves the use of impurity-bound excitons. The focus of my work was the use of semiconductor dots to probe the nuclear spin dynamics of a solid-state nuclear spin system via optical means. We performed experiments that demonstrate that we could polarize the nuclear spins and also measure the spin direction of the ensemble. Quantum dots are not as versatile a means for nuclear spin detection as MRFM but semiconducting systems can provide an alternative and more sensitive means of measuring nuclear spins. In addition, there are other uses for ensembles of nuclear spins besides quantum computing such as quantum memory [12]. Finally, the physics of the coupled exciton-nuclear spin system are not fully understood and the prospect of studying decoherence of a small number of nuclei ($\sim 10^5$) are additional motivating factors.

1.1.1 Implementation of Quantum Computers

There are many ideas for how to build a quantum computer and a discussion of all proposals would be overwhelming. A good overview of quantum computing from a

theoretical and experimental viewpoint is provided in Ref. [13]. Here we mention briefly the requirements for a quantum computer and some of the notable proposals that have seen experimental progress.

Qubit definition Before listing what the requirements are for building a quantum computer, let me first define a *qubit*. A qubit is a quantum bit of information which in a simple mathematical form can be written as

$$|\Psi\rangle = a\,|0\rangle + b\,|1\rangle \tag{1.1}$$

where $|a|^2+|b|^2 = 1$. A standard classical computational bit can only occupy a definite state such as 0 or 1. The ability of a quantum object to simultaneously occupy 0 and 1 is due to the quantum superposition principle. The actual meaning of the states $|0\rangle$ and $|1\rangle$ could correspond to the spin state of an quantum-mechanical object such as electron or nuclear spin. The requirements for some physical object to be a qubit or not merely superposition but also the ability to create entangled states such as the two-qubit state $\frac{|00\rangle+|11\rangle}{\sqrt{2}}$ which has no classical analog.

Extensive mathematical formalism has been developed [13] to show how qubits can be used to carry out useful computation. In fact, the tremendous scientific interest in quantum computers arises from the ability to solve apparently computationally intractable problems. This advantage arises from a qubit's ability to be in a superposition state and from entanglement with other qubits. There is also interest in using a network of qubits for simulation of a quantum system [14, 15].

Basic Requirements David DiVincenzo formulated 5 criterion [16] necessary for building a quantum computer:

1. A scalable physical system with well characterized qubits.

2. A universal set of quantum gates.

3. The ability to initialize the sate of qubits to a simple initial condition such as $|00\ldots0\rangle$

4. The ability to measure the state of qubits after a computation.

5. Long decoherence times so the system remains stable long enough to carry out a useful quantum computation.

This thesis focuses on items 3 and 4 but there is discussion in Appendix A regarding a proposal for one type of solid-state crystal. For a detailed discussion of how the systems we have proposed exhibits long decoherence times please see [17].

Implementations and Solid-State NMR There are several physical systems that have been considered as candidates for quantum computers. Among them are the nuclear spins in solution molecules [18, 19] and crystal lattices [2], cold trapped ions [20, 21], cavity QED [22, 23], photon gates [24, 25], and solid state devices including Josephson junctions [26, 27] and quantum dots [28, 29].

Nuclear spins appear to have the longest coherence time of all potential quantum bits ('qubits') in physical systems, since they are well isolated from their surroundings. Despite this longevity, computational power will be limited by the time needed to carry out logic operations [16]. Nuclei with spin 1/2 in crystals have been shown to be a viable system [2]. The regularity of the lattice ensures identical nuclear dipole coupling throughout the crystal and allows addressing of nuclear spins on the atomic scale if qubits can be distinguished.

Magnetic Field Gradient Generation A spatially varying magnetic field will ensure that nuclei at different locations have a unique Zeeman frequency of precession, given by $\omega = (g_I \mu_N/\hbar)\hat{\vec{I}} \cdot \vec{B}(\vec{r})$, where $\vec{\mathrm{I}}$ is the nuclear spin, g_I is the gyromagnetic ratio, μ_N is the nuclear Bohr magneton, and $\vec{B}(\vec{r})$ is the magnetic field at lattice position $\vec{r}$. The separation of different qubit's frequencies must be larger than the nearest neighbor nuclear-nuclear dipole coupling.

The Hamiltonian describing the magnetic dipole coupling between two neighboring nuclei of spin $\vec{I_1}$ and $\vec{I_2}$ separated a distance r is given by

$$\mathcal{H}_\mathrm{nd} = \mathcal{A}_\mathrm{nd}(r)[\vec{I_1} \cdot \vec{I_2} - 3(\vec{I_1} \cdot \hat{r})(\vec{I_2} \cdot \hat{r})], \tag{1.2}$$

where $\mathcal{A}_{\rm nd}(r) = -\mu_0 g_I^2 \mu_N^2 / 4\pi r^3$ is the nuclear dipole coupling constant between two nuclei. For neighboring nuclei separated by a distance a in a crystal, the coupling constant, $\mathcal{A}_{\rm nd}(a)$, divided by Plank's constant is on the order of 100 Hz for phosphorous nuclei in Cerium Phosphide (CeP), 5.4 kHz for fluorine nuclei in Calcium Fluoride (CaF_2), and is unlikely to be any larger for most crystalline systems [**?**]. A requirement for quantum computation is that the adjacent-nucleus frequency separation be large compared to the nuclear dipole coupling. A dimensionless measure of this, which will be denoted as η, is given by the frequency separation divided by the nuclear-nuclear dipole coupling in rad per second, $A_{nd}/\hbar$:

$$\eta = \frac{\triangle\omega}{A_{nd}/\hbar} = \frac{4\pi a^4 |\hat{\vec{I}}|}{\mu_N \mu_0 g_I} \frac{d|\vec{B}|}{dx}. \tag{1.3}$$

Here, the gradient is assumed to be along x and constant between two neighboring qubits.

As a lower limit, η should be larger than unity. For cystalline solids, this requires a minimum field gradient of more than 0.07 T/μm in CeP and more than 2 T/μm in CaF_2. The focus of Chapter 4 is to demonstrate that magnet designs exist which provide these demanding field gradients while also satisfying other constrains for successful implementation of quantum computation.

Optical Pumping of Nuclear Spins An important requirement for a quantum computer is condition 3 of the DiVincenzo criterion. This requirement means that we must prepare the nuclear spins in a well-known state. This can be challenging and in liquid-NMR based quantum computing effective pure states are used [30]. For a solid-state implementation initializing the nuclear spins has the advantage that we can introduce photo-excited spin-polarized electrons that interact via hyperfine coupling to the nuclear spins and transfer their nuclear polarization.

Nuclear Spin Detection Another requirement is the ability to readout a particular nuclear spin state. In a proposal we published [9] we make use of magnetic resonance force microscopy (MRFM) [31] which is a mechanical means of detecting

nuclear spins. Some discussion of its scaling limits and operation is provided in Appendix A. MRFM is an active area of research and much progress has recently been made [32, 33, 34]. An alternative approach for nuclear-spin detection is to use direct optical detection of impurity-bound excitons in a semiconductor [11] and there has been experimental progress in single nuclear-spin detection in other systems [35].

1.2 Quantum Memory

The ability to store a qubit for an extended period of time is also an important need for quantum information processing devices. For instance, long-lived quantum memory is necessary for some quantum computers. In addition, quantum communication could use quantum repeaters to extend the reach of quantum cryptographic systems [36]. Our research effort has focused on the use of nuclei as qubits and our original intention was to create a quantum computer from a network of coupled nuclear spins in a solid. However, recent work [12] has motivated the idea of using the collective excitations of nuclear spins within a dot to create a long-lived memory device for a quantum state.

1.3 Fundamental Physics

Beyond the possible applications that could arise from devices in which we can exert control at the quantum level there is motivation for this line of research based on fundamental science alone. This includes exploring fundamental questions of quantum mechanics as well as the possibility of observing novel phenomenon like phase transitions. In addition, the behavior of electrons and holes within semiconductor quantum dots and their interaction with nuclear spins are not fully understood and in and of itself it is an interesting research area. One very active area of research is work towards a single quantum dot laser and recently the use of quantum dots for doing cavity quantum electrodynamics (CQED) [37].

1.3.1 Decoherence

How a microscopic system which is governed by quantum mechanics behaves as it interacts with a macroscopic system described by classical systems is of tremendous interest. Decoherence of a coupled nuclear spin system has been studied at the macroscopic level extensively [17, 38]. This typically involves on the order of 10^{22} nuclear spins and 1 cm^3 samples. Within a semiconductor dot there are typically about 10^4 to 10^5 nuclear spins present. Decoherence in an ensemble of nuclear spins at the boundary between a macroscopic system and microscopic (the mesoscopic regime) is an interesting area. The vision for these sorts of experiments is to perform pulsed NMR experiment and use the optical output from the quantum dot to monitor the nuclear spin dynamics of the system.

1.3.2 Nuclear Magnetic Ordering

One example of particular interest is ferromagnetic order with a coupled nuclear spin system. This is an example of a phase transition and occurs routinely with ferromagnets such as iron, where the electrons spins in the outer orbitals become aligned.

Nuclear magnetic order has been observed but only using difficult experimental techniques involving ultra-low temperature equipment, ultra-high magnetic fields, and adiabatic demagnetization [39]. If sufficiently large nuclear polarization were reached within a semiconductor quantum dot then possibly the dynamics that govern this type of phase transition could manifest itself.

An important concept for considering nuclear magnetic ordering and for later discussion in regards to nuclear polarization is the spin temperature of the nuclear spin system. It is defined as follows

$$\frac{p_m}{p_{m-1}} = e^{\frac{\gamma\hbar H_0}{kT_s}} \tag{1.4}$$

where, p_i represent the various m_I sublevels for the nucler-spin states. For simplicity consider the case of $m = 1/2$. If all nuclei are in the ground state or namely $p_{1/2} = 1$

and $p_{-1/2} = 1$, then $T_s \to 0$. The concept of nuclear spin temperature has a useful meaning since spin-$\frac{1}{2}$ nuclei are decoupled from the phonons that define the actual temperature of the lattice. If we can introduce a nuclear polarization $p_m \gg p_{m-1}$ through some means (e.g. optical pumping), then the low spin temperature can induce phase transitions among the nuclear spins. For nuclear spins with $I > 1/2$, the interaction between the with phonons increases because the nuclear quadrupolar moment interacts with fluctuating electric field gradients induced by phonons. Nonetheless nuclear magnetic order and other nuclear cooperative phenomena have been observed in nuclear spin $I > 1/2$ as well [39]. At a microscopic level if the dipolar interaction among the nuclear spins is larger than the comparable energy associated with the nuclear spin temperature then this dipolar interaction can drive effects like ferromagnetic ordering. Thus, the spin temperature needs to be compared the dipolar interaction strength within a given crystal.

1.3.3 Physical Processes within semiconductor quantum dots

The mechanisms that govern hole and electron dynamics and their interactions with photons, phonons and nuclei is not fully understood. Exploring these phenomenon to fullest extent possible is not only desirable but may lead to a fuller understanding that can be extended to areas outside the perceived scope of its relevancy. Semiconductor quantum dots are a relatively new tool for exploring quantum phenomenon the rich physics surrounding them are likely to provide interesting research and hopefully useful devices.

Chapter 2

Physics of Quantum Dots

A quantum dot is the general term ascribed to a small semiconductor region that can trap a few electrons and holes. The dimensions of quantum dots can vary between just a few nanometers and a few microns and it can be defined artificially with electrodes or through a growth technique such as self-assembly. The focus of this thesis is self-assembled InAs semiconductor quantum dots whose growth is discussed in Section 6.1.1.

The term 'quantum' in quantum dot arises from the discrete energy levels that electrons and holes can occupy. The discretization can arise from the Coulombic interaction among the small number of electrons and holes within the dot or from the physical confinement of these particles in a small space. The Coulombic interaction varies as $1/r$ and dominates for larger dots while the quantum confinement varies as a $1/r^2$ and dominates for smaller dots, such as the ones considered in this thesis.

There are many effects to consider which effect the energy state of bound exciton within a dot. An overview of the energy perturbations on an quantum dot-bound exciton is shown in Figure 2.1. Each of these effects is discussed below and the associated parameters are defined.

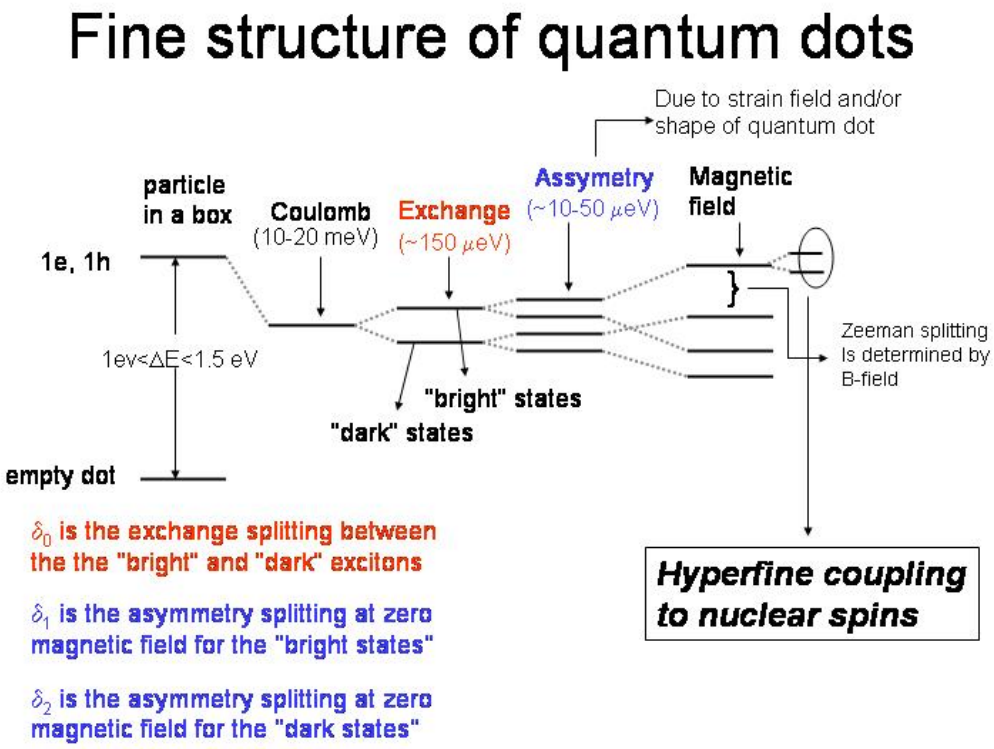

Figure 2.1: This figure shows the various effects on the fine structure of the excitons energy levels. The exciton itself is created by exciting an electron from the valence band into the conduction band. This energy difference, or the bandgap, is 1.52eV for GaAs and between 1.3 and 1.44eV for InAs. The first effect diagrammed is the quantum confinement of a particle in a box. Then, the first correction is electostatic attraction between the electron and hole which reduces the energy of the lowest occupied excitonic level by ∼10-20 meV. An exchange interaction, $\delta_0 \sim 100\mu$ev, splits the excitonic levels into bright and dark excitons. In addition, due to dot asymmetry, these states split further. Finally, the application of magnetic field further moves the levels. Interaction between the trapped electron spin and the nuclear spin can be considered a manifestation of magnetic field, but in the diagram here it is given the label of hyperfine coupling.

2.1 Quantum Confinement & Envelope Wavefunction

To a first approximation we consider the quantum dot to be a an attractive potential where an exciton (or electron-hole pair) can become localized. We can then solve either a particle in a box or a parabolic potential from which discrete energy levels arise. Both approaches have been used to describe the energy levels within a quantum dot. The actual envelope wavefunction can be calculated more precisely if the exact structure of the quantum dot is known [40, 41, 42, 43]. For a single particle (electron or hole) in a semiconductor the wavefunction is not just the envelope wavefunction which gives the distribution of where the electron is localized but also includes a periodic component $u(\vec{r})$, where $e^{i\vec{k}\cdot\vec{r}}u(\vec{r})$ is a Bloch wavefunction. The overall wavefunction of a particle with $\vec{k} = 0$ is given by

$$\psi(\vec{r}) = \Psi(\vec{r})u(\vec{r}) \tag{2.1}$$

Envelope Wavefunction For simplicity we will follow the convention of previous work [44, 3] where we assume the dots are bound by a parabolic potential in two dimensions (x and y) and an infinite square-well potential in the third dimension (z). In this case the potential is

$$V(\vec{r}) = \begin{cases} \frac{1}{2}m^*\omega_0(x^2+y^2) & |z| < L/2, \\ \infty & |z| > L/2, \end{cases} \tag{2.2}$$

where the height of the dot is L and ω_0 is the energy-level spacing between the different spatial states. Thus, following elementary quantum mechanics calculations for parabolic and square-well potentials we can write the energy states as

$$E = (n_x + n_y + 1)\hbar\omega_0 + \left(\frac{\pi^2\hbar^2}{2m^*L^2}\right)n_z^2 \tag{2.3}$$

Since L is very small ($\sim$ 5nm) it is often taken that only the state $n_z = 1$ is bound. Thus ω_0 is the spacing between levels and is found to be about 30-80 meV for our

InAs self-assembled dots. The envelope wavefunction is then

$$\Psi(r) = H_{n_x}(x)H_{n_y}(y)e^{-\frac{1}{2}\frac{m^*\omega_0}{\hbar}(x^2+y^2)}\cos\frac{\pi z}{L} \tag{2.4}$$

where H_n are Hermite polynomials.

Valence bands The atomic orbital function, $u(\vec{r})$, of the electrons in the conduction band have s-like symmetry and so we only have to consider this single conduction band. However, the valence band, which contains the holes, includes atomic orbitals that can be s-like and p-like. The bands are called the heavy, light, and split-off bands which in principle can mix. Valence band theory is discussed in detail in [45]. For quantum dots, and in particular InAs quantum dots, strain is present which separates the light-hole band from the heavy-hole band by at least several tens of meV. Thus, it is often neglected in the analysis. The split-off band, which arises from spin-orbit coupling is separated from the other bands even in bulk unstrained semiconductors and can be neglected in the analysis of the quantum dot energy levels.

2.2 Coulombic Interaction

Up until now we considered the exciton a single particle trapped in a 3-dimensional square potential or 3-dimensional harmonic potential which are solvable. Of course the exact solution for any particular dot depends on the distribution of atoms and shape of the quantum dot. Once this is solved the first correction to make is the Coulombic interaction between the constituent parts: namely the Coulombic attraction between the electron and hole. This leads to reduction in the energy levels since the Coulombic interaction, V_C, is negative due to the opposite sign of the charges on the electron and hole. In general the Coulomb potential between two charge Z_1e and Z_2e separated a distance r is given by:

$$V(r) = -\frac{Z_1Z_2e^2}{\epsilon r} \tag{2.5}$$

where ϵ is the dielectric constant. With $Z_1 = 1$ and $Z_1 = 1$ we can write the direct term of the Coulombic interaction between a hole and electron as

$$H^{dir} = \int d^3\vec{r} \int d^3\vec{s} |\psi_e(\vec{r})|^2 \frac{-e^2}{\epsilon|\vec{r} - \vec{s}|} |\psi_h(\vec{2})|^2 \tag{2.6}$$

2.2.1 Exchange Splitting

An exchange splitting can arise between the energy levels of the excitonic state due to the antisymmetrization requirement for fermionic particles. This exchange splitting arises from the exchange part of the Coulomb interaction. Consider the case of an electron and hole with wavefunctions given by $\psi_e(x)$ and $\psi_h(x)$. The exchange portion of the interaction is given by

$$H^{ex} = \int d^3\vec{r} \int d^3\vec{s} \psi_e^*(\vec{r}) \psi_h(\vec{r}) \frac{e^2}{\epsilon|\vec{r} - \vec{s}|} |\psi_e(\vec{r}) \psi_h^*(\vec{r}) \tag{2.7}$$

2.3 Charge States

Thus far we have only considered a trapped exciton in the dot. In principle we could have multiple particles present including excess charge states (so-called trion states), and multi-exciton complexes such as bi-exciton states. This includes quantum dots which can absorb include an excess electron (X_-) and those that include an excess hole X_+. The neutral dot is denoted X_0 and the bi-exciton is labeled XX. There can also exist The negative trion state X_- is of great interest since they are candidates for quantum information devices [46, 47]. The schematic shown in Fig. 8.25 shows the possible charge states that can be present in quantum dot systems.

To add a charge to the neutral dot we can estimate the extra "charging energy" from first order perturbation theory. The electrostatic repulsion leads to about 10-20 meV per charge.

Using a Schottky diode it is possible to introduce a definite charge state into the dot and the effect of the charge state on the electronic and nuclear spin polarizations has been observed [48] and it has been reported that the charge state for GaAs quantum dots is separated by about 4-6 meV. Santori has provided evidence for these

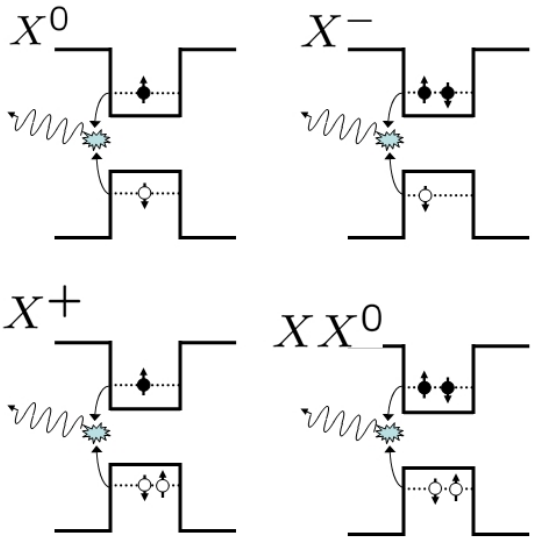

Figure 2.2: This diagram shows the different particle-complexes that can exist in the quantum dot. Included are the single exciton, X^0 which traps a single electron and hole. The X^- and the X^+ correspond to single charge states which include an excess electron and hole respectively. In addition, the neutral biexciton state, XX^0 can occur under large pump powers.

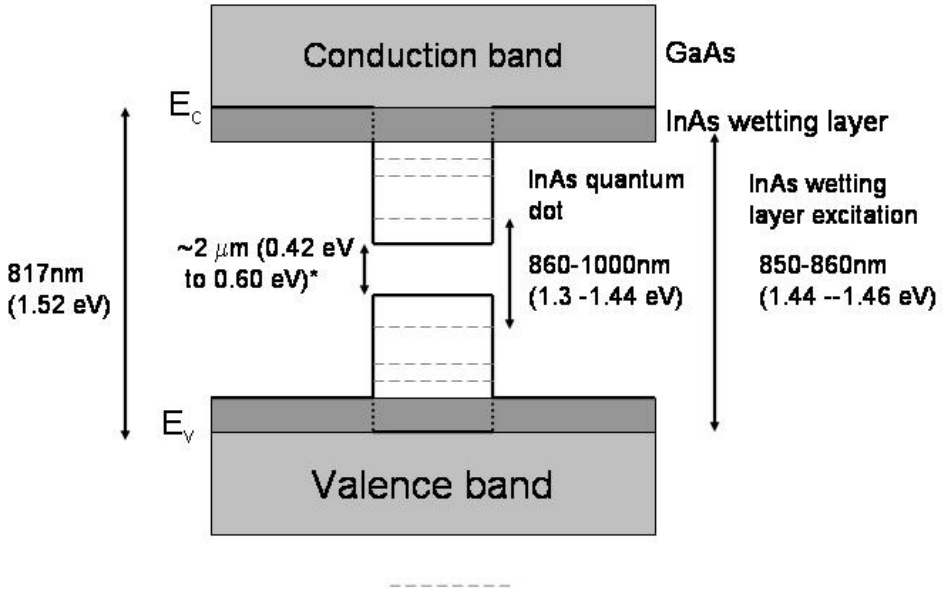

Figure 2.3: This schematic shows the band structure of the quantum dot, wetting layer and the surrounding GaAs semiconductor and pure InAs [1]. The energies shown are the numbers associated with low temperature operation near 4 K. Typically, the emitted light from radiative exciton recombination correspons to between 1.3 and 1.44 eV.

charge states simultaneously existing in nominally un-doped semiconductor without at external electric field present by doing correlation measurement studies with a Streak camera [3].

2.4 Zeeman Hamiltonian

When a magnetic moment is placed in an external magnetic field B_0 the magnetic moment of the spin can interact with magnetic field via the Zeeman hamiltonian $H = -\vec{\mu} \cdot \vec{B}$. In the case of excitons in a quantum both the electron and hole

can interact with the external magnetic field. For the case of a free electron the hamiltonian is given by $H = -g_0\mu_B\hat{S}\cdot\vec{B}$, where $g_0 = -2$ is the free electron g-factor.[1] For the remainder of this thesis we will follow the convention of Bayer *et al* **??** where the free electron g-factor is taken to be positive. Or alternatively, the Hamiltonian is defined as $H = +\vec{\mu}\cdot\vec{B}$. Fig. 2.4 graphically depicts the convention we use for defining the g-factor.

The g-factor depends on the band structure of the semiconductor and and for the hole is related to the Luttinger-Kohn parameters κ and q. The Zeeman Hamiltonian is given as follows:

$$H_{Zeeman}(\vec{B}) = -\mu_B \sum_i \left(g_{e,i}\hat{S}_{e,i} - 2\kappa_i \hat{J}_{h,i} - 2q_i \hat{J}^3_{h,i} \right) B_i \tag{2.8}$$

where $\hat{S}_e$ is the spin operator and $\hat{J}$ is the hole spin operator. The following table defines the exciton states that will be used throughout this thesis:

Exciton State	Electron spin $\otimes$ Hole spin
$\lvert+1\rangle$	$\lvert-\frac{1}{2}\rangle_e \otimes \lvert+\frac{3}{2}\rangle_h$
$\lvert-1\rangle$	$\lvert+\frac{1}{2}\rangle_e \otimes \lvert-\frac{3}{2}\rangle_h$
$\lvert+2\rangle$	$\lvert+\frac{1}{2}\rangle_e \otimes \lvert+\frac{3}{2}\rangle_h$
$\lvert-2\rangle$	$\lvert-\frac{1}{2}\rangle_e \otimes \lvert-\frac{3}{2}\rangle_h$

2.4.1 Faraday Geometry

In the case of the Faraday geometry we assume that $B_x = B_y = 0$ and that $B_z \neq 0$. Since $J^2_{h,z} = \frac{9}{4}$, we can simplify the Hamiltonian in the z-direction as:

$$H^{Faraday}_{Zeeman}(B_z) = -\mu_B \left(g_{e,z}S_{e,z} - (2\kappa_z + \frac{9}{2}q_z)J_{h,z} \right) B_z \tag{2.9}$$

$$= -\mu_B \left(g_{e,z}S_{e,z} - \frac{g_{h,z}}{3}J_{h,z} \right) B_z \tag{2.10}$$

[1] This is excluding quantum electrodynamic corrections.

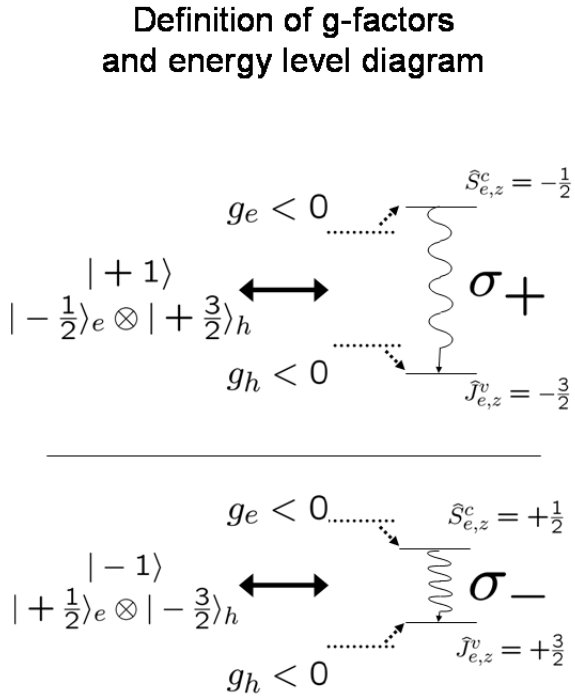

Figure 2.4: This diagram depicts the convention for the g-factor and shows which direction the energy levels shift for $g_e < 0$ and $g_h < 0$. Also, here the exciton states $|+1\rangle$ and $|-1\rangle$ are shown. For example, the state $|+1\rangle$ corresponds to a transition between a conduction state with angular momentum (all from spins) of $-1/2$ and a valence state with total angular of $-3/2$. In order to conserve angular momentum a photon (σ_+) with angular momentum of $+1$ is emitted. The exciton state can also be described by the state of the electron and the hole, where the hole has opposite the angular momentum to what the electron has when it relaxes to the valence band.

where $g_{h,z} = 6\kappa_z + \frac{27}{2}q_z$. We can write the Hamiltonian in matrix form where the rows correspond to $\{|+1\rangle, |-1\rangle, |+2\rangle, |-2\rangle\}$. We arrive at:

$$H_{\text{Zeeman}} = \frac{\mu_B B_z}{2} \begin{pmatrix} +(g_{e,z} + g_{h,z}) & 0 & 0 & 0 \\ 0 & -(g_{e,z} + g_{h,z}) & 0 & 0 \\ 0 & 0 & -(g_{e,z} - g_{h,z}) & 0 \\ 0 & 0 & 0 & +(g_{e,z} - g_{h,z}) \end{pmatrix} \tag{2.11}$$

This diagonal matrix immediately gives us the associated eigenenergies. Typically, the g-factor is negative in this convention, so the $|-1\rangle$ is the lowest energy bright state. The eigenvectors and associated energies are listed below:

Eigenenergy	Eigenstate
$\frac{1}{2}\delta_0 + \frac{1}{2}\sqrt{\delta_1^2 + \beta_1^2}$	$N_1\big[\,\lvert+1\rangle + \big(\frac{\beta_1}{\delta_1} + \sqrt{1 + \frac{\beta_1^2}{\delta_1^2}}\big)\,\lvert-1\rangle\,\big]$
$\frac{1}{2}\delta_0 - \frac{1}{2}\sqrt{\delta_1^2 + \beta_1^2}$	$N_2\big[\,\lvert+1\rangle + \big(\frac{\beta_1}{\delta_1} + \sqrt{1 + \frac{\beta_1^2}{\delta_1^2}}\big)\,\lvert-1\rangle\,\big]$
$-\frac{1}{2}\delta_0 + \frac{1}{2}\sqrt{\delta_1^2 + \beta_2^2}$	$N_3\big[\,\lvert+2\rangle + \big(\frac{\beta_1}{\delta_1} + \sqrt{1 + \frac{\beta_2^2}{\delta_1^2}}\big)\,\lvert-2\rangle\,\big]$
$-\frac{1}{2}\delta_0 - \frac{1}{2}\sqrt{\delta_1^2 + \beta_2^2}$	$N_4\big[\,\lvert+2\rangle + \big(\frac{\beta_1}{\delta_1} + \sqrt{1 + \frac{\beta_2^2}{\delta_1^2}}\big)\,\lvert-2\rangle\,\big]$

where $\beta_1 = \mu_B(g_{e,z} + g_{h,z})B_z$ and $-\beta_2 = \mu_B(g_{e,z} - g_{h,z})B_z$

2.4.2 Voigt Geometry

In the case of the Voigt geometry we have a $B_z = 0$ and $B_x \neq 0$ and/or $B_y \neq 0$. Furthermore, if we assume that $\kappa_x >> q_x$ then we can simplify as follows (assume $B_y = 0$):

$$\begin{aligned} H_{Zeeman}^{Faraday}(B_x) &= -\mu_B \left(g_{e,x} S_{e,x} - 2\kappa_x J_{h,x}\right) B_x & (2.12) \\ &= -\mu_B \left(g_{e,x} \frac{S_{e,x+} + S_{e,x-}}{2} - 2\kappa_{h,x} \frac{J_{h,x+} + J_{h,x-}}{2}\right) B_x & (2.13) \end{aligned}$$

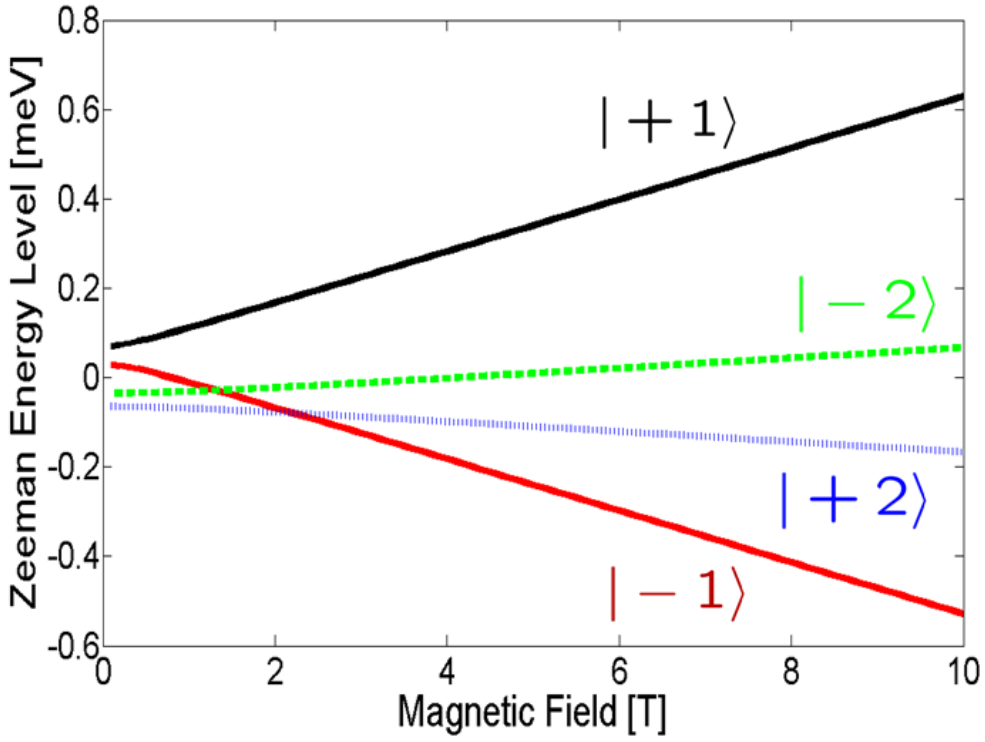

Figure 2.5: This plot shows the Zeeman levels in the Faraday configuration, including the bright and dark states for $g_{e,z} = -1.5$ and $g_{h,z} = -0.5$.

The Hamiltonian has off-diagonal terms which lead to mixing of the bright and dark states.

$$H_{\text{Zeeman}} = \frac{\mu_B B_z}{2} \begin{pmatrix} 0 & 0 & g_{e,x} & g_{h,x} \\ 0 & 0 & g_{h,x} & g_{e,x} \\ g_{e,x} & g_{h,x} & 0 & 0 \\ g_{h,x} & g_{e,x} & 0 & 0 \end{pmatrix} \tag{2.14}$$

Eigenenergy	Eigenstate
$\frac{1}{4}\left[+(\delta_1+\delta_2)+\sqrt{(2\delta_0+\delta_1-\delta_2)^2+4(g_{e,x}-g_{h,x})^2\mu_B^2B_x^2}\right]$	$N_1\big[\,(\lvert+1\rangle-\lvert-1\rangle)+\alpha_1\,(\lvert+2\rangle-\lvert-2\rangle)$
$\frac{1}{4}\left[-(\delta_1+\delta_2)+\sqrt{(2\delta_0-\delta_1+\delta_2)^2+4(g_{e,x}+g_{h,x})^2\mu_B^2B_x^2}\right]$	$N_2\big[\,(\lvert+1\rangle+\lvert-1\rangle)+\alpha_2\,(\lvert+2\rangle+\lvert-2\rangle)$
$-\frac{1}{4}\left[-(\delta_1+\delta_2)+\sqrt{(2\delta_0+\delta_1-\delta_2)^2+4(g_{e,x}-g_{h,x})^2\mu_B^2B_x^2}\right]$	$N_3\big[\,(\lvert+2\rangle-\lvert-2\rangle)+\alpha_3\,(\lvert+1\rangle-\lvert-1\rangle)$
$-\frac{1}{4}\left[+(\delta_1+\delta_2)+\sqrt{(2\delta_0-\delta_1+\delta_2)^2+4(g_{e,x}+g_{h,x})^2\mu_B^2B_x^2}\right]$	$N_4\big[\,(\lvert+2\rangle+\lvert-2\rangle)+\alpha_4\,(\lvert+1\rangle+\lvert-1\rangle)$

where $\beta_1 = \mu_B(g_{e,z}+g_{h,z})B_z$ and $-\beta_2 = \mu_B(g_{e,z}-g_{h,z})B_z$

2.5 Hyperfine Structure

2.5.1 Diamagnetic Shift

The average position of the Zeeman-split peak pair varies quadratically with increasing external magnetic field. In addition, it tends to shorter wavelength or higher energy and this effect can be explained by the quantum theory of diagmagnetism. As will be shown in Sec. 7.3 we have observed this quadratic dependence. For now, I would like to present the theory so that later when this phenomenon is presented the reader is familiar with the concept. In the results section, I will discuss our results, the diamagnetic coefficient and the interpretation of this result. In general when a magnetic field is present it is not the magnetic field which enters into the Hamiltonian but the vector potential. The general Hamiltonian is given by:

$$H' = \frac{ie\hbar}{2mc}(\vec{\nabla}\cdot\vec{A}+\vec{A}\cdot\vec{\nabla})+\frac{e^2}{2mc^2}A^2$$

With $\vec{B} = B\hat{z}$ the vector potential can be written as

$$\vec{A} = -\frac{1}{2}yB\hat{x} + \frac{1}{2}xB\hat{y} + 0\hat{z}$$

This leads to the following Hamiltonian:

$$H' = \frac{ie\hbar B}{2mc}(x\frac{\partial}{\partial y} - y\frac{\partial}{\partial x}) + \frac{e^2B^2}{8mc^2}(x^2 + y^2)$$

The associated energy is given by:

$$E' = \frac{e^2B^2}{12mc^2}\langle r^2\rangle$$

This is equivalent to writing the magnetic moment as

$$\mu = -\frac{\partial E'}{\partial B} = -\frac{e^2\langle r^2\rangle}{6mc^2}B$$

2.5.2 Bloch Wavefunction

As the reader may recall from section 2.1 the solution to the energy eigenstates is composed of both an envelope wavefunction and a periodic Bloch wavefunction. In addition, the electron and hole have different Bloch wavefunctions since the electrons are considered 's-like' while the holes are considered 'p-like.' Essentially, this means that the electrons have a finite probability of being at the site of the nucleus while the holes have exactly no probability of being at the nucleus. The relative probability to find an electron at a particular nuclear site depends on the overall envelope wavefunction as well what species of nuclear spins it is. This is because the ionicity affects the Bloch wavefunction. This quantity can be estimated and is done so in Section 2.5.4.

2.5.3 Overhauser Effect

The interaction of the nuclei located inside a quantum dot with a trapped exciton arises from the Fermi contact hyperfine interaction between the nuclear spins and the

trapped electron spin. The coupling between the nuclei and the hole is negligible since the holes are p-like states and the wavefunction overlap between the holes and the nuclei is 0. There are a number references which discuss the Overhauser effect and there is no consistent language so here I chose to follow the conventions in References [49, 50].

The Fermi contact Hamiltonian is given by

$$\hat{V}_{HF} = \frac{8\pi}{3}\frac{\mu_0}{4\pi} g_0 \mu_B \gamma_n \hbar \hat{I} \cdot \hat{S}\delta(\vec{r}) \tag{2.15}$$

where γ_n is the gyromagnetic ration and g_0 is the free-electron g-factor. (Comment on why it is the free electron g-factor)

If we used this Hamiltonian and tried to calculate the effect of the nuclear spins on the energy of an electron we would do so by first calculating the spatial component $\langle\psi(\vec{r})|\,\hat{V}_{HF}\,|\psi(\vec{r})\rangle$. Note that $\int_{R^3}\delta(\vec{r}) = 1$ since $\delta(r,\theta,\phi) = \frac{\delta(r)}{4\pi r^2}$ and in spherical coordinates $\int_{R^3} = \int_{-\pi}^{\pi}\int_0^{2\pi}\int_{-\infty}^{\infty} r^2\sin(\phi)d\theta d\phi dr$. This yields the following hyperfine interaction which depends only the spin interaction between the electron ($\hat{S}$) and nucleus ($\hat{I}$):

$$\hat{V}'_{HF} = \frac{2}{3}\mu_0 g_0 \mu_B \gamma_n \hbar \hat{I} \cdot \hat{S}|\psi(0)|^2 \tag{2.16}$$

The total electron wavefunction is given by the product of an envelope wavefunction and a periodic Bloch wavefunction so that $\psi(\vec{r}) = \Psi(\vec{r})u'(\vec{r})$ and for the wavefunction to be normalized we have $\int_{\text{QDOT}}|\psi(\vec{r})|^2 = 1$. As in *Paget*, we have use this renormalized wavefunction $u'(\vec{r})$. The normalization condition is $\int_{\text{QDOT}}|\Psi(\vec{r})|^2 d^3\vec{r} = \Omega$, where Ω is the volume of the unit cell. Also, $\int_{\text{QDOT}}|u'(\vec{r})|^2 d^3\vec{r} = 1/\Omega$. Thus, the relationship between the standard Bloch wavefunction, $\mu_0(\vec{r})$ and $\mu'(\vec{r})$ is given as follows:

$$\mu'(\vec{r}) = \mu_0(\vec{r})\sqrt{\frac{V}{\Omega}}$$

The standard Bloch wavefunction, $\mu_0(\vec{r})$, is normalized such that $\int_{\text{QDOT}}|\mu_0(\vec{r})|^2 d^3\vec{r} = 1/V$.

If we want to calculate what is the effect of all the nuclear spins on the electron we have to sum the single nucleus-electron hyperfine interaction, $\hat{V}'_{\text{HF}}$, over all the

nuclei within the dot.

$$\hat{H}_{\rm HF} = \sum_i \hat{V}'_{\rm HF} \tag{2.17}$$

$$= \sum_i \frac{2}{3}\mu_0 g_0 \mu_B \gamma_n^i \hbar |\Psi(\vec{r_i})|^2 |u'(\vec{r_i})|^2 \hat{I}_i \cdot \hat{S} \tag{2.18}$$

All of the re-normalized Bloch wavefunction evaluations at $\vec{r_i}$ are identical for similar nuclei. We can define $d_j = |u'(\vec{r_j})|^2$ and introduce a_i to be

$$a_i = \frac{2}{3}\mu_0 g_0 \mu_B \gamma_n^i \hbar d_i \tag{2.19}$$

If we introduce in Eq. 2.17 a sum over all different nuclear species (including isotopes) α, and sum over all nuclei of that species we can write:

$$\hat{H}_{\rm HF} = \sum_i a_i |\Psi(\vec{r_i})|^2 \hat{I}_i \cdot \hat{S} \tag{2.20}$$

$$= \sum_i c_i \hat{I}_i \cdot \hat{S} \tag{2.21}$$

$$= \sum_\alpha \sum_{j=1}^{n_\alpha} a_j \hat{I}_j \cdot \hat{S} |\Psi(\vec{r_j})|^2 \tag{2.22}$$

$$\tag{2.23}$$

To proceed we note that the envelope wavefunction, $\Psi(\vec{r})$, does not vary much over any single unit cell, Ω. We can write [2],

$$\int_{\Omega_j} |\Psi(\hat{r})|^2 d^3\vec{r} \approx |\Psi(\vec{r_j})|^2 \Omega \tag{2.24}$$

[2] A more rigorous argument can be made using a Fourier transform of delta functions

If we sum both sides over all nuclei i we arrive at

$$\underbrace{\sum_i \int_{\Omega_i} |\Psi(\vec{r})|^2 d^3\vec{r}}_{\int_{QDOT} |\Psi(\vec{r})|^2 d^3\vec{r}} \approx \sum_i |\Psi(\vec{r}_i)|^2 \Omega \tag{2.25}$$

$$\int_{QDOT} |\Psi(\vec{r})|^2 d^3\vec{r} \tag{2.26}$$

This last step is simply that we sum up integrals over each unit cell which is equivalent to integrating over the entire quantum dot. So we finally arrive at

$$\sum_i |\Psi(\vec{r}_i)|^2 = \frac{1}{\Omega} \int_{QDOT} |\Psi(\vec{r})|^2 d^3\vec{r} \tag{2.27}$$

$$= 1 \tag{2.28}$$

The next step we is to use the mean-field approximation where we sum over all the nuclei and insert Eqn. [**?**]. This yields an operator which only acts on the electron spin in the dot.

$$\langle \hat{H}_{\mathrm{HF}} \rangle = \sum_\alpha A_\alpha \langle I_{z,\alpha} \rangle \hat{S}_z \tag{2.29}$$

$$= \left[(A_{^{113}In} \xi_{^{113}In} + A_{^{115}In} \xi_{^{115}In}) \langle I_{z,\mathrm{In}} \rangle + A_{^{75}As} \langle I_{z,\mathrm{As}} \rangle \right] \hat{S} \tag{2.30}$$

Here we have made the substitution

$$A_\alpha = \sum_{j=1}^{n_\alpha} a_j |\Psi(\vec{r})_i|^2$$

$$= \sum_{j=1}^{n_\alpha} a_j c_i$$

Also, ξ is the relative abundance of a particular isotope. The actual values are shown in Table 2.1. Instead of writing the Hamiltonian of the system we can also describe the interaction between the nuclei and the electron spin as an external magnetic field

Table 2.1: Values for gyromagnetic ratio and isotope abundance

Element	**Isotope**	**Spin**	**Natural Abundance [%]**	**Gyromagnetic Ratio (γ_n) [$\frac{10^7 \mathbf{rad}}{\mathbf{T\ s}}$]**	Quadrupole moment (Q) [mBarn]
Gallium	^{69}Ga	3/2	60.108	6.4389	171
	^{71}Ga	3/2	39.892	8.1812	107
Arsenic	^{75}As	3/2	100	4.5961	314
Indium	^{113}In	9/2	4.3	5.8845	799
	^{115}In	9/2	95.7	5.8971	810

given by

$$\vec{B}_N = \frac{2\mu_0}{3}\frac{g_0}{g_e}\hbar\sum_i \gamma_i I_i |\psi(r_i)|^2 \tag{2.31}$$

where the sum over i goes over all the nuclei in the dot and the g-factor g_e is the effective g-factor of the electron in the dot (typically ≈ -2). We can relate our expression in Eq. 2.29 for the Hamiltonian as:

$$\langle \hat{H}_{\mathrm{HF}} \rangle = \sum_\alpha A_\alpha \langle I_{z,\alpha} \rangle \hat{S} \tag{2.32}$$

$$= \mu_B g_{e,z} \hat{S}_z B_{N,z} \tag{2.33}$$

To simplify, suppose we write $\langle \hat{H}_{HF} \rangle = \beta \hat{S}_z$. In addition to the external magnetic field the exciton (and specifically the electron) see an internal magnetic field created by the nuclei. The nuclei will become aligned or anti-aligned with the external magnetic field depending on the direction of the electron spin introduced which is controlled by the laser pump polarization (see Section 5.4.5). Suppose the observed Zeeman energy splitting under σ_+illumination is give by Δ_{σ_+} and under σ_-pump polarization the energy splitting is given by Δ_{σ_-}, then we can write

$$\Delta = |\Delta_{\sigma_+} - \Delta_{\sigma_-}| \tag{2.34}$$

With perfect polarization the observed value for Δ would be $2\beta^*$, where $\beta^* =$

$A_{\mathrm{In}}9/2 + A_{\mathrm{As}}3/2$ but in the regime far from perfect polarization more care must be taken to determine the polarization. We can think of the nuclear polarization process as one where nuclei are polarized at some rate while depolarized (either through relaxation or diffusion) at another rate. These two competing processes lead to a steady-state equilibrium. The arsenic nuclei can only undergo at most 3 flips towards a polarized state since they have spin 3/2 while the indium nuclei can flip as many as 9 times since they are spin 9/2. This assumes we start from the anti-aligned state and move towards the aligned state.

In this sense the polarization rate is reduced as the arsenic nuclei become more polarized because the electron wavefunction still is distributed among the arsenic and indium nuclei. Once the arsenic nuclei have reached 100% polarization we have to wait longer for nuclear spin flips to occur as there is a reduced probability of a nuclear spin flip per unit time since only the indium will contribute to the polarization increase, and the electron wavefunction still is spread over all the nuclei.

If we are indeed in a regime where the nuclear polarization is far from saturating the arsenic polarization we can assume that the average spin of the nuclei is the same for both indium and arsenic. Then we have $A_{\mathrm{eff}} = A_{\mathrm{In}} + A_{\mathrm{As}}$ which is 102μeV. The average nuclear spin is given by $\langle I \rangle = \Delta/2\beta$. Thus, the polarizations for the different nuclear species will be different. The polarization can be calculated as

$$P = \frac{\Delta}{2IA_{\mathrm{eff}}} \tag{2.35}$$

where $I = 9/2$ for Indium or $I = 3/2$ for arsenic. A summary of the various energies, equivalent magnetic fields for GaAs and and InAs is shown in Table 2.2. The measured polarization values will be reported in Section 8.1.3.

Another important point is that the non-equilibrium nuclear polarization induced by optical pumping (see Chapter 3) should be compared to the thermal polarization

and statistical polarization. For a system of spin 1/2-particles the thermal polarization at a temperature T and magnetic field B is given by

$$P_{th} = \frac{N_\uparrow - N_\downarrow}{N_\uparrow + N_\downarrow} \tag{2.36}$$

$$= \tanh \frac{\hbar \gamma_N}{B} k_B T) \tag{2.37}$$

For typical nuclei with γ_B 5×10^7 radT s, the thermal polarization at 2 K and 1 T is $\sim 10^{-4}$. This estimate allows us to conclude that the thermal polarization can be neglected for the temperatures and magnetic fields we operate at. One point is that both arsenic and indium are not spin 1/2 nuclei so the calculation is more complicated but for the purposes of this estimation the result we have is sufficient. If the field is raised up to 10 T and we used a dilution fridge system then this effect cannot be entirely neglected.

The statistical polarization corresponds to fact that we have a small number of nuclear spins present and a subset of them may randomly point in one direction which could give rise to a measurable Overhauser effect. The quantum dot contains between 10^4 and 10^5 nuclei and statistically $\sim \sqrt{N}$ of the nuclei can point in one direction. Suppose there are 4×10^4 nuclei, then 2×10^2 would correspond to the number of nuclei that may be statistically polarized. That is 200 more nuclei may randomly point up than down or vice-versa. This difference leads to a polarization given by

$$P_{st} = \frac{N_\uparrow - N_\downarrow}{N_\uparrow + N_\downarrow} \tag{2.38}$$

$$= \frac{2 \times 10^2}{4 \times 10^2} = 5 \times 10^{-3} \tag{2.39}$$

It is interesting to note that the statistical polarization and the thermal polarization we might expect are comparable and in fact the statistical polarization appears slightly larger. It turns out that we have observed nuclear polarizations that are between 2 to 3 order of magnitude larger than these values. However, future research could include studies of these effects.

Table 2.2: Values for A, A_{eff} and β^* and the equivalent magnetic fields

Semiconductor	**Hyperfine constant**	**Value [μeV]**	$\mathbf{g}_{e,z}\mathbf{B}_{N,z}$ **[T]**
GaAs	A_{Ga}	42	0.73
	A_{As}	46	0.80
	$A_{\text{eff}} = (A_{\text{Ga}} + A_{\text{As}})$	88	1.53
	$B^* = \frac{3}{2}(A_{\text{Ga}} + A_{\text{As}})$	132	2.29
InAs	A_{In}	56	0.97
	A_{As}	46	0.80
	$A_{\text{eff}} = A_{\text{In}} + A_{\text{As}}$	102	1.77
	$B^* = \frac{9}{2}A_{\text{In}} + \frac{3}{2}A_{\text{As}}$	323	5.58

.

Table 2.3: Ionicities for III-V semiconductors

GaAs	0.31
InAs	0.357
InSb	0.321

2.5.4 Ionicity and Nuclei-Electron Wavefunction Overlap

If we assume that the sharing of electrons in GaAs is the same for InAs given their similar ionicities then we can estimate the values for η_{In} and η_{As}. See Ref. [51] for calculation of the ionicity. In Paget *et al* [52] a similar argument is made to compare GaAs to InSb in which an actual measurement has been made for the hyperfine interaction. The atomic hyperfine interactions are known for In, As, and Ga [53]. Paget *et al* use a dimension d to describe the hyperfine interaction in a crystal and it can be related to η_α by:

$$\eta_\alpha = \frac{da^3}{n_\alpha}$$

where a is the lattice constant (see Table 2.4 and n_α is the number of nuclei of that type α within the unit cell, Ω.

Table 2.4: Lattice constants for GaAs and InAs.

GaAs	5.65325 Å
InAs	6.0583 Å
InSb	6.4279 Å

Table 2.5: Wavefunction overlap for various III-V semiconductors

Semiconductor	**Element**	η	d [cm^{-3}]
GaAs	Ga	2.7×10^3	5.8×10^{25}
	As	4.5×10^3	9.8×10^{25}
InSb	In	6.3×10^3	9.5×10^{25}
	Sb	10.9×10^3	16.4×10^{25}
InAs	In	5.2×10^3	9.35×10^{25}
	As	5.4×10^3	9.8×10^{25}

Using the ratio formula we can write:

$$\begin{aligned} \frac{d_{\text{In in InAs}}}{d_{\text{Ga in GaAs}}} &= \frac{|\psi(0)|^2_{\text{In atom}}}{|\psi(0)|^2_{\text{Ga atom}}} \\ \frac{d_{\text{As in InAs}}}{d_{\text{As in GaAs}}} &= \frac{|\psi(0)|^2_{\text{As atom}}}{|\psi(0)|^2_{\text{As atom}}} \end{aligned}$$

So this gives us $d_{\text{As in InAs}} = d_{\text{As in GaAs}} = 9.8 \times 10^{25} cm^{-3}$ and $d_{\text{In in InAs}} = \frac{10}{6.2} 5.8 \times 10^{25} cm^{-3}$.

2.5.5 *g*-factor

The g-factor plays an important role in both how the emission peaks shift due to the Overhauser effect and also in regard to the use of quantum dots as magnetic field sensors. First, I want to clarify the sign convention that I use for the g-factor and introduce to the reader why there exists different sign conventions. Secondly, I want to mention the expected value for the g-factor and the mechanisms that effect its magnitude. This is of particular importance for understanding the spectra and the expected Overhauser shifts as well as the use of quantum dots as magnetic field

sensors.

References [54] and [45] present how the bandgap for $In_{1-x}Ga_xAs$ depends on the stochiometry. Namely for a given value of x the bandgap energy is given by as follows

$$E_g(\Gamma) = 0.422 + 0.7x + 0.4x^2 \text{ eV} \tag{2.40}$$

It is also worth noting the effective mass depends on the stoichiometry in the following way:

$$\frac{1}{m_e^*(x)} = \frac{x}{m_{e,\text{GaAs}}^*} + \frac{1-x}{m_{e,\text{InAs}}^*} \tag{2.41}$$

For a quantum dot the electron and hole wavefunction depends on the size of the dot and the stoichiometry of the material. The dot growth (discussed in 6.1.1) occurs at 600 ^{o}C which can lead to annealing and a mixing of the In and Ga atoms. In addition for one study [55] on $In_{0.10}Ga_{0.90}As$, very large dots had g-factors that tended toward the bulk GaAs value of -0.4 while the smaller dots had larger negative g-factors (-4 to -12) which are more like pure InAs. For an infinite square well the energy of the states is proportional to $\frac{1}{m^*a^2}$ where a is the size of the well and m^* is the effective mass. Thus, with tighter confinement or smaller a the energy is further increased but also the electron and hole wavefunctions are more tightly bound within the InAs. It may also be that the smaller dots had a higher indium concentration and the stoichiometry only reports the MBE growth conditions and not the actual stoichiometry of any particular quantum dot.

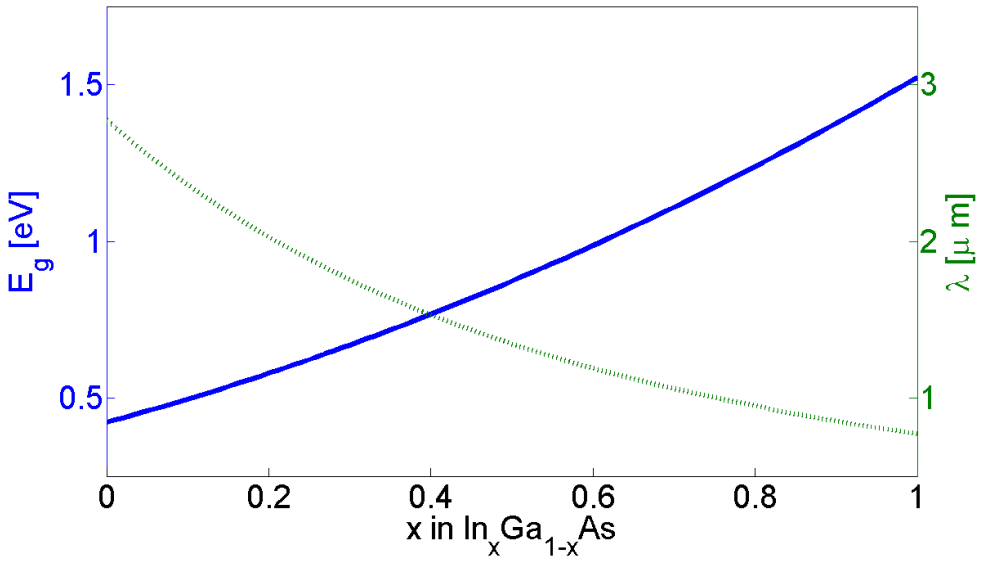

Figure 2.6: This figure shows the bandgap for $In_{1-x}Ga_xAs$ and the corresponding wavelength.

Chapter 3

Nuclear Spin Dynamics

In this chapter we will derive the nuclear polarization timescale and present a model that explains how the nuclei within InAs quantum dots become polarized. Returning to Sec. 2.5.3 and rewriting Eq. 2.21 to introduce flip-flop terms we can write:

$$\hat{H}_{\mathrm{HF}} = \sum_i c_i \hat{I}_i \cdot \hat{S} \tag{3.1}$$

$$= \sum_i c_i \left[\hat{I}_{i,z}\hat{S}_z + \frac{\hat{I}_{i,+}\hat{S}_- + I_{i,-}\hat{S}_+}{2} \right] \tag{3.2}$$

The last two terms corresponds to terms of the Hamiltonian where the electron spin and a single nuclear spin simultaneously flip their spin directions. This process conserves angular momentum but does not conserve energy and therefore requires some assisting process in order to occur.

The basic model for nuclear polarization is based on a fast hole-relaxation time after which the exciton is trapped in a dark exciton state. Hole-relaxation within dots has been found in GaAs to be faster than 5ps [56, 57]. Holes have $l = 1$ angular momentum and therefore couple well to phonons which at 1.5K are abundant. If the exciton is pumped into a bright state (i.e. $|+1\rangle$ or $|-1\rangle$), it quickly relaxes to a dark state (i.e. $|-2\rangle$ or $|+2\rangle$) as shown in Figure 8.4. Once in the dark state the exciton will either return to the bright state from which it came via phonon coupling with the hole, or it will undergo a spin-flip assisted radiative process whereby a nuclear

spin and electron simultaneously flip and thereby causing the exciton to go into a new bright state. This process is a second order process and requires a hyperfine interaction between the electron and a nucleus in the dot.

3.1 Fermi's Golden Rule

Fermi's golden rule is an important result from Time-Dependent Perturbation Theory which provides a means of calculating a transition rate between two states. The transition rate is a transition probability per unit time and when taken to 2nd order is [58]:

$$w_{i\to[f]} = \frac{2\pi}{\hbar}\overline{|V_{fi} + \sum_p \frac{V_{fp}V_{pi}}{E_i - Ep}|^2}\rho(E_f)|_{E_f\simeq E_i}$$

To summarize we assume that we start in some initial state $|i\rangle$ and transition into one of many possible states $|f\rangle$, which we denote by $[f]$ where $E_i \simeq E_f$. Note that a direct transition between $|i\rangle$ and $|f\rangle$ may be 0 in which case only the 2nd order terms are relevant [1]. In our case a virtual process is responsible for the nuclear polarization. The second term can be interpreted as one where the system makes a transition between the initial state and an intermediate state but not necessarily conserving energy. Then, the final state transfer occurs and in order to conserve energy the missing or excess energy is made up through some other means, such as a decrease or increase in the energy of the emitted photon. For the case of nuclear polarization we believe it is spin-flip assisted radiative recombination. The dark exciton is quickly populated and via hyperfine interaction the quantum dot emits a photon.

[1] In our case the direct process, V_{fi}, does not conserve energy and so is therefore 0.

3.2 Nuclear Polarization Rate

We begin by writing out Fermi's Golden Rule for our case:

$$\frac{1}{T_e} = \frac{2\pi}{\hbar} \sum_i P_i \sum_p \Big| \frac{\langle f| \hat{V}_{dip} |p\rangle \langle p| \hat{V}_{HF} |i\rangle}{E_i - Ep} \Big|^2 \rho(E_f)|_{E_f \simeq E_i} \tag{3.3}$$

Notice that here we rewrote the rate as $1/T_e$ and we inserted a sum $\sum_i$ over initial states weighted with probabilities P_i. The perturbations V_{fp} and V_{pi} are replaced with the relevant Hamiltonians; the first takes the state from one of the possible initial states $|i\rangle$ via a hyperfine interaction, $\hat{V}_{HF}$, to an intermediate where an electron spin in the exciton and a single nuclear spin flip within the dot; the second term is responsible for the radiative recombination of the bright exciton and is a electric dipole transition from a bright exciton to the empty dot state. The energy required for the hyperfine interaction is compensated for by a change in the emitted photon energy. The initial states are either

$$\begin{aligned} |i\rangle &= |+2\rangle \otimes |m_1, m_2, \ldots, m_p, \ldots, m_N\rangle \\ |i\rangle &= |-2\rangle \otimes |m_1, m_2, \ldots, m_p, \ldots, m_N\rangle \end{aligned}$$

depending on which type of the polarized light we shine on the quantum dots.

The only relevant intermediate states are those by which a hyperfine interaction gives a non-zero result:

$$\begin{aligned} \langle p| \hat{V}_{\mathrm{HF}} |i\rangle &= \langle +1| \otimes \langle m_1, m_2, \ldots, m_{p+1}, \ldots, m_N| \, cS^- I_p^+ \, |+2\rangle \otimes |m_1, m_2, \ldots, m_p, \ldots, m_N\rangle \\ \langle p| \hat{V}_{\mathrm{HF}} |i\rangle &= \langle -1| \otimes \langle m_1, m_2, \ldots, m_{p-1}, \ldots, m_N| \, cS^+ I_p^- \, |-2\rangle \otimes |m_1, m_2, \ldots, m_p, \ldots, m_N\rangle \end{aligned}$$

The transition that takes us from the intermediate state to the empty dot state of the quantum dot is a electric dipole transition and we can define M^+ and M^- as

$$\begin{aligned} M^{+} &= \langle f| \hat{V}_{\text{dip}} |p\rangle \\ &= \langle GS| \langle m_1, m_2, \ldots, m_{p+1}, \ldots, m_N| \hat{V}_{\text{dip}} |m_1, m_2, \ldots, m_{p+1}, \ldots, m_N\rangle |+1\rangle \end{aligned}$$

and

$$\begin{aligned} M^{-} &= \langle f| \hat{V}_{\text{dip}} |p\rangle \\ &= \langle GS| \langle m_1, m_2, \ldots, m_{p-1}, \ldots, m_N| \hat{V}_{\text{dip}} |m_1, m_2, \ldots, m_{p-1}, \ldots, m_N\rangle |-1\rangle \end{aligned}$$

An important result from basic quantum mechanics regarding angular momentum raising or lower operators [59]is

$$L^{\pm} |l, m\rangle = \hbar\sqrt{l(l+1) - m(m \pm 1)}\, |l, m \pm 1\rangle$$

Then we sum over all possible initial states including the different nuclear spin species and different possible nuclear spin states of all the nuclei in the dot. Suppose there are N_{In} Indium nuclei and N_{As} Arsenic nuclei and N_{Ga} Gallium nuclei.

An important substitution we can make in order to simplify the expression is to replace the component of the calculation which relates the density of photon states and the dipolar matrix element connecting one of the bright exciton states to the ground state. This is achieved by writing:

$$\begin{aligned} \frac{1}{\tau_b^{+}} &= \frac{2\pi}{\hbar} |M_{+}|^2 \rho(E_{abc}) \\ \frac{1}{\tau_b^{-}} &= \frac{2\pi}{\hbar} |M_{-}|^2 \rho(E_{abc}) \end{aligned}$$

The rate $1/\tau_b$ is the bright exciton lifetime which from the literature is known to be ~ 0.5s (see [3]) and $\tau_b^{+} = \tau_b^{-}$. Another important point is that the denominator in Eqn. 3.3 containing the difference in energies between the initial and intermediate

state, $E_i - E_p$, can be replaced by δ_0^- or δ_0^+.

Next we consider the interaction of the electron spin with In and As separately, and ascribe a different hyperfine constant A_p for each nuclei. Notice that this site dependent factor and includes the wavefuntion overlap with a particular nuclear site. To simplify we also calculate separately the transition rates for pumping into $|+1\rangle$ and $|-1\rangle$, and here we continue only with an analysis for σ_+pumping. $P(m_p)$ is the probability that the nuclei p is in a particular nuclear sublevel.

$$\begin{aligned}\frac{1}{T_e^+} &= \frac{1}{\tau_b^+ \delta_0^2} \sum_{p=1}^{N} P(p) \sum_{m_I=-I_1}^{I_1} P(m_1) \sum_{m_I=-I_2}^{I_2} P(m_2) \\ &\quad \ldots \sum_{m_I=-I_N}^{I_N} P(m_N) |a_p|^2 ||\Psi(\vec{r}_p)|^4 \big[I_p(I_p+1) - m_p(m_p+1) \big]\end{aligned}$$

Now we can rewrite our sum to include A_p^{In} and A_p^{As} and change the sums to only sum over the number of nuclei of each type. Also if we assume the infinite temperature limit then all nuclear sublevels are equally populated and we can replace $P(m_{In}) = 1/10$ and $P(m_{As}) = 1/4$ since Indium is a spin 9/2's and Arsenic is a spin 3/2.

$$\begin{aligned}\frac{1}{T_e^+} &= \frac{1}{\tau_b^+ \delta_0^2} \Big(\sum_{j=1}^{n_{\mathrm{In}}} |a_j^{\mathrm{In}}|^2 |\Psi(\vec{r}_j)|^4 \frac{35}{2} + \\ &\quad + \sum_{k=1}^{n_{\mathrm{As}}} |a_j^{\mathrm{As}}|^2 |\Psi(\vec{r}_j)|^4 \frac{5}{2} \Big)\end{aligned}$$

The next step in the process to get use a numerical result is to assume a particular envelope wavefunction for the exciton.

The envelope wavefunction, $\Psi(\vec{r})$ can be written as a Gaussian with width σ as

$$\Psi(r) = \sqrt{\Omega} \frac{1}{(\pi\sigma^2)^{3/4}} e^{-\frac{r^2}{2\sigma^2}} \tag{3.4}$$

In a similar manner to Section 2.5.3 we can assume that $\Psi(\vec{r}_i)$ is a smoothly

varying function and is constant over a single unit cell such that

$$\sum_i |\Psi(\vec{r}_i)|^4 = \frac{1}{\Omega}\int_{QDOT} |\Psi(\vec{r}_i)|^4 d^3\vec{r} \tag{3.5}$$

$$= \frac{\Omega^2}{\Omega}\frac{1}{(\pi\sigma^2)^3}(2\pi\sigma^2)^{3/2} \tag{3.6}$$

$$= \frac{\Omega}{\sigma^3}(\frac{2}{\pi})^{3/2} \tag{3.7}$$

Using this envelope wavefunction we arrive at an expression for the nuclear polarization timescale

$$\frac{1}{T_e^+} = \frac{1}{2}\frac{1}{\tau_b^+\delta_0^2}\frac{\Omega}{\sigma^3}(\frac{2}{\pi})^{3/2}\big(\frac{35}{2}|A_{\mathrm{In}}|^2 + \frac{5}{2}|A_{\mathrm{As}}|^2\big) \tag{3.8}$$

The factor of 1/2 comes from the fact that when we sum over all the nuclei in the dot we only sum over the Indium for the first term and for Arsenic for the second which contain exactly 1/2 the number of nuclei each.

Let us explore a different potential to calculate the envelope wavefunction of electron. Suppose instead we assume a particle in a box. Regardless of the numerical factors due to the envelope wavefunction we see a clear dependence on δ_0. We can in turn relate this to magnetic field.

3.3 Nuclear Depolarization

Nuclei in a solid-state crystal have long relaxation times at low temperature. However, in the presence of a laser field the nuclei within the dot see a fluctuating magnetic field due to the electron spin excited by the laser. The depolarization arises from a heating effect induced by temporal fluctuations of the hyperfine field of the optically excited electron. The formalism to calculate the relaxation time is derived in Ladd thesis.

3.4 Rate equations

A full analysis of the time evolution of the population of the various states requires the use of a rate equation model. This model assumes that the rate of change of the population of a given state is directly proportional to the population of states that couple to it including possibly itself. This is a linear model and serves as a reasonable first approximation. To simplify the model we also assume two extremes for the nuclear polarization; spin-up and spin-down. Thus, the model I used included

10 states:

label	state	description
n_1	$n_{GS,\downarrow}$	nuclear spin down, electron in ground state
n_2	$n_{GS,\uparrow}$	nuclear spin down, electron in ground state
n_3	$n_{\lvert+1\rangle,\downarrow}$	nuclear spin down, electron in $\lvert+1\rangle$
n_4	$n_{\lvert+1\rangle,\uparrow}$	nuclear spin down, electron in $\lvert+1\rangle$
n_5	$n_{\lvert-1\rangle,\downarrow}$	nuclear spin down, electron in $\lvert-1\rangle$
n_6	$n_{\lvert-1\rangle,\uparrow}$	nuclear spin down, electron in $\lvert-1\rangle$
n_7	$n_{\lvert+2\rangle,\downarrow}$	nuclear spin down, electron in $\lvert+2\rangle$
n_8	$n_{\lvert+2\rangle,\uparrow}$	nuclear spin down, electron in $\lvert+2\rangle$
n_9	$n_{\lvert-2\rangle,\downarrow}$	nuclear spin down, electron in $\lvert-2\rangle$
n_{10}	$n_{\lvert-2\rangle,\uparrow}$	nuclear spin down, electron in $\lvert-2\rangle$

These states evolve according to the matrix below. P_+ and P_- correspond to the laser pump rate from the ground state for the two different pump polarizations. w_r is the radiative recombination rate and w_{ph} corresponds to phonon interaction. Finally, w_+ and w_- are nuclear spin-flip radiative recombination rates for the different pathways as calculated previously in this chapter. The results shown in Chapter 7 for optical pumping timescales is derived from this theory and the code used to calculate these rates is shown in Appendix B

$$\dot{\vec{n}} = M\vec{n}$$

$$M = \begin{pmatrix}
-(P_+ + P_-) & 0 & w_r & 0 & w_r & 0 & 0 & 0 & 0 & w_- \\
0 & -(P_+ + P_-) & 0 & w_r & 0 & w_r & w_+ & 0 & 0 & 0 \\
P_+ & 0 & -w_r + w_1 & 0 & 0 & 0 & 0 & 0 & w_{ph1} & 0 \\
0 & P_+ & 0 & -w_r + w_1 & 0 & 0 & 0 & 0 & 0 & w_{ph1} \\
P_- & 0 & 0 & 0 & -w_r - w_1 & 0 & -w_{ph2} & 0 & 0 & 0 \\
0 & P_- & 0 & 0 & 0 & -w_r - w_1 & 0 & w_{ph2} & 0 & 0 \\
0 & 0 & 0 & 0 & w_{ph3} & 0 & w_2 - w_+ & 0 & 0 & 0 \\
0 & 0 & 0 & 0 & 0 & w_{ph3} & 0 & w_{ph2} & 0 & 0 \\
0 & 0 & w_{ph4} & 0 & 0 & 0 & 0 & 0 & w_{ph4} & 0 \\
0 & 0 & 0 & w_{ph4} & 0 & 0 & 0 & 0 & 0 & w_{ph4} - w_-
\end{pmatrix}$$

3.5 Charged States

Thus far the model developed explains nuclear polarization in a neutral dot and the expected spectra. Charged dots, as will be shown in Section 8.4, also exhibit evidence for Overhauser shifts and interesting spectral properties. It has been reported that the X^- trion state exhibits negative polarization behavior in the optical emission [48]. Additionally, previous work has observed negative polarization[2] in charged quantum dots [60].

3.6 Nuclear Magnetic Resonance

Coupling directly to nuclear spins with a magnetic moment can be achieved with radio frequency (rf) photons. The resonance condition for standard nuclear magnetic resonance is given by:

$$\omega_0 = \gamma_I B_0 \tag{3.9}$$

where γ_I is the gyromagnetic ratio of the nucleus and B_0 is the magnetic field experienced by the nuclear spin. Table 2.1 shows values for γ_I for the relevant nuclei in our system. Radio frequency photons can cause the nuclear spins to make transitions between different m_I levels.

It is possible to use a continuous wave (cw) or a pulse rf source to for transmitting rf. The main requirement is that the sample be near to the rf transmitter so that effective power of the rf is sufficient to drive enough nuclear spin transitions. This is achieved by designing a suitable coil and rf circuit (see Section 5.3.2). The details of NMR experiments are in and of themselves the content of many thesis (see [**?**]) so the main point to take away is through rf we can interact with nuclei and through the effect of the nuclear spin direction on emitted light from a quantum dot. If we can control the nuclear spins through other means this too would manifest itself in the emitted photon energy and indeed by adjusting the excitation laser polarization

[2]The spin memory is related to the polarization by the formula $P = \frac{I_{\sigma_+} - I_{\sigma_-}}{I_{\sigma_+} + I_{\sigma_-}}$ where I_{pol} is the intensity of the two Zeeman-split emission under a given polarization. Thus negative polarization implies that under σ_+pumping the emitted light is predominantly σ_-.

we control the nuclear polarization within the quantum dot.

3.6.1 Nano-NMR in quantum dots

Previous work [61] has demonstrated coupling between nuclei and the emission from single GaAs quantum dots by using continuous wave rf. This has been an active area of research for our group as well. However, we have not successfully demonstrated and our experimental techniques and results are discussed in Section 8.3. The principal reason is likely due to quadrupolar effects which is now explained.

3.6.2 Quadrupole Effects

For nuclei with spin $I > 1/2$ the positive electric charge these nuclei carry is not distributed with perfect spherical symmetry and thus gives rise to a quadrupolar moment. When placed in an electric field gradient (efg) the quadrupole moment interaction with the efg leads to a splitting in the energy levels of the different m_I-sublevels. Thus, one can perform nuclear quadrupole resonance (NQR) even in the absence of an external magnetic field provided the nuclei are in an environment in which they see an efg. In fact many nuclei within solids experience efg's and this is also the case with quantum dots.

3.6.3 Strain in Quantum Dots

Some materials naturally have large electric field gradients and so nuclear quadrupole splitting occurs (e.g. covalently bonded Cl_2 molecules). Self-assembled InAs quantum dots form in order to minimize the strain at the interface between the InAs layers and the GaAs. However, very large strains still exist in and around the dot [62]. The electric field gradient can be related to the strain in the system [63, 64]. Roughly the amount of quadropole splitting in MHz is found for GaAs to be 3 MHz/%strain. Thus, for strains of order 5% the quadrupole splitting can be as large as 15 MHz. In addition, according to Grundmann *et al* [62], the strain is not uniform and thus the broadening can be tens of MHz. Gammon *et al* report that the nuclear spin resonace

was not uniform and in fact some dots had linewidths of ∼200 kHz. Yet other dots did not exhibit any resonance suggesting that the strain in those dots was sufficiently large to create inhomogeneously broadened quadrupolar splittings.

Chapter 4

Magnetic Field Gradient Generation

4.1 Introduction

A quantum computer using nuclear spins in a crystal lattice requires a method for addressing individual quantum bits. This identification can be achieved with a spatially varying magnetic field. Spins at different lattice sites can have distinguishable Zeeman frequencies allowing initialization, logic operations, and measurements to be performed through radio frequency (rf) pulse techniques. In this Chapter we present magnet designs that have gradients between 1 and 20 T/μm, which are necessary to realize quantum computation with particular crystals. As a reminder, we desire to maximize η in Eq. 1.3, which translates into field gradients typically larger than 1 T/μm.

4.2 Design Considerations

Designs should be chosen so that the field gradient is sufficient and the fabrication is realistic. Here we consider the question of how to construct such field gradients within the crystal and what implications these designs have for quantum computation.

Field gradients can be in one, two, or three dimensions. A basic form of a one-dimensional quantum computer has a field gradient in one dimension with the orthogonal dimensions having minimal field variation. Maxwell's equations for a static system not enclosing any currents state that $\nabla \cdot \vec{B} = 0$ and $\nabla \times \vec{B} = 0$. Thus, a gradient or spatial variation of one component of the magnetic field implies a change of a different component in an orthogonal dimension. However, application of a large external field introduces an asymmetry so that nuclei along the direction in which there is no intended field gradient have negligible Zeeman energy shifts. Thus, the orthogonal plane of nuclei have nearly identical energies and are labeled 'equivalent qubits' (Fig. 4.1a). The equivalent qubits are meant to be identical but non-interacting. Quantum computation still occurs within a row of distinct qubits, but the output signal is enhanced by the multiple copies of spin states.

A spatial variation in the magnetic field can also be introduced in two dimensions. This can be used to create a two-dimensional quantum computer with equivalent qubits existing along rows. A 2-dimensional quantum computer requires an anisotropic field gradient with no spectral overlap along both gradient directions. The anisotropy must be sufficient so that nuclei along the dimension with the larger field gradient are separated in frequency by more than the maximal frequency separation of qubits in the direction with the smaller field gradient. In the case of a two-dimensional computer, the density of interacting nuclei is more than doubled when compared to a one-dimensional quantum computer. For instance, if pulse techniques permit two-bit operations between nearest neighbors, then a 1-dimensional quantum computer allows for up to two neighboring nuclei to be involved in logic operations, while a 2-dimensional computer permits at least 4 (Fig. 4.1b). With certain crystal structures, next-nearest neighbors may also be allowed to interact in this design. This geometry will allow more neighboring nuclei to carry out logic operations, thus reducing bit-swapping.

Alternatively, not all qubits in the crystal lattice need be used. By modifying the pulse sequence we can get the 2-dimensional design described above to behave as a 1-dimensional quantum computer. This mode of operation is physically identical but instead of permitting the computer to have distinct qubits along two dimensions,

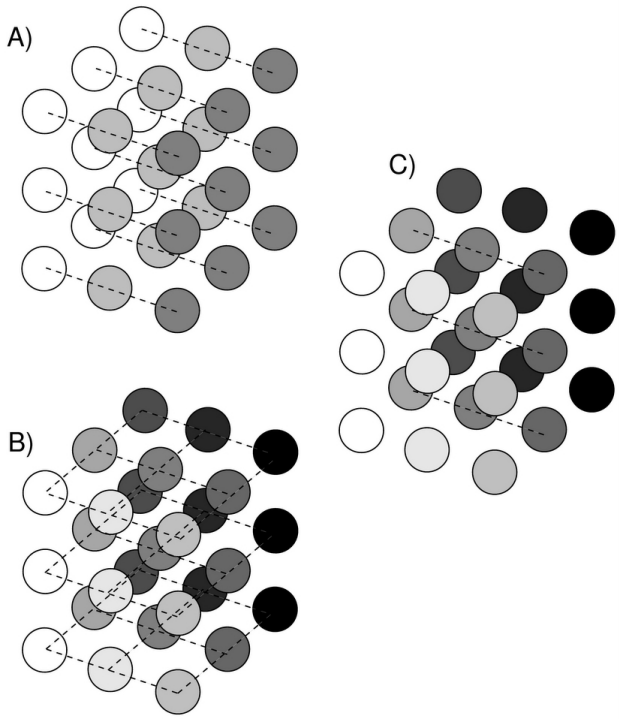

Figure 4.1: Shown are three different forms of quantum computers using nuclei in crystal lattices. The circles represent the nuclei and the shading identifies the Zeeman energy. **a**) Type 1: The quantum computer lies in one dimension with a plane of equivalent qubits which have identical shading. Interactions are meant to occur only along the dashed lines shown. **b**) Type II: This design has a 2-dimensional field gradient and therefore distinct qubits along 2 dimensions. The interactions among distinct qubits as meant to be limited to the dashed lines. The requirement that their be no overlap in the Zeeman energies in the distinct qubits is shown by the anisotropic shading of the two gradient directions. In this design a single nuclei can interact with 4 neighboring or more if next-nearest neighbors are also considered. **c**) Type III: This design is identical to Type II but by use of the proper pulse sequence only the interactions along one dimension are permitted, as shown by the dashed lines.

it acts effectively like a one-dimensional quantum computer with only one dimension of equivalent qubits (Fig. 4.1c). The advantage over the one-dimensional design described above is that elimination of interactions between equivalent qubits (i.e. decoupling) is made easier by eliminating one of the dimensions, and as will be shown in Sec. 4, this configuration also allows for a larger field gradient than the design with a field gradient only in one dimension. Figure 4.2gives a frequency picture of how this type of computer would operate.

In summary, the computers described above can be divided into three types: I) a 1-dimensional quantum computer with equivalent qubits in two dimensions; II) 2-dimensional quantum computers with equivalent qubits in the third dimension; III) a 1-dimensional quantum computer with equivalent qubits in the second dimension, while the third dimension, which has a magnetic field variation, is not used. The choice of design is largely determined by the NMR pulse sequences, the algorithms to be implemented, ease of fabrication and alignment of the magnet to the crystal, and the minimum field gradient required.

4.3 Magnetic Field Calculation

Current-carrying wires allow one to construct an electro-magnet with arbitrary geometries, and the induced magnetic field can be directly controlled through changes in the applied current. Unfortunately, the field gradients with such systems are limited by the current carrying capacity of the wires. Even an optimal metal (e.g. Au) arranged in a Helmholtz configuration operating at a current density of 10^{12} A/m^2 yields a maximal field gradient on the order of 0.01 to 0.1 T/μm which extends for less than 1 μm. Theoretical proposals and reported results with current carrying wires for micromagnetic atom traps on the order of 0.001 T/μm are presented in [65, 66, 67] and up to 0.1 T/μm field gradients are described in [68]. It should be noted that nano-sized current-carrying wires could yield field gradients as large as 10 T/μm as discussed in Section 9.7.

Larger gradients have been realized with ferromagnetic materials [69, 70, 71] such as Tb, Fe, and Dy. Dysprosium (Dy) has the largest value for saturated magnetic

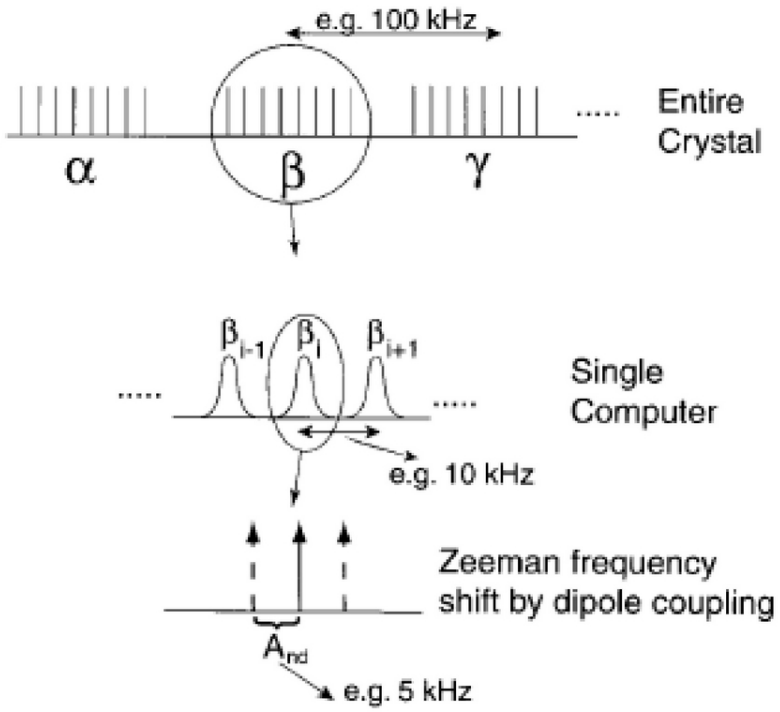

Figure 4.2: A single crystal situated near a 2-dimensional anisotropic field gradient creates a distribution of frequencies as shown in the first line. The larger field gradient separates the qubits into groups whose centers could be separated by 100 kHz, for example. Within each group the smaller field gradient will separate quantum bits by an order of magnitude less or smaller (e.g. 10 kHz). With the proper pulse sequence the quantum computer labeled β could be the operational computer while the remaining qubits are decoupled entirely. The last line shows how the qubits experience frequency shifts due to dipole couplings with nearest neighbors; These shifts serve as the basis for logic operations in crystalline systems [2].

polarization (3.5 to 3.7 T) [71, 72]. Polarization is achieved by the application of an external field of a few tesla. Dy will exhibit ferromagnetism below 180 K and paramagnetism above this temperature except for some low field (less than 1 T) in [73, 74]. To carry out the calculation of the magnetic behavior of a material (ferromagnetic or paramagnetic), we model the material as having uniform magnetization without edge effects due to domain formation.

The calculations begin with the equation describing the field due to a single magnetic dipole:

$$\vec{B}_{\text{dip}}(r,\theta) = \frac{\mu_0}{4\pi}\frac{m}{r^3}(2\cos\theta\hat{\vec{r}} + \sin\theta\hat{\vec{\theta}}), \tag{4.1}$$

where m is the magnetic moment of the electron, and r and θ are the spherical coordinates shown in Fig. 4.3. Then, to calculate the magnetic field due to a slab of magnetic material one integrates this expression over its dimensions and replaces the prefactor with the saturated magnetic polarization, J_s, assuming full saturation is reached. The total magnetic field is then given by

$$\vec{B}_{\text{total}}(x,y,z) = J_s \int_{-\frac{L}{2}}^{\frac{L}{2}} \int_{-\frac{D}{2}}^{\frac{D}{2}} \int_{-\frac{W}{2}}^{\frac{W}{2}} 3(x-x')(z-z')\hat{\vec{x}}$$

$$+3(y-y')(z-z')\hat{\vec{y}} + (2(z-z')^2 - (x-x')^2 - (y-y')^2)\hat{\vec{z}}$$

$$\frac{\mathrm{d}x'\mathrm{d}y'\mathrm{d}z'}{[(x-x')^2 + (y-y')^2 + (z-z')^2]^{5/2}}$$

where W, D, and L correspond to the dimensions of the magnet along x, y, and z respectively, and the origin of the coordinate system is located at the center of the magnet (Fig. 3). This expression is only valid for $x > W/2$, $y > D/2$, and $z > L/2$; i.e. outside of the bar magnet.

This three-dimensional integral yields a closed form solution which does not consider edge fluctuations due to geometrical effects or misaligned domains. The result can be expressed as

$$B_l = J_s F_l(x,y,z,x',y',z') \tag{4.2}$$

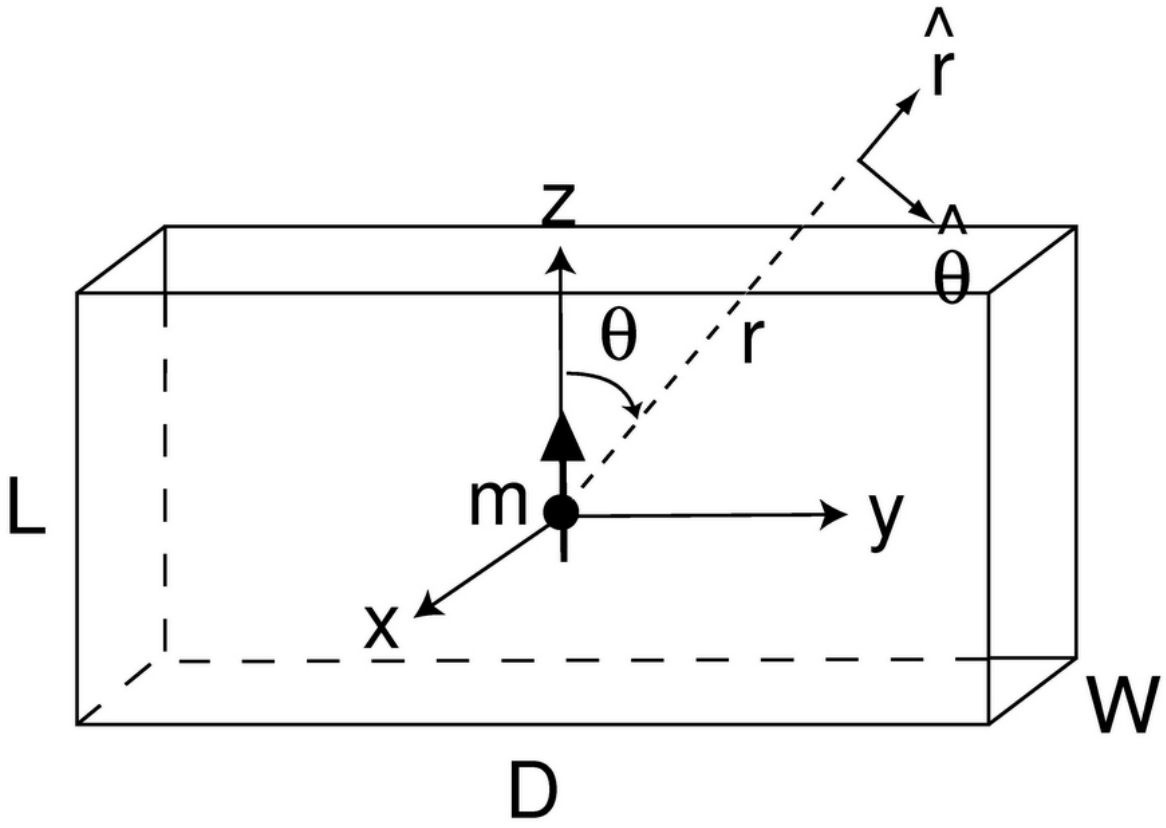

Figure 4.3: A single dipole is shown to be aligned along the z-axis. The standard spherical coordinates r and θ are used. To calculate the field due to a rectangular slab of material one integrates this expression along the 3 dimensions, as shown.

with,

$$F_l(x,y,z,x',y',z') = \sum_{i,j,k=0}^{1} (-1)^{i+j+k}$$
$$G_l[x,y,z,(-1)^i\frac{W}{2},(-1)^j\frac{D}{2},(-1)^k\frac{L}{2}]$$

$$G_x = -\sinh^{-1}\left[\frac{(y-y')}{\sqrt{(x-x')^2+(z-z')^2}}\right] \tag{4.3}$$

$$G_y = -\sinh^{-1}\left[\frac{(x-x')}{\sqrt{(y-y')^2+(z-z')^2}}\right] \tag{4.4}$$

$$G_z = \frac{1}{2}\tan^{-1}\left[\frac{2(z-z')(y-y')(x-x')r}{(z-z')^2r^2-(x-x')^2(y-y')^2}\right] \tag{4.5}$$

where $r = \sqrt{(x-x')^2+(y-y')^2+(z-z')^2}$.

Typically, D is made to be millimeters long. W and L typically will have an aspect ratio of 10 and in the case of the Type I design, L is the longer dimension while in the other designs W would be chosen as the longer one. The following section gives a detailed picture of the expected field gradient and magnetic behavior for the configurations considered in Sec. 2.

4.4 Magnet Designs

4.4.1 1-dimensional quantum computer with a field gradient in one dimension: Type I

In this design the objective is to achieve a large one-dimensional field gradient while suppressing inhomogeneity in the transverse directions. In this way, a plane of nuclei will have nearly identical Zeeman energies. Figure 4.4 presents a possible design using the magnetized material discussed in Sec. 3. At a properly chosen distance d from the magnet in the x-direction as shown in Fig. 4.4 and near the line $z = 0$, the total field is independent of z. However, $\partial B_z/\partial x$ can be large and is used as the field gradient

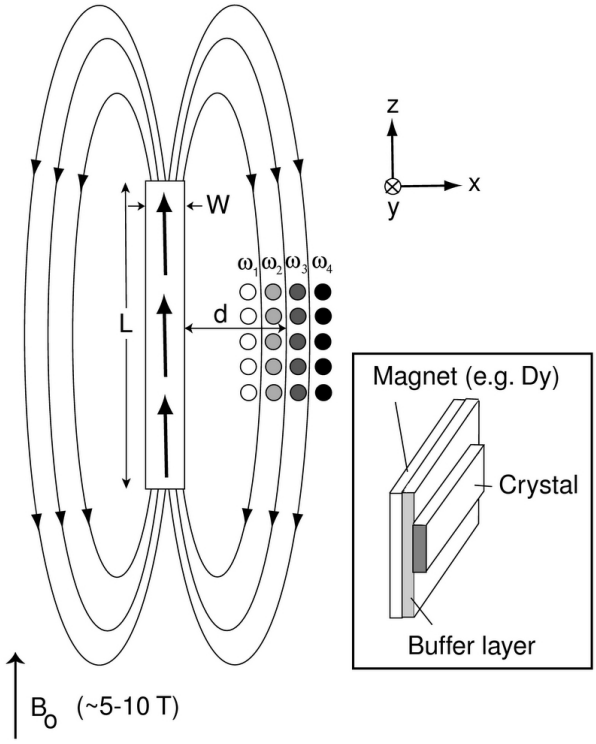

Figure 4.4: A long, thin slab of material is placed in an external field as shown. The sample is placed at $z \sim 0$ and the gradient is along the x-axis. In this realization of the Type I configuration the yz-plane houses equivalent qubits.

to separate the Zeeman energies of the spins. The magnet extends considerably in y, so there are a large number of equivalent qubits in this direction.

As the value of z moves away from $z = 0$ the field varies and the number of equivalent qubits permitted in this dimension is limited by the allowed inhomogeneity. The inhomogeneity is brought about by unwanted magnetic field components in the x direction. When the crystal is placed in a large external field of strength B_0 aligned along the z direction, the shift in the magnetic field is

$$\begin{aligned} \triangle B(x_0, z) &= \sqrt{B_x^2(x_0, z) + (B_0 + B_z(x_0, z))^2} \\ &\quad -(B_0 + B_z(x_0, z = 0)) \end{aligned}$$

where x_0 is the location of a plane of equivalent qubits.

Note that the y-component of the magnetic field is ignored, since the magnet is very long in the y-direction. By symmetry, there should be no field on the line $y = 0$ and, as one moves away from the center, the contribution to the total magnetic field is still negligible until one approaches the edge. Figure 4.5 shows the magnetic field and gradient $\partial B_z/\partial x$ with respect to x for $L = 3$ μm and $W = 0.3$ μm. With these parameters the maximum field gradient achieved is larger than 1 T/μm. By decreasing the value of L or increasing W, larger field gradients can be achieved, but inhomogeneity will grow and reduce the number of available equivalent qubits. The gradient in this configuration persists for the range of 1 μm along the x-axis, so the number of the equivalent qubits can be as large as several thousand. The inhomogeneity permitted will determine the number of equivalent qubits. Fig. 4.6 shows the inhomogeneity, defined by $\triangle B(x_0, z)/[B_0 + B_z(x_0, z = 0)]$, as a function of z for fixed values of x. Assuming the permitted homogeneity should be better than 10 ppm (as is typical in commercial high-homogeneity superconducting magnets) and the external field is 10 T we can allow for $\sim 10^3$ equivalent qubits in z. Since y could be made to be 1 to 2 cm, the number of equivalent qubits could be on the order of 10^7. Thus, with about 10^2 multiple copies of the magnet and crystal configurations the total number of equivalent qubits can be as large as 10^{12}.

Larger field gradients can be achieved by increasing W or decreasing L but both

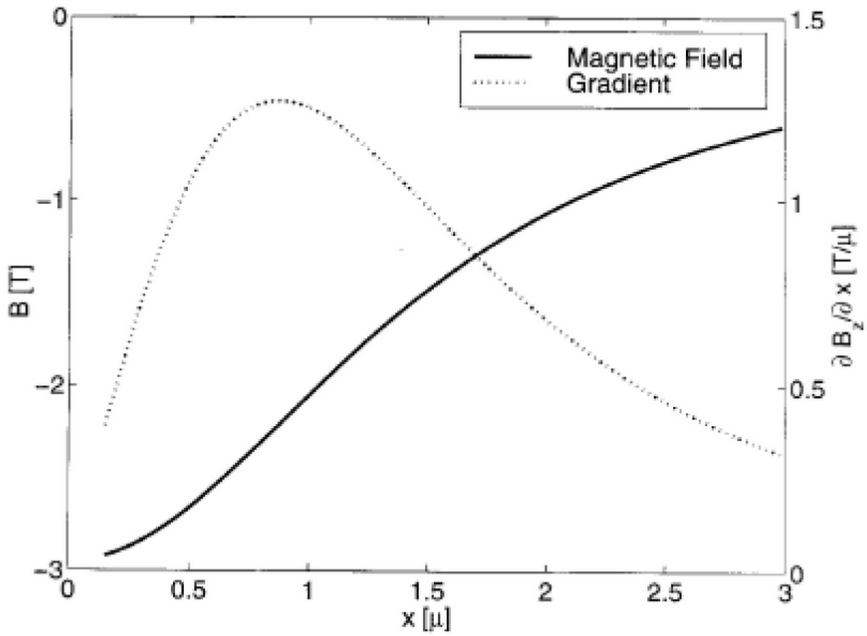

Figure 4.5: For a design with $L = 3\mu$m, and $W = 0.3\mu$m, one can achieve a field gradient of ~ 1 T/μm for over a 1 micron distance.

will diminish the number of equivalent qubits. A parameter search revealed that for $L > 0.5$ μm and $W < 1$ μm (which are reasonable for standard lithographic and metal evaporation techniques), about 10 T/μm appeared to be an upper bound. This field gradient persists over a short distance (0.01 to 0.1 μm) so the number of qubits available for this large a field gradient is limited to hundreds as opposed to thousands.

4.4.2 2-dimensional and 1-dimensional quantum computers with field gradients in 2 dimensions: Types II & III

As mentioned in Sec. 2 the configurations of Type II and III are identical, but differ in their pulse sequences. There are a number of potential designs to consider for this

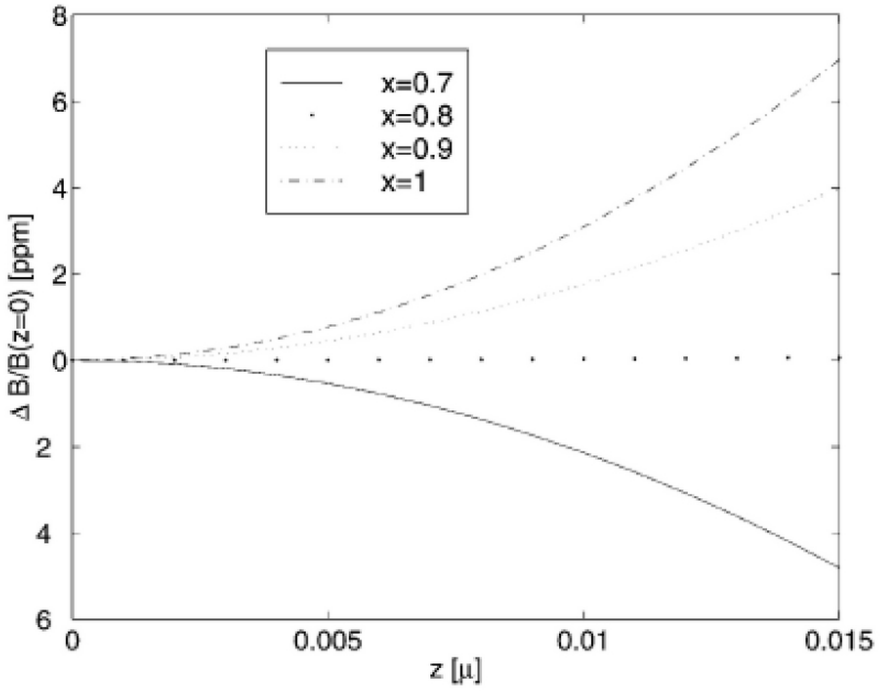

Figure 4.6: This plot shows the inhomogeneity for the 1-dimensional configuration described in Fig. 4.5 at different x positions and as functions of the z-coordinate. The plots show that 10 ppm homogeneity can be achieved over a 0.02 μm range.

class of magnetic fields. Two possible configurations are shown in Figs. 4.7 and 4.8. The design in Fig. 4.7 uses the field profile created around the edge of a single bar magnet. The fields created by such edges have been used for magnetic barriers in 2-dimensional electron gas systems [69, 70, 71]. The crystal is placed below and slightly away from the edge. Depending on the location (x_0, z_0) as defined in Fig. 4.7, the gradient can be anistropic with x or z housing the larger field gradient. Alternatively, by using two closely separated magnets one can achieve larger anistropy in x (Fig. 4.8). This is possible by placing the crystal in the middle of the space between the two magnets and near the point $z = 0$.

A caveat should be mentioned about the Type III computer. There is one potential advantage to having the quantization axis parallel to the axis containing the spins of an individual quantum computer By a single quantum computer we mean the set of spins who line up along the smaller gradient direction and are decoupled from the other non-equivalent qubits through a pulse sequence. Without having to apply any pulse sequences, one can automatically get decoupling between next-nearest neighbors if the angle between them satisfies $\theta = \cos^{-1}\sqrt{\frac{1}{3}}$, which is known as the magic angle [75]. A line of equivalent qubits can be decoupled completely if we orient the magnet and the crystal so that next-nearest neighbors are made to be equivalent. The implication would be that the gradient along the x-direction should be the smaller one. The design in Fig. 4.8 tends to increase the homogeneity in z and although coordinates exist which have the desired anistropy the design shown in Fig. 4.7 is the more natural choice if magic angle decoupling is to be used.

For the single magnet design shown in Fig. 4.7, numerical results for the field and gradients are shown in Figs. 4.9 and 4.10. This design was calculated with $W = 10$ μm and $L = 0.1$ μm. The results show that for $z_o = 0.3$ μm and $x_0 = 5.03$ μm a value of ~ 10 T/μm can be achieved along x and ~ 1 T/μm in z.

In the design with two closely spaced magnets larger anistropy is possible. This design tends to enhance the homogeneity in z near the point $z = 0$. As shown in Figs. 4.11 and 4.12the gradients in x and z are comparable to the previous design but the gradient in x can be enhanced if one moves away from the midpoint between the two magnets.

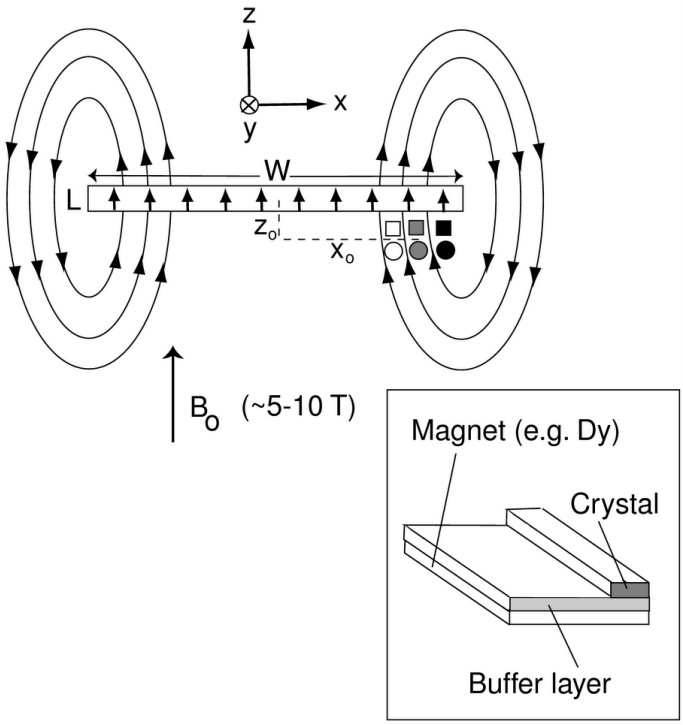

Figure 4.7: W, and L are the dimensions which characterize the cross-section of magnet and (x_o, z_o) locate the center of the quantum computer (Note, drawing is not to scale). The change in shape and shading is meant to show the change in the Zeeman energy.

Both these configurations have only 1 dimension of equivalent qubits so they lose about 10^3 spins compared with the design shown in Fig. 4.4. Thus, 10^8 to 10^9 is a reasonable estimate of the number of available equivalent qubits. As for the actual size of the computer, the increased dimensionality compensates for the decreased extent over which these larger field gradient extend for, so thousands of qubits are still available in the Type II quantum computer.

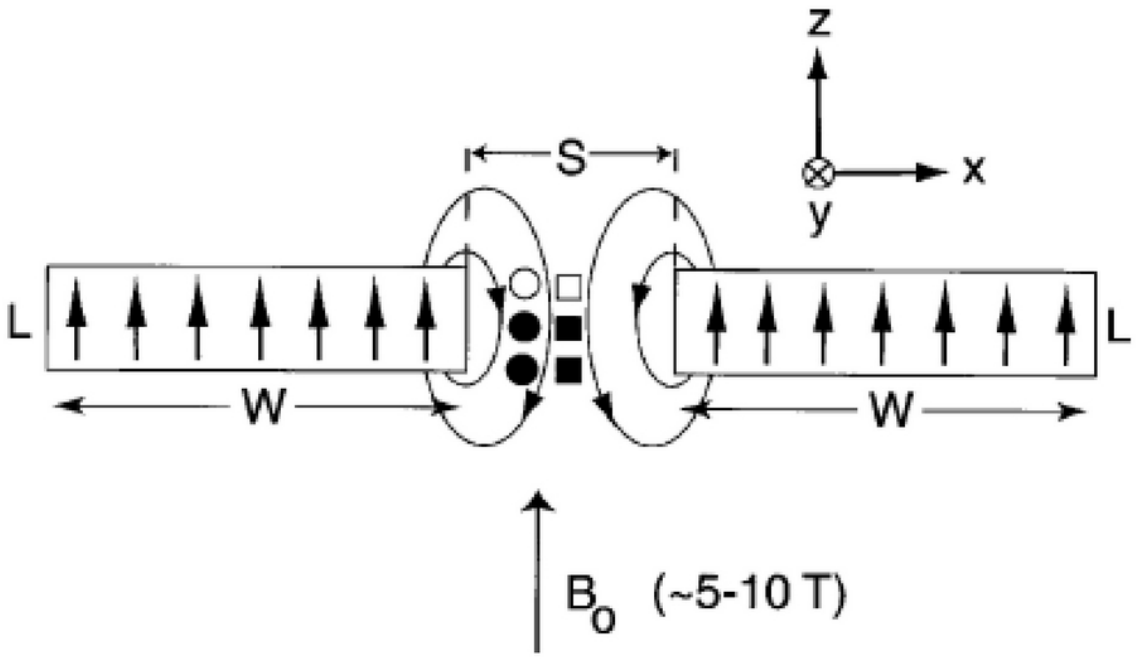

Figure 4.8: Two identical magnets are aligned as shown and the crystal is placed between the magnets. S is the spacing between the magnets and is typically much less than W. Again the shapes and shading are meant to show an anistropy in the field gradients.

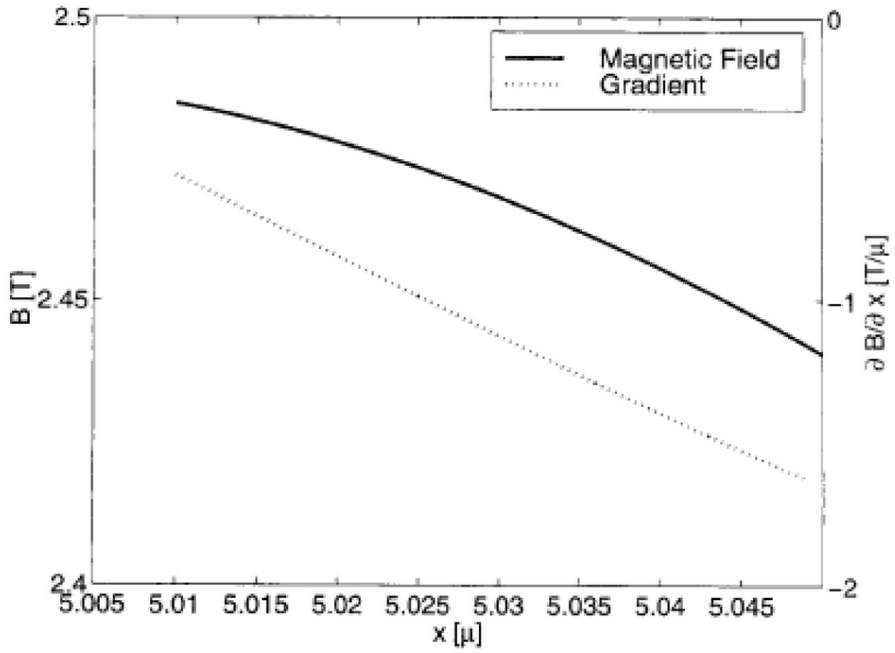

Figure 4.9: For the design drawn in Fig. 4.7 the field and gradient are plotted versus x with $W = 10$ μm and $L = 0.1$ μm. Here z_0 is chosen to be 0.3 μm.

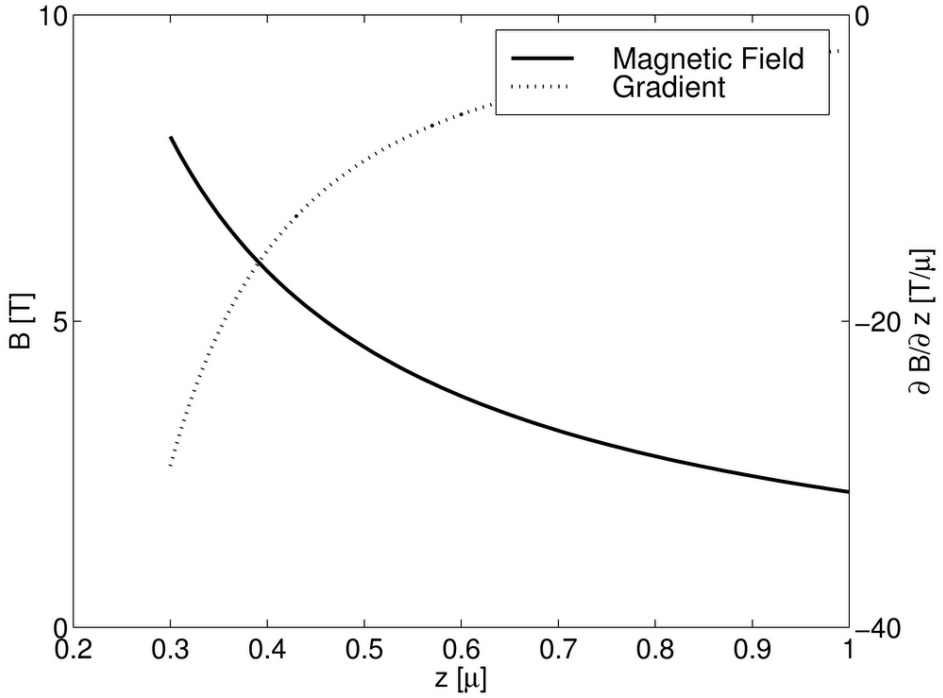

Figure 4.10: This plot shows the field and gradient along the z axis for the parameters desribed in Fig. 4.9. x_0, shown in Fig. 7, is chosen to be 5.03 μm.

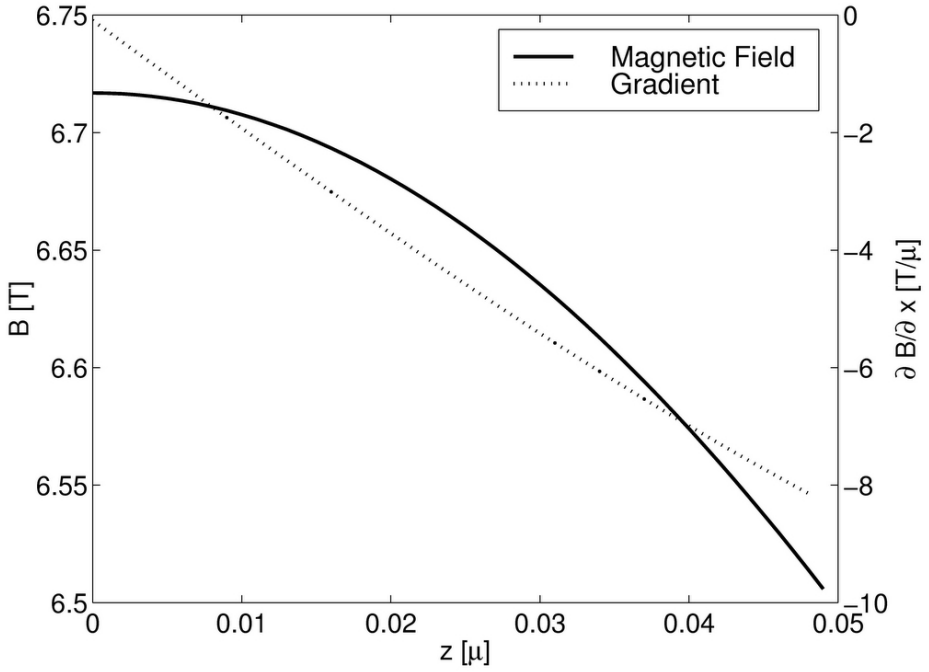

Figure 4.11: Using two magnets side-by-side as shown in Fig. 8 one can get enhanced field gradients. With $W = 10$ μm, $L = 0.1$ μm, $x_0 = 5.35$ μm and S, the spacing, set to 0.5 μm a field gradient along z can be made to be small if the crystalline nuclei are situated near $z = 0$.

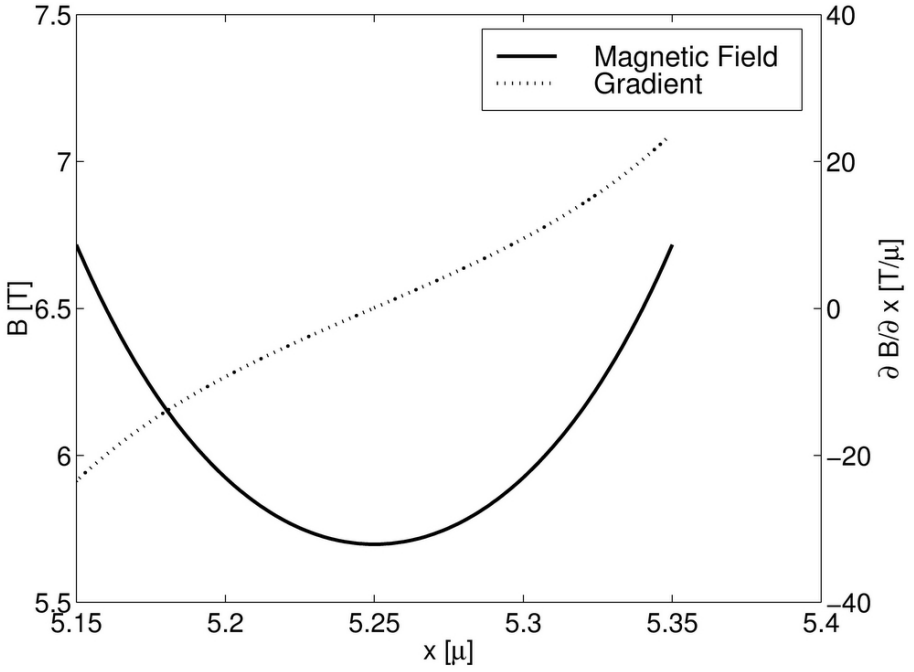

Figure 4.12: This plot shows the field gradient along x for the design described in Fig. 4.8 and with parameters listed in Fig. 4.11. z_0 is set to 0, and thus one can get gradients on the order of 20 T/μm.

4.5 Edge Fluctuations

For Type I, the location of the quantum computer can be such that the crystal is far from the magnet compared to the magnet thickness ($d >> W$). This has the advantage that it is insensitive to physical edge, has an increased number of equivalent qubits, and has an upper bound ($\sim$1000's) for the number of qubits. If a larger field gradient is desired or one with a field gradient in two dimensions Types II and III should be chosen instead. The quantum computer, as shown in Figs. 4.7 and 4.8, must be placed near the edge of the magnet. In such cases, there are concerns about having increased inhomogeneity due to the edge not having uniform structure along the y-direction. A simulation was carried out which modeled the edge of the magnet as having a sinusoidal oscillation along the y-direction as depicted in Fig. 4.13. Note that here we are considering only the effects of the variation in the physical size of the magnets and not multiple domains forming near the edge.

Using the parameters described in Fig. 4.9 for the design shown in Fig. 4.7 a determination of the edge effect was made. Inhomogeneity versus frequency is plotted versus the z position for fluctuation amplitudes (A_0) of 1 nm and 10 nm and with $\lambda = 1$ μm. The inhomogeneity is defined by subtracting a magnetic field produced by a magnet of identical dimensions but without any edge structure from the same design with the edge behavior. This is done for a distribution of positions along y and the resulting histogram gives a distribution of magnetic shifts from the idealized model. The width of this distribution divided by the absolute value of the magnetic field at that coordinate is defined as the inhomogeneity and is shown in Fig. 4.14 in parts per billion (ppb). Even for values of A_0 of 10 nm the inhomogoneity is less than 10^{-2} ppb. This suggests that the macroscopic size of the magnet as opposed to local fluctuations in the edge is the dominant factor. The studies carried out showed little sensitivity to the wavelength of the edge disturbances. Current lithographic techniques using electron beams have the ability to define sidewalls down to less than 10 nm [76], so these results suggest that these magnets can be used to create large magnetic field gradients while also allowing for equivalent qubits along the y-axis.

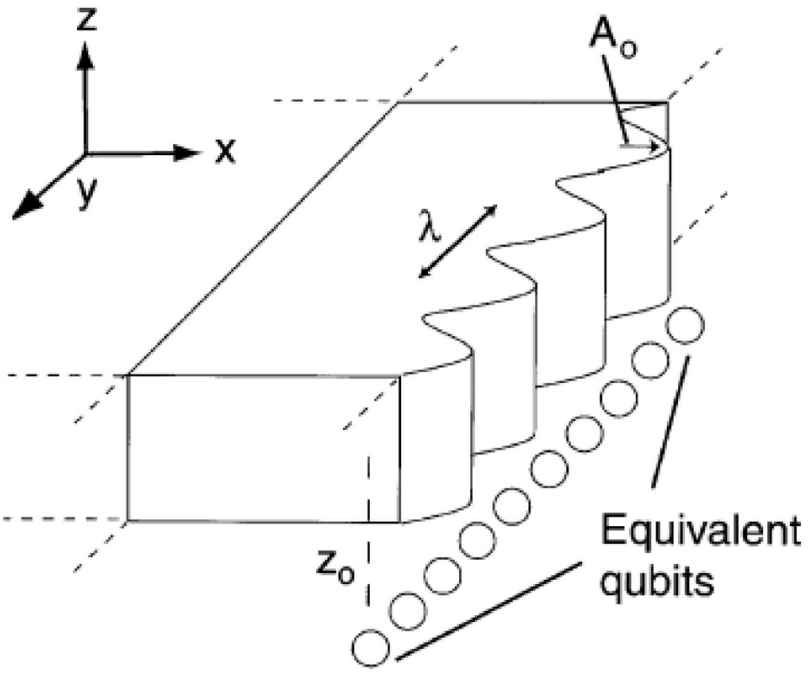

Figure 4.13: The geometry considered for calculating the effect of imperfections in the physical edge. The edge is modelled with some sinusoidal oscillation of wavelength λ, and amplitude A_o. Spectral linewidths are determined by creating a histogram in the distribution of Zeeman energies for equivalent spins situated at coordinates (x_o, z_o) as shown in Fig. 4.7. The circles along the y-axis represent the equivalent qubits whose Zeeman energies are calculated.

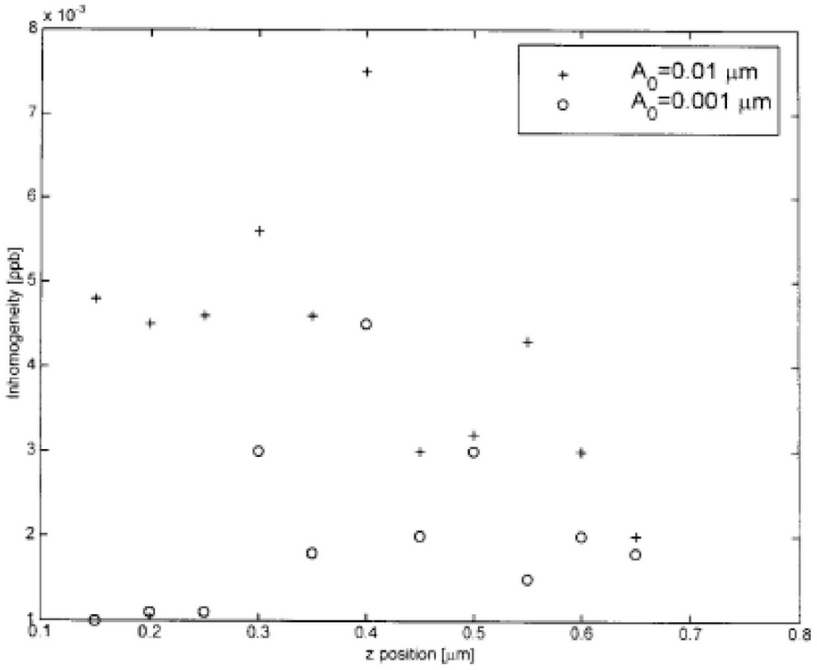

Figure 4.14: Shown is the inhomogeneity in ppb as a function of z for a 1 nm and 10 nm and amplitude fluctuation. The chosen design has $\lambda = 1$ μm, $W = 10$ μm, $L = 0.1$ μm, $D = 200$ μm and $x_0 = 5.03\mu$m.

4.6 Conclusion

Magnetic materials can be used to create micromagnets which have gradients larger that those achievable in current carrying magnets. Such designs can be used to address individual nuclei in a crystal lattice quantum computer. Field gradients of 20 T/μm are achievable with an anisotropic magnetic field variation along two dimensions (Types II & III). Field gradients of up to 10 T/μm are realistic in the Type I design. The use of magnets described in this paper is also applicable to electron spin systems in a crystal lattice or similar systems. The frequency separation for the same field gradient is increased by a factor of 10^3. These magnets hold promise for allowing the observation of atomic layers through nuclear magnetic resonance or a corresponding electron resonance measurement.

Chapter 5

Instrumentation And Experimental Setup

The design and setup of a new experiment requires development, expertise, and money to purchase the necessary equipment. In this section I will present the various equipment and setups I used in a chronological order. My hope is that a future student comes to appreciate the necessary components of doing spectroscopy in a magnetic field and can quickly gain some useful tips. Expertise is most easily achieved from working in the lab with a mentor. This chapter first presents the equipment we used for doing magnetic field studies of dysprosium. After we determined that dysprosium was a suitable material for generating large magnetic field gradients we developed an apparatus for detecting magnetic fields on a nano-meter scale using quantum dots. In order to reach magnetization saturation we required an external magnetic field and initially we used our fixed 7 Tesla (T) NMR magnet. Subsequently we purchased a variable field magnet designed for doing magneto-optical studies. Much of the work related to the nuclear spin-dynamics involved the use of polarized light and timing control over the incident polarized laser light and photoluminescence collection.

5.1 SQUID measurement

Prior to performing spectroscopic studies of quantum dots I first studied the magnetic properties of microfabricated dysprosium. To test the performance of the dysprosium magnet by itself we used a magnetic property measurement system (MPMS) manufactured by Quantum Design. This system is capable of measuring magnetic properties of samples by using a superconducting quantum interference device (SQuID). A sample is mounted and placed in the instrument where the magnetic field near the sample is measured using the SQuID. The system can sweep both temperature and magnetic field and is programmable. With this system we performed studies to characterize the magnetic properties of dysprosium as a function of temperature and magnetic field.

Here I present results from a sample with micron-sized magnets of dysprosium. In order to measure the magnetic field due to the dysprosium we required multiple micron-sized magnets. In this way we could measure the magnetization at different temperatures and for different magnetic fields. The device structure is similar to the one shown in Figure 5.1 except no aluminum was deposited. From this we could determine if the dysprosium behaved as predicted. Indeed, the saturated magnetization was near the known value of 29.89 x10^5 Am [77]. The horizontal line at 350 emu/g corresponds to the saturated magnetization of Dy. The Curie temperature of dysprosium is 85 K and so at sufficiently low temperatures and field strength between 1 and 2 Tesla saturation is reached. The behavior of dysprosium in a higher temperature regime and at varying fields is explored extensively in [78].

5.2 NMR Magnet Setup

Preliminary magneto-photoluminescence experiments were performed in a 7T magnet designed for doing high-resolution NMR. This was not originally intended but initially we planned to only do standard NMR in the magnet. We later decided to pursue quantum dot spectroscopy in a magnetic field and the only available magnet was the 7 T magnet.

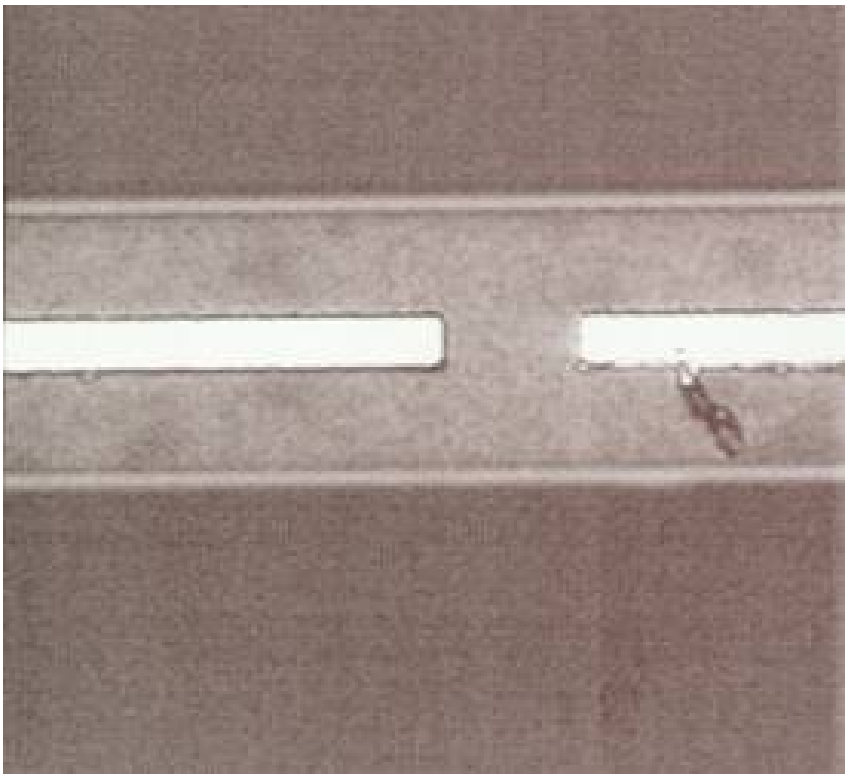

Figure 5.1: This photograph shows a fabricated micromagnet of dysprosium. Above the dysprosium we covered the sample with polyamide and an layer of patterned aluminum. The purpose of the aluminum was to use NMR to measure the effect of the dysprosium magnet and in this way determine if a field gradient was present. This experiment revealed that the aluminum nuclei were too broadly distributed to provide a NMR signal.

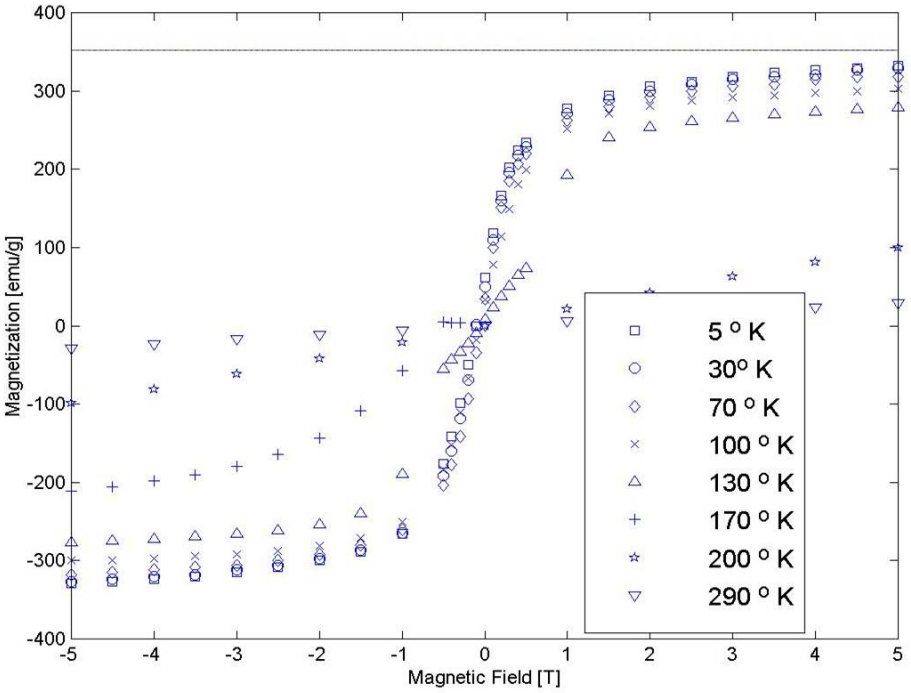

Figure 5.2: Dysprosium magnetization vs temperature and magnetic field. The dysprosium magnetization reaches near saturation (∼350 emu/g) for microfabricated dysprosium.

Figure 5.3: 7 T NMR magnet made by Oxford Instruments. We installed an optical breadboard below the magnet to mount the necessary optics. Aluminum supports screwed into holes on the bottom of the magnet. The laser and monochrometer are located on a standard optical table and all the light to and from those equipment are fiber coupled.

The 7T NMR magnet is a standard one that many companies offer and requires little maintenance. In fact our magnet was manufactured and installed by Oxford Instruments and the only maintenance we performed over a 5 year period was maintaining the cryogen levels. The Oxford engineers did the installation, ramped up the current and set the magnet in persistent-current mode. The magnet remained "on" and required liquid helium transfers every 6 months assuming the liquid nitrogen vessel was filled at least once every 2 weeks.

The magnetic field is created in the center of the magnet by a solenoid coil. Our magnet produces a field of $\sim$7 T and is homogenous to $<$10ppm over a 1cm wide x 2cm tall cylinder in the center of the magnet. The bore of the magnet is open to air and ran through the entire length of the magnet. The 89mm bore is rather wide by NMR standards but nonetheless the central homogenous region is located roughly 1m from either end of the magnet.

Although this apparatus appeared relatively easy to work with it was not ideal for doing magneto-photoluminescence studies on isolated mesas containing quantum dots. This experiment requires a means of exciting the mesa containing the dot of interest and simultaneously an efficient means of collecting the emitted light. This translates experimentally to building a microscope to operate inside the magnet bore and a means to cool the dot to liquid helium temperatures. In addition, many of the studies we were interested in required a variable magnetic field which is not possible with a 7T NMR magnet. However, we realized that we did not require the homogeneity offered to NMR experiments so by lifting the cryostat up or lowering it we could access different magnetic fields. In order to measure the magnetic field we installed a hall probe located about 1.5cm vertically above the sample. Unfortunately, this setup was not ideal since when we moved the crysotat we had to realign our optics.

5.2.1 Variable Temperature Insert (VTI)

In order to control the temperature of the sample we purchased a cryostat designed for the NMR magnet with optical access at the bottom. Figure 5.5 shows an inserted photograph with the sample and window at the bottom of the cryostat. The cryostat is

a standard continuous flow cryostat and the details of its operation can be found in the manual or going to the website of Janis. Similar cryostats for room temperature bore NMR magnets are made by Oxford Instruments and other companies. Essentially, gaseous helium (or liquid) can is pumped through the sample space and cools the sample to 4 K. This cryostat is inserted in the bore of the magnet. With the heater and needle valve controlling the helium flow along with a temperature controller the system can be stabilized to any temperature below 77 K. For operation 77 K liquid nitrogen can be used instead but we only operated at 4 K temperatures.

5.2.2 Sample Holder

The sample holder for this experiment was attached to an insert for the continuous flow cryostat. A support structure with radiation baffles was constructed from stainless steel and brass. Attached to the bottom plate was a support which held the sample and essentially it was a copper plate with screw holes. Typically we mounted the sample using grease to solid piece of copper which we then screwed into this plate. The only required feed-through we used were electrical ones needed for a Hall probe. This became important once we began raising and lowering the cryostat to do measurements in different magnetic fields.

Voigt Geometry

The sample holder was modified at one point when we wanted to study a sample with the magnetic field oriented perpendicular to the growth direction of the sample. This geometry, the so-called Voigt configuration, required that we install a mirror at a 45 degree angle and place the sample such that the growth direction was perpendicular to the applied magnetic field. The modified sample holder is shown in Figure 5.4. This modification was the simplest in order for us to perform these measurements.

5.2.3 Optical Setup

The primary challenge of the microscope was finding a lens that provided good imaging quality and was non-magnetic. This proved quite a challenge. If one used a

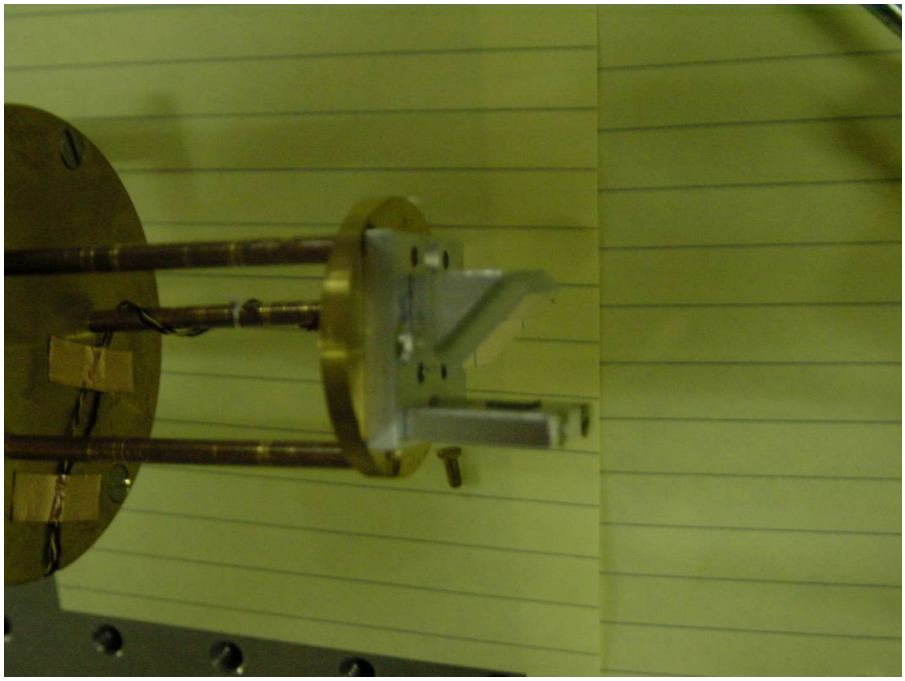

Figure 5.4: This photograph shows the modified sample holder that allowed us to probe the sample in the Voigt configuration. The 45^o portion had a mirror mounted on it and the sample can be seen mounted on the vertical slab. Also note the wires lead to the hall probe which was mounted on the back of the bottom circular plate.

standard single achromatic lens soon after the outer window of the cryostat the image quality was very poor. If instead we used a SLR camera lens we obtained very nice images but the camera lenses generally contained small screws and retaining rings that had were made from magnetic material. These small steel masses were sufficient to be unusable in the magnet. The forces became so large that the springs in the stage on which the lens was connected to via a lens tube (see Figure 5.5) provided insufficient restoring forces to keep the lens from being pulled towards the center of the magnet. The solution we found by chance was the standard 1X objective of a Nikon SMZ800 stereo microscope. This compound lens system provided a decent image quality. We went to the local camera store to find an adapter ring in order to adapt the threads of the camera lens to the threads on the 2 inch lens tube from Thorlabs we used.

5.2.4 Variable Field Access

Once we realized that we needed to do measurements at different magnetic fields we lifted the cryostat to access different magnetic fields. This required use of a Hall probe to calibrate the magnetic field value. The homogeneity for NMR is poor except at the point where the field is 7T but for the purposes of our experiment the homogeneity is sufficient. The difficulty became that the since the Nikon lens was not infinity corrected its position relative to the sample changed as we lifted the cryostat. This led to changes in the delivered laser power and the numerical aperture. At fields near 2 T the cyrostat had to be lifted $\sim$2 ft and the image quality became degraded. One other difficulty is that every time we moved the cryostat we lifted the cryostat with a hoist and added sections to the lens tube. This made doing multiple field values rather time consuming and tedious. It was a welcome relief once we purchased a variable field cryostat designed specifically for doing optics. Nonetheless, with this system we obtained data for quantum dots in the presence of magnetic material.

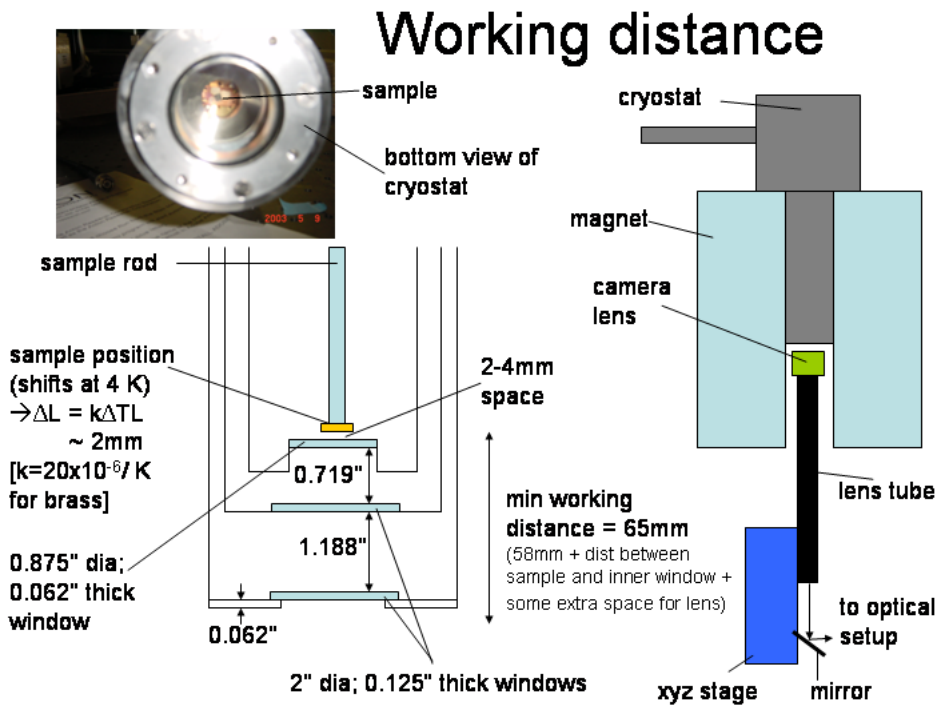

Figure 5.5: Working distance for this system totaled 65mm. The inserted photograph shows the bottom of cryostat with the windows and the sample located in the center region. The lens we used was attached to a lens-tube which then was mounted on a sturdy XYZ stage.

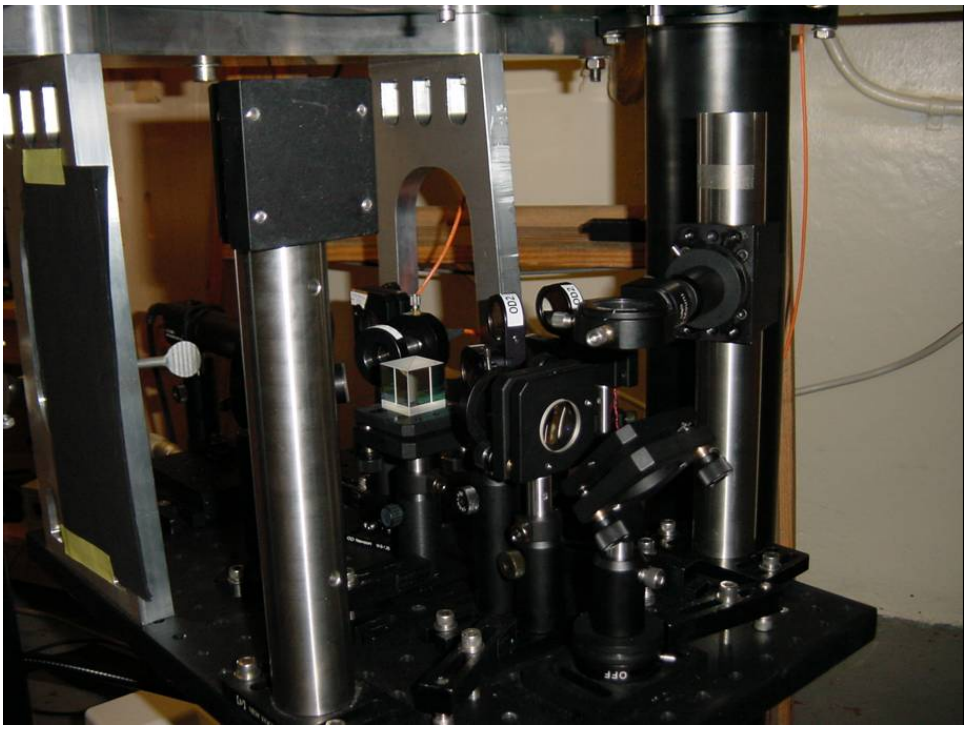

Figure 5.6: This photograph shows the optical breadboard attached to the bottom of the 7T NMR magnet

Figure 5.7: This is the Spectromag magnet. Ours is a maximum of 11.5 T magnet. The coils are located in the bottom portion and the upper portion houses a the liquid nitrogen bath and the vacuum space.

5.3 Spectromag Magnet System

As our group realized that more and more experiments would arise that demanded variable magnetic field spectroscopy we purchased a magnet with this capability that was installed in December 2005. This magnet was optimized for working with smaller samples and we requested that it be designed in such a way that we could bring a window to within 40mm of the sample. The Spectromag magneto-optical superconducting magnet (see Fig. 5.7) system is described in detail in the manuals and at (http://www.oxford-instruments.com/SCNPSC156.htm). In summary the system consists of a vacuum space with a liquid nitrogen jacket and a helium reservoir. The magnet coils are immersed in the helium reservoir and connected to an external power supply provided with the system. By changing the current in the superconducting coils we can change the magnetic field. The system came with a variable temperature insert similar in function to the one described in 5.2.1. The helium source for this VTI is the helium reservoir that keeps the magnet coils cold.

5.3.1 Sample Holder

The system came with a sample rod and mounting plate including ∼24 electrical feedthroughs. However, we did not use any of the feedthroughs. We did install a vacuum sealed BNC feedthrough for connecting an external RF source to a rigid transmission line that delivered rf to the sample. Unfortunately, these experiments were not successful as will be discuss later in Chapter 8.3.2.

5.3.2 NMR coil

The coil used for generating rf waves was a hand-wound copper coil made from a single 2mm gauge piece of wire. This is connected to a rigid transmission line and then connected to the NMR spectrometer. Since the focus of this thesis is not the attempts we made at coupling to the nuclear spins through rf I will not discuss the NMR instrumentation. The details of the rf generators can be found in [17] as well as more discussion about rf circuit design. The coil has 2 sets of between 4-5 turns and we designed it to be split in order to allow for unobstructed optical access.

5.4 Optical Instrumentation

The setup for performing photoluminescence experiments on quantum dots involves a means for exciting the quantum dots with laser light, a means of collecting the emitted light from the quantum dots and filtering the pump light, and finally a means of dispersing the collected photoluminescence. These portions are discussed briefly in this section.

5.4.1 Photoluminescence Setup

The photoluminescence setup consists of the mirrors and lenses needed to deliver the laser light to the sample, form an image of the sample, and collect the emitted photoluminescence (PL). A diagram of the setup is shown in Figure 5.8. The basic idea was to use a glass wedge. This wedge reflects about 3% of incident light so for

the emitted PL most of the light would be transmitted from the sample side to the PL collection side. The laser was polarized as desired and the reflected off the wedge and so most of the light was transmitted through the wedge and not directly along the same path the PL followed. The laser light passed through the 35mm lens and then through a Mitotoyo 10X telecentric lens (working distance is 44mm) in the re-entrant bore tube. Some of the laser reflects directly off the sample and will go along the same path as the PL but by filtering laser light we could remove the laser light from the PL. This is done with cut-on filters or with narrow-band filters. Using this method of filtering the laser light makes it difficult to do PL spectroscopy where the PL is within 10nm from the pump light. For many of our experiments the pump light is tuned to the wetting layer at 850nm and the PL is at 875nm or longer wavelength so this method of filtering was sufficient. However, for resonant excitation or n=2 excited state pumping the experiment became challenging. The PL can then either be sent to a CCD camera where an image of the sample forms so we can see what we are looking at or it is send to the monochrometer where the light is dispersed.

5.4.2 Titanium-Sapphire Laser

The laser source we used was a 3900S Spectra Physics laser pumped by a Millenia diode laser array. The laser is manually tunable from 700nm up to 1100nm and is cw with a almost 3W of available power. Typically we couple the light into a single-mode fiber which creates a clean gaussian mode. In addition as the laser is tuned the beam moves slightly in the laser cavity which can lead to large movement 20ft away at our setup. Thus, coupling into a fiber near the output of the laser allows us to avoid this stability issue as we tune the laser wavelength. One modification we made was to install stepper motors to tune the bi-refringent crystal and the thin etalon so we could automate the laser tuning. This system worked but since we had so many difficulties with doing near-resonant excitation we often worked in the wetting layer. However, for future photoluminescence excitation spectroscopy studies such a system is useful.

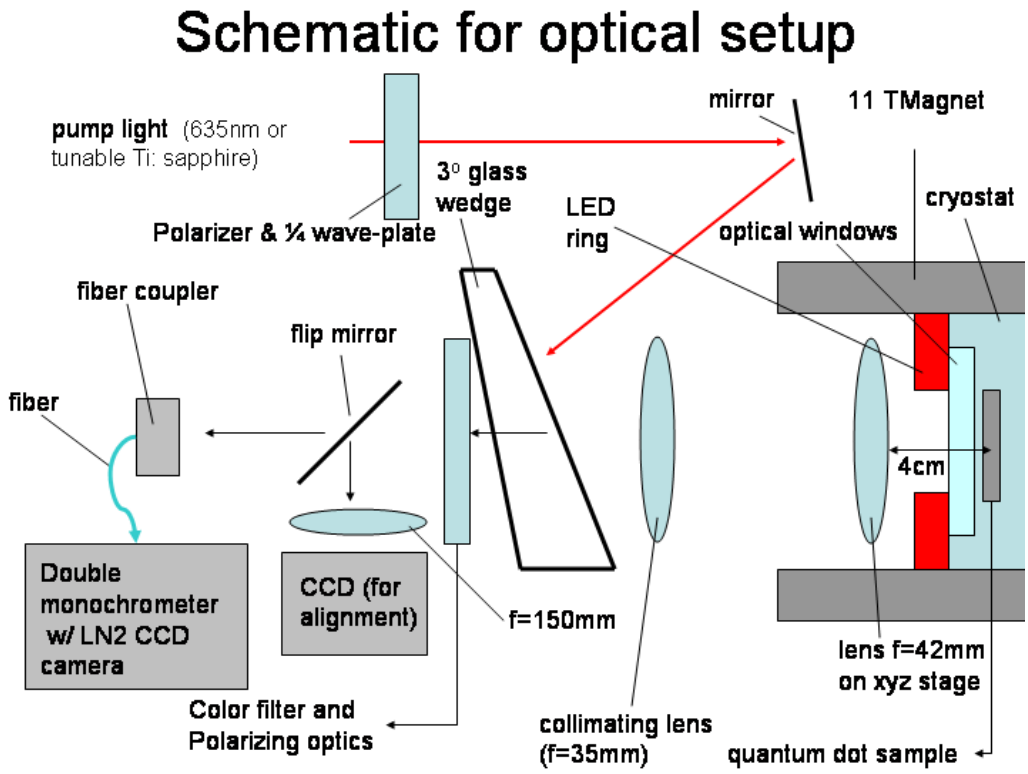

Figure 5.8: Schematic showing optical setup. The laser light is reflected off a wedge and focused via the two lenses onto the sample. The PL is filtered from any scattered and reflected laser light and sent to a CCD camera from which we form an image or toward a monochrometer where it is dispersed.

5.4.3 Monochrometer and Detection

Our monochrometer, a Spectra Pro 750, was manufactured by Acton Research and included 3 gratings. These gratings, with groove densities of 600 mm^{-1}, 1714 mm^{-1}, and 1800 mm^{-1}, provided spectral coverage of about 20nm, 12nm, and 10nm respectively. The highest resolution we achieved with the 1800 mm^{-1}-groove grating is about 0.01nm. The grating could either output the light to a slit or disperse the light onto a liquid-nitrogen-cooled CCD camera (Princeton Instruments LN/CCD) which had pixels of size 13μm x 13μm which helped improve the resolution. Of course there is a fundamental limit to the dispersion offered by the grating for a given input slit width but this increase in pixel density over the standard 26μm pixel size cameras helped with the resolution.

A high precision motor controlled via software allows the grating to be rotated in a reliable and repeatable way. A mechanical shutter is used to control exposure times. Because the camera is nitrogen-cooled long exposure times were possible and the main source of noise is readout. We coupled to this monochrometer by sending light either via free space from the photoluminescence setup or collecting the light into a fiber and sending it to the monochrometer.

5.4.4 Polarization Optics

We can chose the electron spin (and hole spin) direction we excite into the semiconductor by shinning circularly polarized light. A single photon carries angular momentum. In the case of circularly polarized light the classical description is easily to reconcile with the individual photon picture. Photons have intrinsic spin angular momentum of either $-\hbar$ or $+\hbar$ which means they can impart this angular momentum onto an exciton. However, for plane polarized light at the photon level there is an equal probability of the photon to impart either $-\hbar$ or $+\hbar$ and at the single photon level we write the angular momentum state as a superposition state of $\frac{1}{\sqrt{2}}(|\,|\sigma_+\rangle + |\sigma_-\rangle)$. We can use standard polarization optics to introduce the desired polarization. To create circularly polarized light, we use a polarizer followed by a quarter-wave plate (QWP) which is oriented at 45^o relative to the fast or slow axis. We can describe

the polarization state of classical light using a Jones vector, which is a column vector comprising of the x and y components of the electric field. In general we can write the Jones vector as

$$\mathbf{E} = \begin{bmatrix} E_x(t) \\ E_y(t) \end{bmatrix} \tag{5.1}$$

. Since we are using a laser, a coherent form of light, the time-dependence of the electric field can be ignored so long as we keep track of the phase information. Namely at a given point in space and time along the path of a coherent wave we may write

$$\mathbf{E} = \begin{bmatrix} E_{0x}e^{i\phi_x} \\ E_{0y}e^{i\phi_y} \end{bmatrix} \tag{5.2}$$

. Then, to determine the polarization at a different point in time or space we can calculate it easily assuming plane wave propagation along z by using the formula $\mathbf{E}_(z,t) = \mathbf{E}_0 e^{kz-\omega t}$. A horizontally polarized state is given by

$$\mathbf{E}_h = \begin{bmatrix} E_{0x}e^{i\phi_x} \\ 0 \end{bmatrix} \tag{5.3}$$

5.4.5 Polarization Optics

We can choose the electron spin (and hole spin) direction we excite into the semiconductor by shinning circularly polarized light. A single photon carries angular momentum. In the case of circularly polarized light the classical description is easily to reconcile with the individual photon picture. Photons have intrinsic spin angular momentum of either $-\hbar$ or $+\hbar$ which means they can impart this angular momentum onto an exciton. However, for plane polarized light at the photon level there is an equal probability of the photon to impart either $-\hbar$ or $+\hbar$ and at the single photon level we write the angular momentum state as a superposition state of $\frac{1}{\sqrt{2}}(|\,|\sigma_+\rangle + |\sigma_-\rangle)$. We can use standard polarization optics to introduce the desired polarization. To create circularly polarized light, we use a polarizer followed by a quarter-wave plate (QWP) which is oriented at 45^o relative to the fast or slow axis. We can describe the polarization state of classical light using a Jones vector, which is

a column vector comprising of the x and y components of the electric field. In general we can write the Jones vector as

$$\mathbf{E} = \begin{bmatrix} E_x(t) \\ E_y(t) \end{bmatrix} \tag{5.4}$$

. Since we are using a laser, a coherent form of light, the time-dependence of the electric field can be ignored so long as we keep track of the phase information. Namely at a given point in space and time along the path of a coherent wave we may write

$$\mathbf{E} = \begin{bmatrix} E_{0x}e^{i\phi_x} \\ E_{0y}e^{i\phi_y} \end{bmatrix} \tag{5.5}$$

. Then, to determine the polarization at a different point in time or space we can calculate it easily assuming plane wave propagation along z by using the formula $\mathbf{E}_(z,t) = \mathbf{E}_0 e^{kz-\omega t}$. A horizontally polarized state is given by

$$\mathbf{E}_h = \begin{bmatrix} E_{0x}e^{i\phi_x} \\ 0 \end{bmatrix} \tag{5.6}$$

5.4.6 Timescale Measurements

In addition to doing standard photoluminescence we developed a way to dynamically change the polarization of the pump laser and collect photoluminescence at specified times after changing the pump polarization. The reason for implementing this will become clear in Section 8.2.1 but suffice it to say that under different pump polarization the spectra appeared different. This prompted us to investigate how quickly the spectra would change after changing the pump polarization. This was implemented by using a polarizing beam splitter (PBS) to split the pump laser into horizontally and vertically polarized light as shown in Figure 5.9. Then on each path we placed a mechanical shutter which can be controlled by TTL pulses. The light is recombined on a non-polarizing beam splitter and then after passing through a quarter-wave plate the laser light becomes $\sigma_+$and σ_-. The emitted PL from the quantum dots also passes

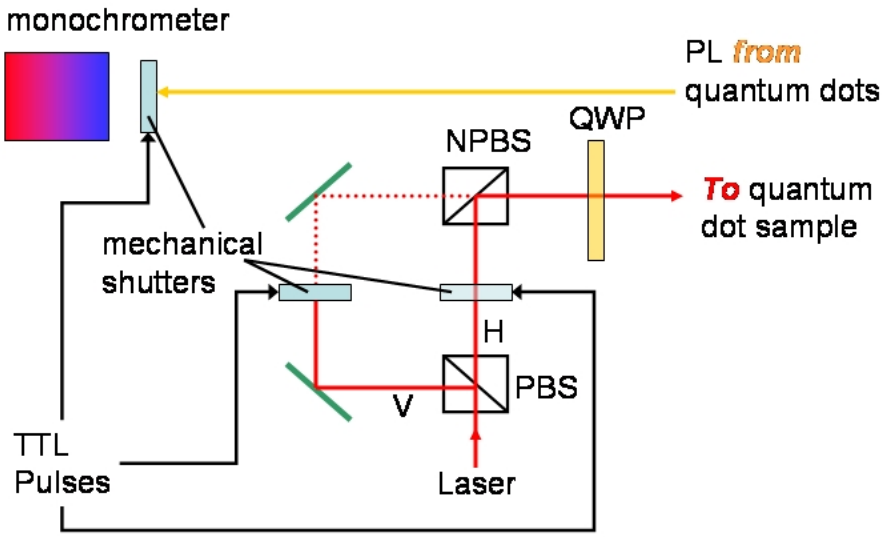

Figure 5.9: By sending the laser through a polarizing beam splitter (PBS) the laser is split into horizontally (H) and vertically (V) polarized light. Each path of the split laser light has a shutter installed which is controlled with TTL pulses. The light is recombined on a non-polarizing beam splitter (NPBS). The light then passes through a quarter-wave plate which converts the H and V light to $\sigma_+$and σ_-light. The light entering the monochrometer also passes through an identical mechanical shutter also controlled by TTL pulses.

through a shutter since the mechanical shutter included in the monochrometer does not have a fast enough response time or high repitition rate to be useful. The shutters we used were LST200SLP made by NM Laser products which have 300μs switching speeds and can operate as high as 150 Hz.

Chapter 6

Fabrication

All of this work would not be possible without the discovery of self-assembled quantum dots. The growth of such materials is itself a active areas of scientific inquiry and I briefly mentioned how the samples are grown. This chapter also explores the fabrication techniques we used and in particular highlights some of the processes I developed for integrating a magnetic structure with quantum dots.

6.1 Quantum Dot Creation

The quantum dots studied in this work are created via self-assembly. They naturally form at the interface between GaAs and a few monolayers of InAs which is further capped by more GaAs. The growth technique and means of isolation are discussed here.

6.1.1 Molecular Beam Epitaxy (MBE)

Fabrication of InAs quantum dots begins with a high-quality GaAs semiconductor wafer which can easily be purchased. These clean wafers are treated to remove water and other contaminants from the surface and immediately loaded into the ultra-high vacuum ($\sim 10^{-11}$ to $\sim 10^{-12}$ range) chamber of a molecular-beam epitaxial (MBE) [**?**] machine. Further heat treatments within the chamber help ensure that residual

water vapor and other atoms desorb from the surface.

MBE is a technique developed in the 1970's for producing high-quality semiconductor films. It works by heating a solid source which produces a small flux of atoms or molecules. The atoms strike the wafer, which is also heated, and this allows the atoms to diffuse along the surface easily and typically come to rest at a step edge where a new layer of atoms is forming. Additionally, the atom flux is small and typically stabilized to better than 1%. These conditions allow for single atomic layer growth. Much expertise is required to maintain an operational system and grow different materials with varying properties.

The formation of quantum dots of InAs comes about from the strain that arises from the lattice mismatch between the GaAs substrate and the InAs layers that are deposited. The first monolayer (MLs) of InAs actually match the GaAs substrate but are under strained. At some point during the addition of more InAs the system becomes strained to the point that small islands of InAs form instead of the standard smooth single atomic layers. There is some residual InAs material that remains and forms a roughened quantum well called the wetting layer. This occurs at varying numbers of monolayers and the size of the islands can also varying depending on the atomic flux and the growth temperature. The islands can range in size from 4-7nm and can be about 20-40nm in diameter. The shape appears like a squashed cylinder but atomic force microscopy (AFM) images often show the localized InAs content to be pyramid-like. This growth technique for making self-assembled quantum dots is known as the Stranksi-Krastanov growth process [79]. The growth concludes by protecting the dots with a capping layer of GaAs. Otherwise the quantum dots can become optically inactive as the surface can accommodate trapped charge states which can quench their nice optical properties.

The density of dots that form and the optical emission properties varies according to the growth conditions. It should also be noted that in practice even a single wafer may have variation it the dot properties and density, and it can be hard to reproduce the same wafer since the exact growth conditions are not always known precisely. It is also worth mentioning that allow these dots are primarily InAs there is some annealing that occurs and this causes the island to contain In, As, and possibly small

amounts of Ga. Also, the wavefunction describing the trapped exciton may extend beyond the island and be affected by the lattice outside of the island of InAs. The bandgap for the tertiary semiconductor $In_{1-x}Ga_xAs$ has been studied at 2 K [54, 45] but the size of the dot also affects the energy level structure. Also, the g-factor of the exciton[1] is determined by the Luttinger-Kohn Hamiltonian which is affected by various lattice parameters.

Figure 6.1 shows the experimental results of the variation of InAs QD density with the change of the InAs QD growth temperature at 1.89ML InAs coverage. Under the high growth temperature, we obtain the lowest InAs island density ($\sim$20 per μm^2), while the height and base diameter of InAs QDs increase with the temperature, which shows a trend of low density-large size. During SK growth with kinetic model, adatoms adsorbing to the wetting layer from deposition process are assumed the only mobile surface species. Diffusion adatoms meet bond together and form small 2D islands. Mobile adatoms hop randomly on the InAs wetting layer around nearest-neighbor sites dependent on the surface diffusion constant [80, 81], which is mainly decided by the growth temperature. The increase of the growth temperature enhances the mobility of In adatoms on the InAs wetting layer surface, which decreases the accumulation of atoms on the top of 2D islands. Hence, the speed of conversion of 2D islands to 3D islands would decrease.

6.1.2 Isolation

Typically, the dot density varies between 10 μm^{-2} and 500 μm^{-2} and due to inhomogeneous broadening, spectral isolation of a single dot would be impossible. In order to isolate a single quantum dot we physically remove most of the dots by selectively etching through the layer of material containing the quantum dots and leaving small mesas which contain only a few quantum dots as show in Figure 6.3. The subsequent sections detail the recipes for fabricating including the electron-beam lithography and reactive ion etching. Another option is to use a mask with a small aperture. The mesa size ranges from 100 nm to 2 μm. With the $1\mu m^2$ mesas it is still possible with

[1]The term g-factor when applied to the exciton is not necessarily just the sum of the hole and the electron g-factors. This is discussed in Section 2.5.5.

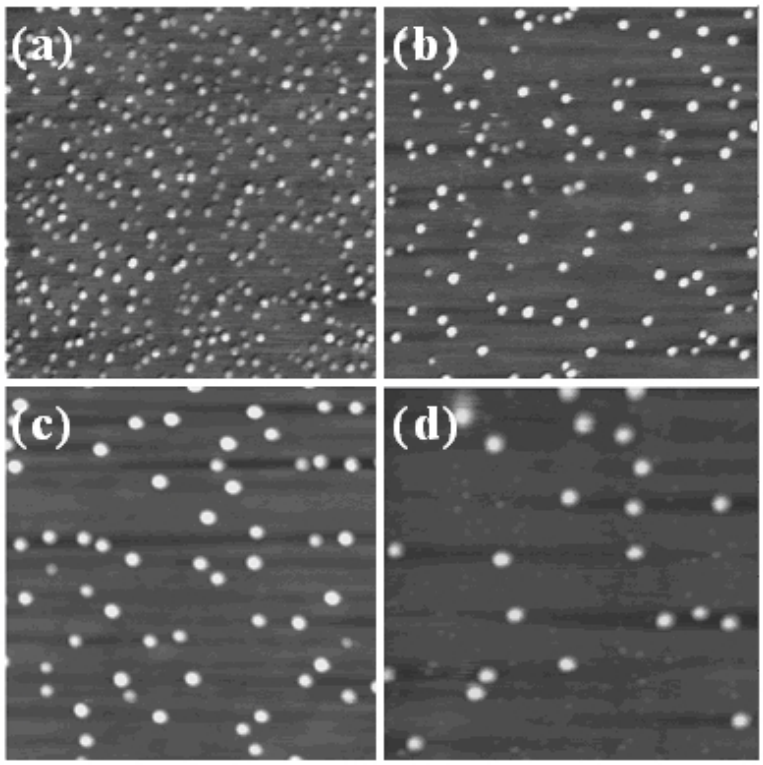

Figure 6.1: AFM images of InAs QDs grown on (100) GaAs substrate with 1.89ML InAs coverage by MBE at growth temperatures of (a) 475, (b) 482, (c) 505, and (d) 525. The growth rate of InAs QDs is 0.07ML/s, and ratio of As to In is about 50. The measured area is 1x1 μm^2.

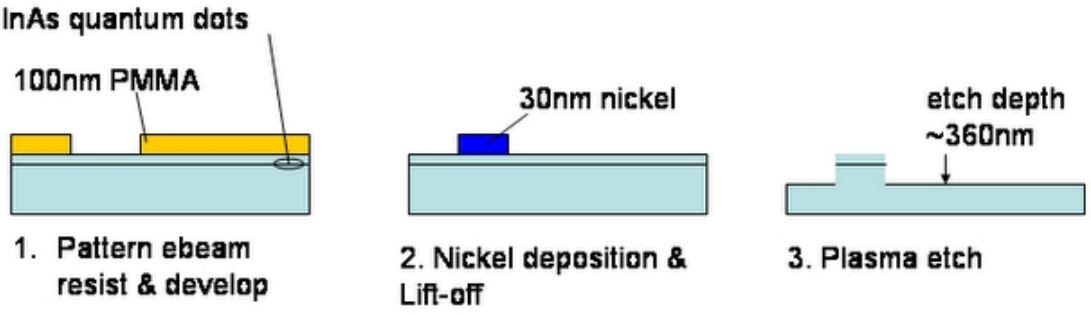

Figure 6.2: This procedure diagrams the method we use to etch mesas for isolating a small number of quantum dots. 1) We coat the positive e-beam resist which we expose using electron beam lithography. After developing in the e-beam developer a region of the resist is removed. 2) We can deposit a thin layer of metal such as nickel which covers the entire wafer. After using acetone to perform lift-off the nickel that adhered directly to the wafer remains while the nickel that was deposited on the resist is removed. 3) We can now etch into the wafer and etch past the layer containing quantum dots except where the metal protects the substrate. We can subsequently remove the nickel with a nickel etch and we are left with isolated mesas with dimensions as small as 100nm X 100nm containing just a few quantum dots.

a high resolution monochrometer to spectrally isolate a single quantum dot. For the samples we worked with the dot density is relative low at tens of dots per square micron.

The sample from which most of the data is taken comes from wafer 903 grown in 1999 and also the subject of the thesis of other students from our group. Many wafers have been grown since then that have similar optical properties. This sample had relatively sparse quantum dots with a density at around 11 μm^2 and they were capped with 75nm of GaAs.

Many other samples were grown with different capping layer thicknesses and some with multiple layers of quantum dots. These were made for experiments intended to place quantum dots at specific locations from the top surface and remain useful for future research towards field gradient studies and Overhauser effect studies with integrated magnets.

6.2 Magnet Fabrication

In order to integrate magnets near the quantum dot different approaches were taken. One approach is to deposit tiny magnets horizontally displaced from a mesa. This requires an aligned electron-beam write between the first layer which contains the mesas and a new layer which is to contain the magnet. In fact this is precisely what we did and the e-beam pattern was designed to vary the position of the magnet with respect the mesa location. In this way, assuming uniform magnets, we could image the magnetic field and draw conclusions about the field gradient produced by such a structure. It turned out that this approach yielded poor results primarily due to poor adhesion of the magnet and a dynamical shawdow-masking effect which caused the sidewall to have the shape shown in Figure 7.4. Serendipitously, one set of magnets actually landed directly on the mesas. Not only did these magnets get placed where they weren't intended but small openings in the magnets formed allowing optical access to the mesas now located within a magnet. This fortunate outcome produced some interesting results which are discussed in Chapter 7.

6.2.1 Electron Beam Evaporation

Electron beam deposition of metals works by focusing a beam of electrons on a metal source. A filament supplies a steady source of electrons which are accelerated towards a target metal. The metal heats up over time and causes clusters of metal atoms to sublime. Effectively the metal locally becomes very hot from the focused electron beam. The beam can be slightly defocused or have some intended jitter to distribute the electrons over a region containing metal. Typically the metal is loaded into a crucible made of graphite or platinum which has a high-melting temperature.

The metal then uniformly covers the surfaces of the chamber of an evaporation station including a region containing the sample. Typically, the sample can be protected by a shutter so that once a stable deposition rate is established the amount of time the sample is within the flux of atoms can be timed and therefore the amount of deposited material can be accurately estimated. A quartz crystal is used to measure the deposition rate. By measuring the resonance frequency of the crystal the mass of

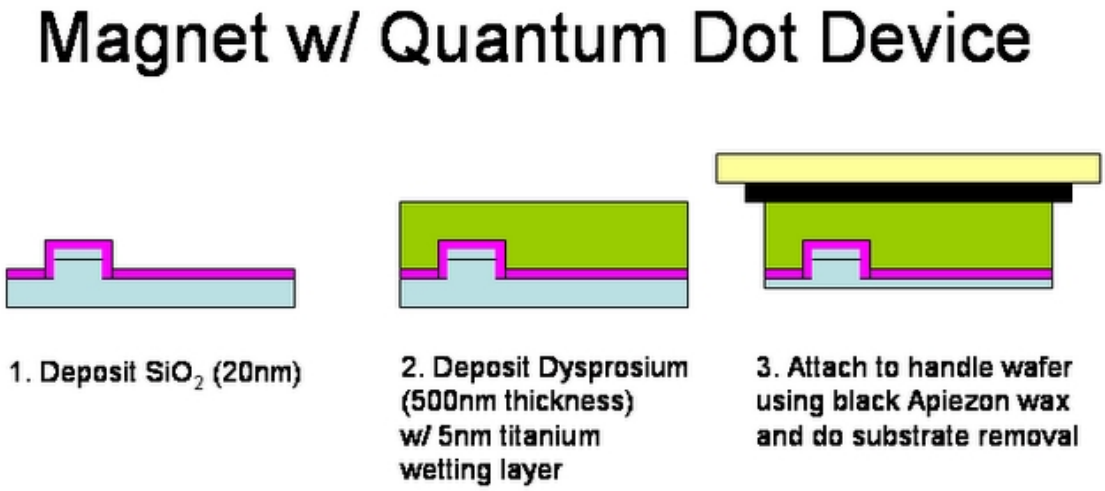

Figure 6.3: This diagram shows the major steps necessary to make an integrated device to introduce a magnetic field gradient across the quantum dot. 1) After obtaining a sample with suitable mesas we can deposit a buffer layer of SiO_2 using the STS chemical vapor deposition chamber. This layer can be of variable thickness and helps ensure that the quantum dots are located near the center of the void within the magnet. Also, it can help with providing a smooth surface on which deposit dysprosium (Dy). 2)Here we deposit sufficient magnetic material by evaporating Dy on to the wafer. An alternative is to sputter a material such as FeCo which would ensure better sidewall coverage. Sputtering heats the sample more and this could damage the sample. 3) Finally, we use wax to attach the wafer to a handle wafer such as quartz. Then we do a wet chemical etch as outlined below. The material that remains is very thin and the quartz is necessary to handle the sample without damaging the quantum dots.

the crystal plus deposited material can be monitored. Some deposition stations also have the ability to rotate the sample so that the flux is averaged out and dynamical shadow-masking effects are minimized.

One disadvantage of evaporation is that clumping tends to occur and the deposited metal has graininess. Typically, atoms travel 50 cm and hit the sample and immediately stick as the sample is kept at room temperature. Sputtering is an alternative technique that be used. However, lift-off is not possible as sputtering is done at higher temperatures and destroys the e-beam or photo-resist layer. The distance between substrate and sample is typically 10cm and the atom flux coats sidewalls quite easily so this also makes lift-off difficult. However, the sample coverage is better and the grain size is much smaller.

6.2.2 Lift-off Process

For samples that have a layer of metal deposited on patterned e-beam or photo-resist it is necessary to remove the unwanted metal. This can be done by immersing the sample in acetone. Acetone is able to dissolve the resist and can access the resist through the sidewalls and the wafer edge. Thus, for samples with complete sidewall coverage lift-off is difficult often has undesirable effects. Gentle sonic agitation can help the process of lift-off.

6.3 Clean Room Processing

Here I present a novel process I developed for building a device for embedding the quantum dot in a dysprosium micro-magnet. The details for the mesa fabrication are standard. This process will be particularly important for future devices where quantum dots with an integrated magnet are desired. For the work I present in Chapter 8, the focus of this thesis, the devices essentially inlcuded only steps 1 through 3. In addition I removed the thin layer of nickel using a nickel etch in the Ginzton clean room. This improves the photon flux from the quantum dots.

1. First layer write

PMMA coat of 2% 950 K spun at 5krpm for 30 sec; [Headway]
Unaligned ebeam write with dosage of 120 μC [Raith]
Develop using MIBK for 45 seconds [E-beam solvent bench]

2. Nickel deposition and lift-off 30nm nickel layer [McCullough Annex or Tom Carver]
   Acetone soak and gentle ultrasonic agitation.
   (Alternative metals such as chromium also works)

3. GaAs Dry etch 200 watts for 2 minutes (etch rate is 180nm/min) [PlasmaQuest]
   Depth = 360nm

4. Deposit SiO2 Deposition rate is 1nm/sec. [STS] Deposit 500nm of Dysprosium 5-10nm titanium wetting layer helps adhesion. [McCullough Annex]

5. Attach to handle wafer Use Apiezon black wax and attach to 1cmx1cm quartz piece. [Crystal Shop]

6. Substrate Removal (Please see below for more details) 1:8:1 H_2SO_4:H_20_2:H_20 wet etch at 10μm/minute until within 50-100 μm of the AlGaAs layer. 97% H_20_2 and 3% NH_4OH will stop at AlGaAs layer 1:1 HCl: H_20 will remove AlGaAs layer which otherwise will oxidize easily.

Substrate Removal

Here I present more details regarding the substrate removal process I used. Other variations exist but I found this process a reliable way. Please be aware that the remaining sample is very brittle and contains a thin layer of GaAs and quantum dots. Also note that large wafer pieces are advantageous in that better contact between the wax and the substrate wafer can be achieved.

1. Use a 1:8:1 water:peroxide:sufuric mix. It is easiest to use 30ml:260ml:30ml mixture. Mix the water and sulfuric first, as it will heat up. Wait for it to cool back to less than 25^o C. Then add the peroxide.

2. Use the spin bar and a spider like 4 inch wafer spring holder thing on top of the spin bar to stir the solution. Etch rate will be about 10μm per minute.

3. When you have 50-100μm left, stop etching. Pour the mixture into a hazardous waste container and dispose of properly.

4. Mix 97% peroxide, 3% Ammonium Hydroxide

5. Again use the stir bar. Stirring is very important. If you do not stir very hard, you will develop an oxide on the surface of your sample which does not etch very fast at all. This etch will then take forever. You may develop some places which don't etch well anyway. Just wait it out. Your etch-stop (300nm of 90% or more AlAs) should be able to stand up to this etch for at least maybe 2 hours. It will stand up less if you take it out of the etch and rinse it many times so avoid doing that when you can. The etch rate will be 1.5-2 μm per minute.

6. After all the GaAs has cleared, you can etch off the AlAs layer in either BOE 6:1 (quick dip, maybe 30 seconds, just watch it till you see it clear), or with 1:1 HCl and water.

Chapter 7

Magnetophotoluminescence of Quantum Dots

In this chapter I will present typical spectra from InAs quantum dots in a magnetic field. We can compare these data to the model developed in Sec. 2.4. We can study how the g-factor varies and also how much diamagnetic shift is present. Finally, and most importantly, we will use the magnetic field dependence to explore the use of quantum dots as magnetic field sensors. Using the quantum dots as a nm-sized magnetic field sensor we can verify that the fields created by sub-micron magnet geometries are as calculated. In this sense we can experimentally make some conclusions regarding whether field gradients greater than 1 T/μm are realistic.

7.1 Sample Spectra for Faraday Geometry

A typical set of spectra from a mesa containing a single quantum dot is shown in Fig. 7.1. These data were taken in steps of 0.5T from 0 to 7 T using the 11.5T variable field Oxford Spectramag. The quantum dot was excited using above-band excitation with a red diode laser.

From this data we can determine the center position of the emission and from these fitted parameters determine the Zeeman splitting at each magnetic field value. If we know the magnetic field applied and have measured a splitting value we can

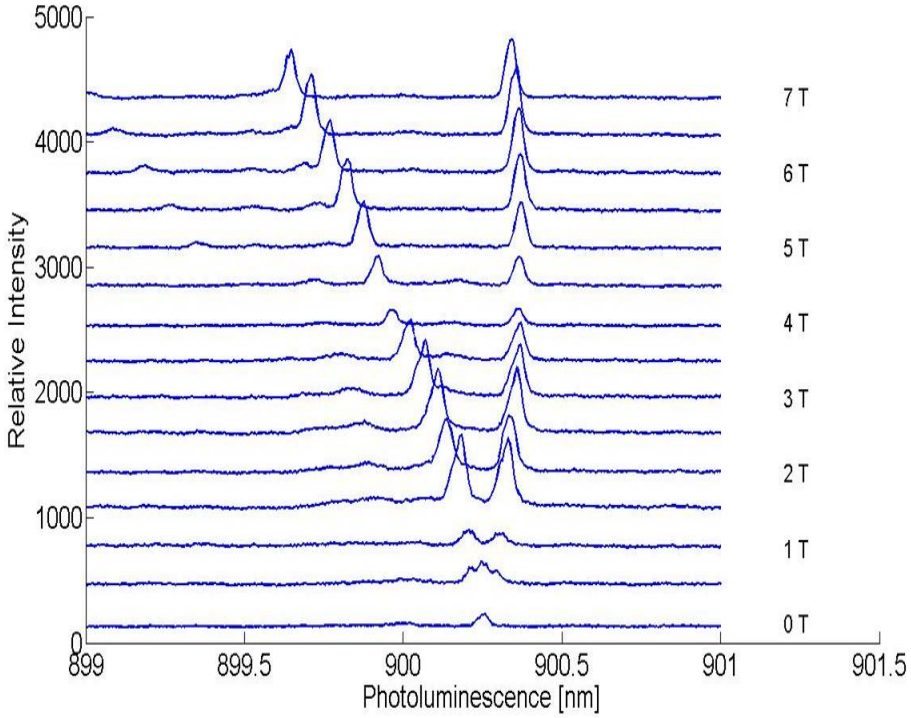

Figure 7.1: This data shows typical spectra from a single quantum do as a function of magnetic field. The data are taken from 0 to 7T every 0.5T. The spectra clearly curve towards shorter wavelengths which is due to the diamagnetic shift.

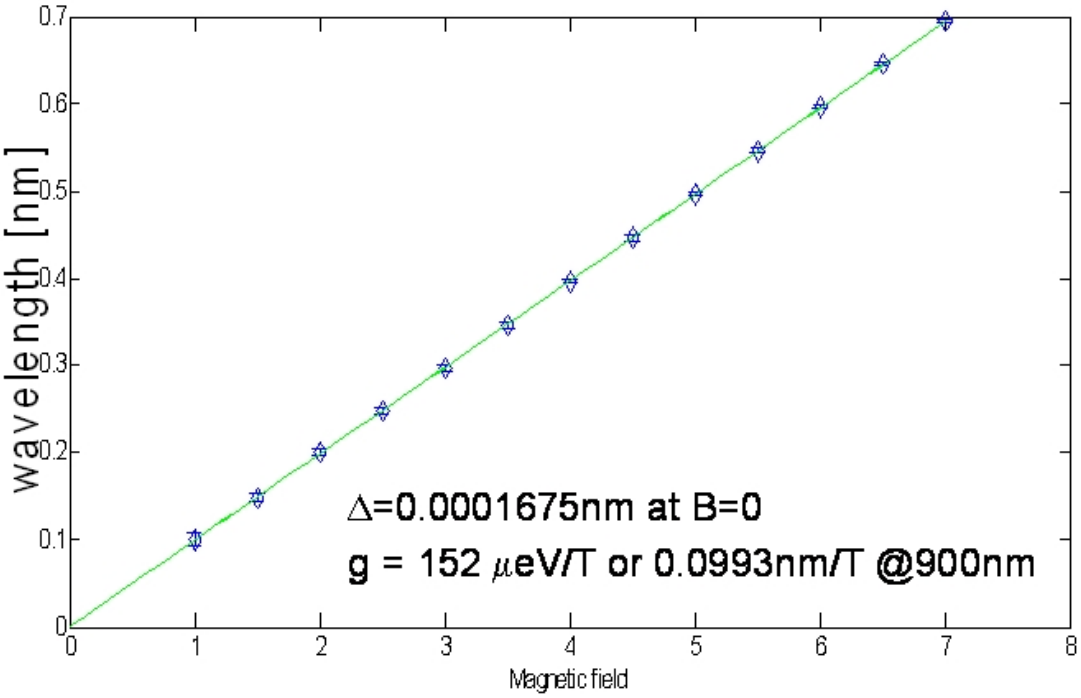

Figure 7.2: This plot shows the splitting from the data in Fig. [**?**]. The data lie on a staight line and have a g_{eff}-factor of 152 μeV/T. This corresponds to a g-factor of -2.62

determine the total g-factor for the dot. In fact the magnetic field for an observed Zeeman energy splitting Δ_{ZE} is related to the applied field by

$$\begin{aligned} \Delta_{ZE} &= |E_{|+1\rangle} - E_{|-1\rangle}| && (7.1) \\ &= \sqrt{\delta_1^2 + \beta_1^2} && (7.2) \\ &\approx \mu_B(g_{e,z} + g_{h,z})B_z && (7.3) \end{aligned}$$

If we desire to use the dot as a local probe of the magnetic field we must know the g-factor prior to calculating the magnetic field. Thus if we want to measure the field created by a local ferromagnet we can vary the external field and assume that the field due to the ferromagnet is unchanged. This is a reasonable assumption

for fields where the ferromagnet has reach saturation and for Dy this was true for B>1T as shown in Sec. 5.4.6. Simply put, we have two unknowns–the g-factor and the magnetic field due to the nearby ferromagnet– and we can use an experimental parameter and a measured variable from which we can determine both unknowns. This can be summarized by the following equation:

$$\Delta_{ZE} = \mu_B(g_{e,z} + g_{h,z})\,[B_0 + B_M] \tag{7.4}$$

where B_0 is the external magnetic field and B_M is the magnetic field due to a localized magnetic material. Thus, if we measure splitting values while B_M is saturated and fit the data to a line we can determine how much contribution to the splitting is due to B_M. This can be done by extrapolating the line to when $\Delta_{ZE} = 0$ at which point $B_M = -B_0$. This is the basis for the measurements we made to try to determine the effect of the Dy ferromagnets located near the quantum dots as described below.

7.2 g-factor variation

Before we discuss the details of the measurements of the quantum dots near nano or micro-magnets let me point out the variation in g-factors which we could do after accumulating many spectra. The data are composed from two sets: 1) From spectra where we actually swept the magnetic field and then found the slope of the fitted line and 2) data from which we divided the observed splitting by the applied external magnetic field. From these data we created a histogram of the distribution of g-factors as shown in Figure 7.3.

7.3 Diamagnetic Shift

Diamagnetic shifts from single quantum dots have been reported [82, 83, 84]. Typical coefficients are less than 20 μeV/T^2. This means that the central position of the two peaks blue-shifts quadratically for increasing magnetic fields. As can be seen from the spectra plot in Fig. 7.1 the peaks indeed curve towards higher energy. INSERT

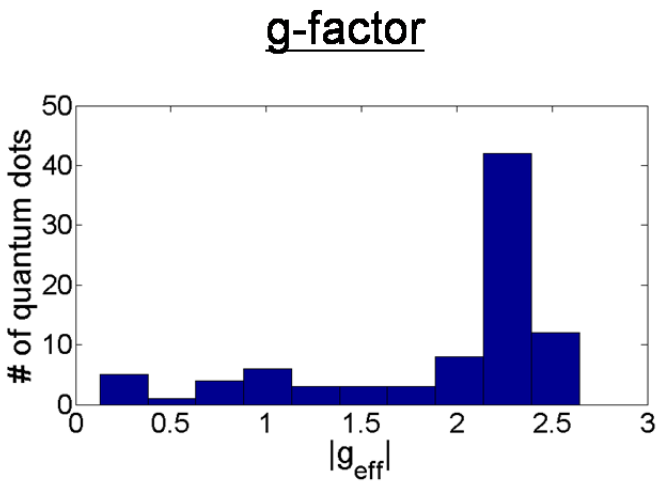

Figure 7.3: A histogram of the distribution of g-factors for the dots we have measured. This data can only tell us the effective g-factor, or $g_{e,z} + g_{h,z}$. If the dark states could be measured then it would be possible to determine the contribution from the electron and hole separately. The best way to do this is to apply the magnetic field slightly off a normal axis and this introduces a mixing of the bright and dark states.

FIGURE.

7.4 Voigt Geometry

We also explored Voigt geometry photoluminescence studies for two reasons: 1) For determining the effect of the Dy magnets in a different orientation and 2) For creating entangled photons from a quantum dot [5] by tuning the magnetic field to a point where two of the energy levels in the Voigt geometry are nearly degenerate 2.4.2.

7.5 Quantum dots with magnets

This section shows devices I fabricated that include mesas containing quantum dots and nearby magnetic material. The clean room processing for this work ultimately

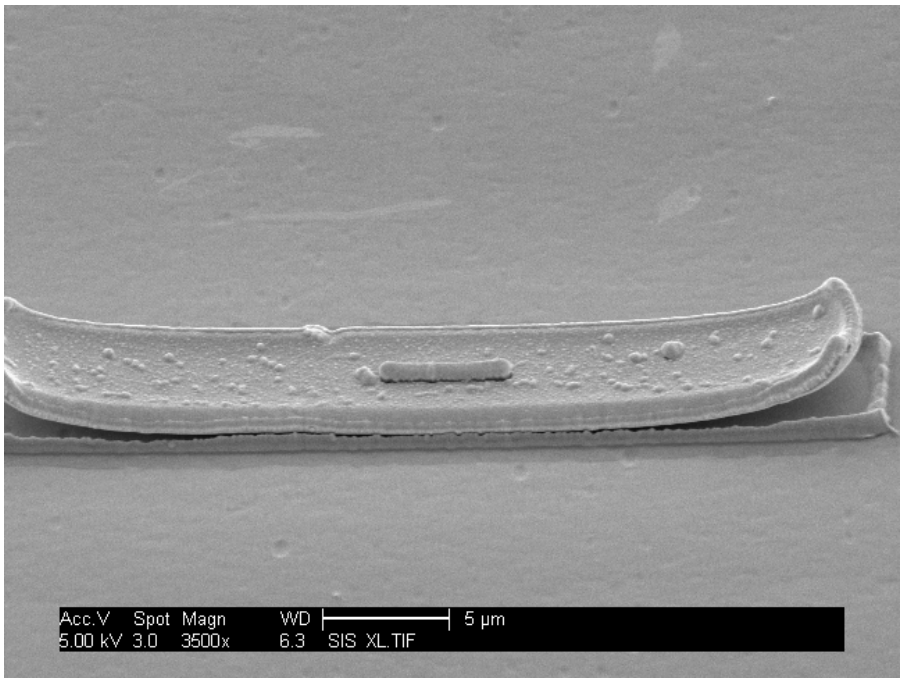

Figure 7.4: This SEM shows a full view of a magnetic that capped a mesa containing quantum dots. The dysprosium metal deposited was 1μm thick and tremendous strain developed in this film causing it to curl. Also noticeable is what we believe is a dynamical shadow-masking effect. This is evident in the region of metal deposited around the edge. We believe that the magnet curled up while deposition was underway and after curling it acted as a mask for further material that was deposited directly onto the substrate.

helped us determine a structure that was easier to fabricate and also, in principle, could achieve larger magnetic field gradients.

7.5.1 Faraday orientation

We first tested devices that included mesas embedded inside the magnetic material. This was done by orienting the magnetic field parallel to the growth direction. We simulated the results as show below and also mesaured devices that had this configuration.

Magnet Simulation

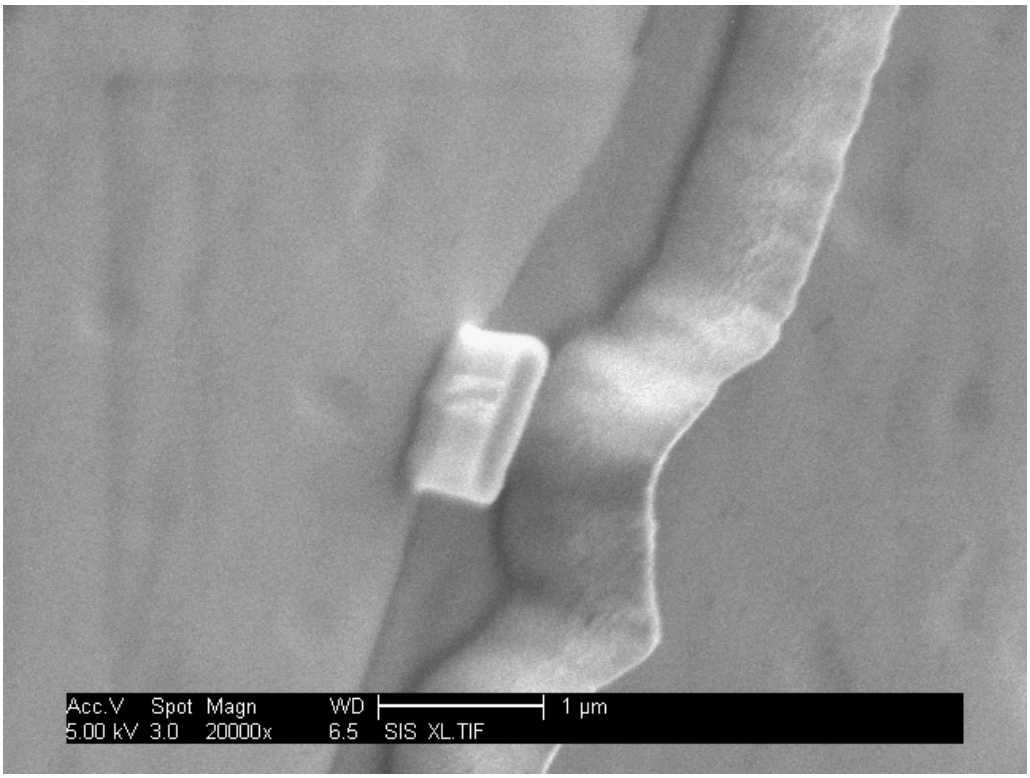

Figure 7.5: The original intent of the experiment was to place micromagnetic material near to mesas containing quantum dots. This SEM shows a triangular magnetic structure we fabricated near the mesa. The mesa is the oval- shaped region and the triangular magnet is pointing toward the mesa.

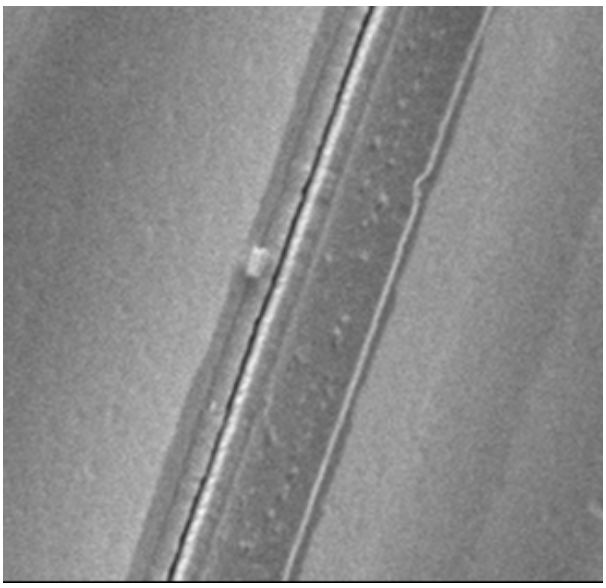

Figure 7.6: The original intent of the experiment was to place micromagnetic material near to mesas containing quantum dots. This SEM shows a rectangular magnetic structure we fabricated near the mesa, which is the small mesa that appears whitish in the SEM micrograph.

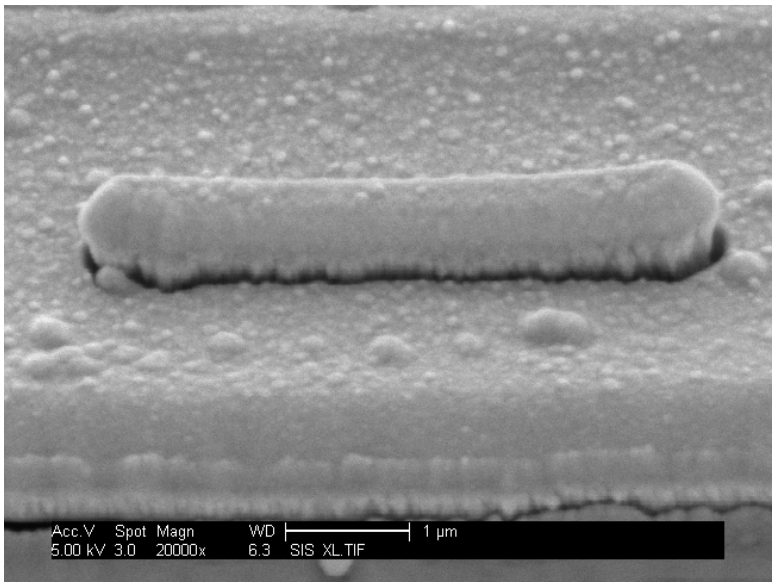

Figure 7.7: The SEM shows a magnet with a region protruding out due to the mesa below. The mesa was roughly 0.5μm tall and with the magnet deposited on the mesa and surrounding region

Experimental Result

7.5.2 Voigt orientation

To confirm that the dysprosium magnet was indeed the source of the offset we decided to rotate the such that the magnetic field was perpendicular to the growth direction. In this orientation we expected a

Magnet Simulation

Experimental Result

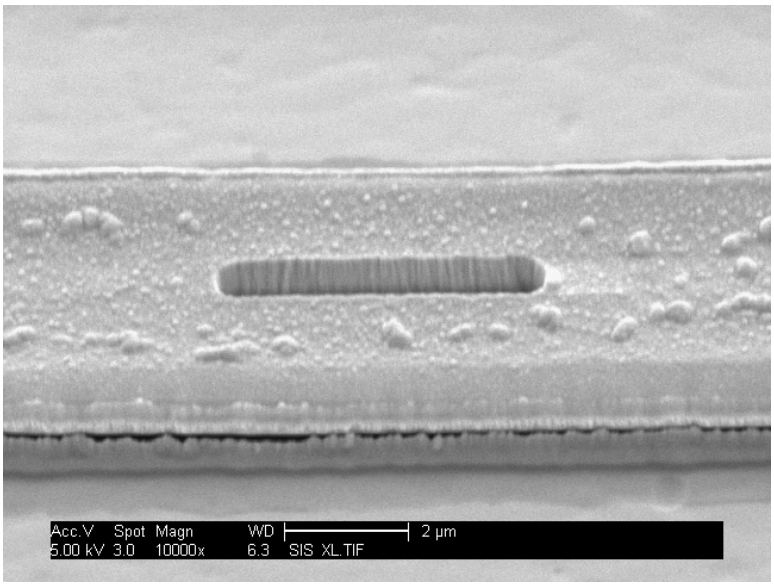

Figure 7.8: This SEM shows the metal directly above the mesa was removed. This effect is due to a dynamical shadowmasking effect which cause the region above the mesa to form a mushroom-like cap. When we performed lift-off this small region of material was removed. This was not universal and roughly 50% of the structures had caps removed. With the cap removed it was possible to perform photoluminescence studies.

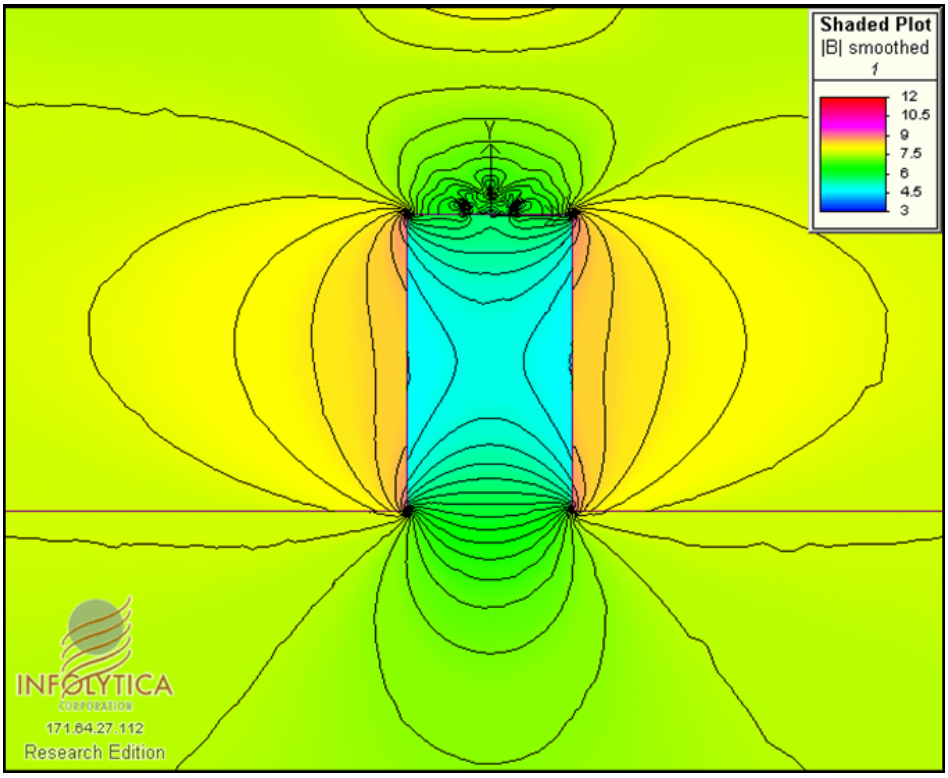

Figure 7.9: This simulation is for the Faraday geometry. Notice that the magnetic field is decreased inside the void region. The blue region is missing magnetic material while the surrounding yellow region contains dysprosium.

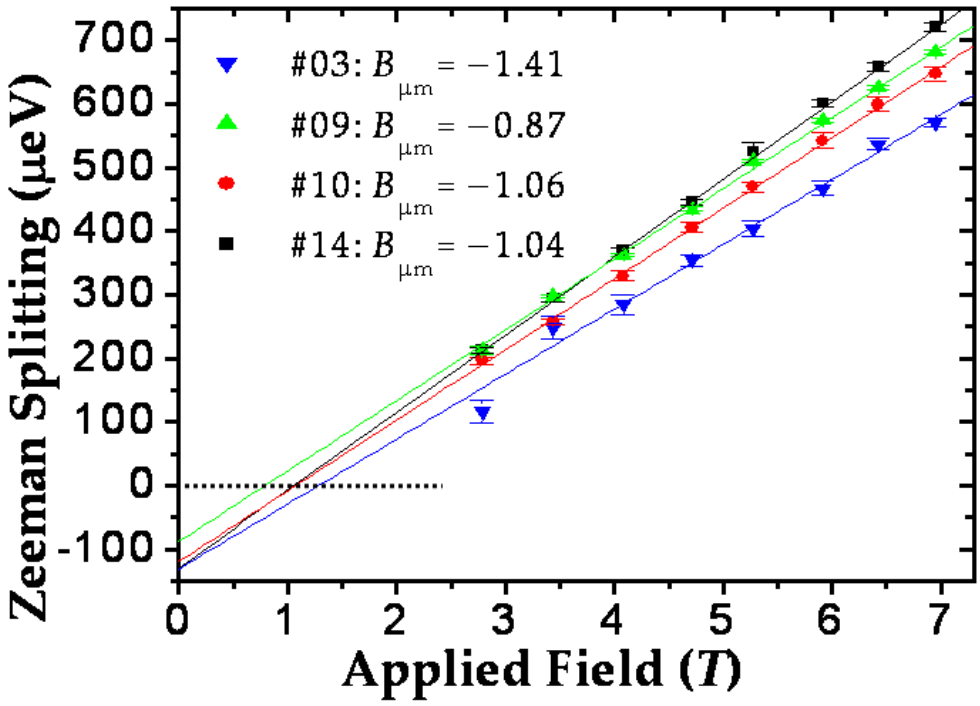
#03: $B_{\mu m} = -1.41$
#09: $B_{\mu m} = -0.87$
#10: $B_{\mu m} = -1.06$
#14: $B_{\mu m} = -1.04$
Zeeman Splitting (μeV)
Applied Field (T)
700
600
500
400
300
200
100
0
-100
0
1
2
3
4
5
6
7

Figure 7.10:

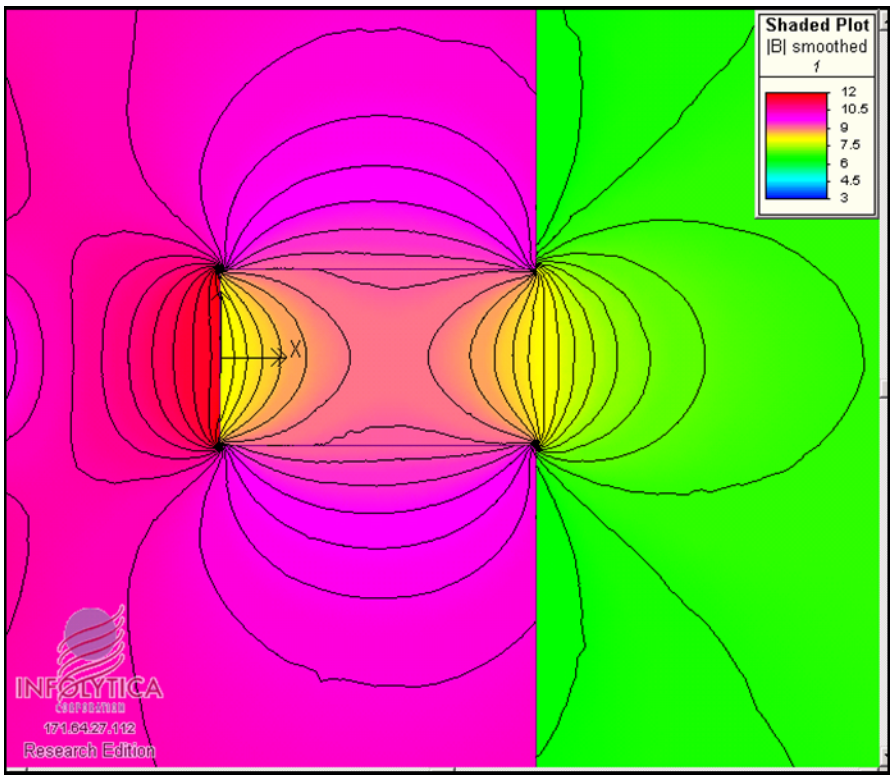

Figure 7.11: Simulation showing Voigt Simulation

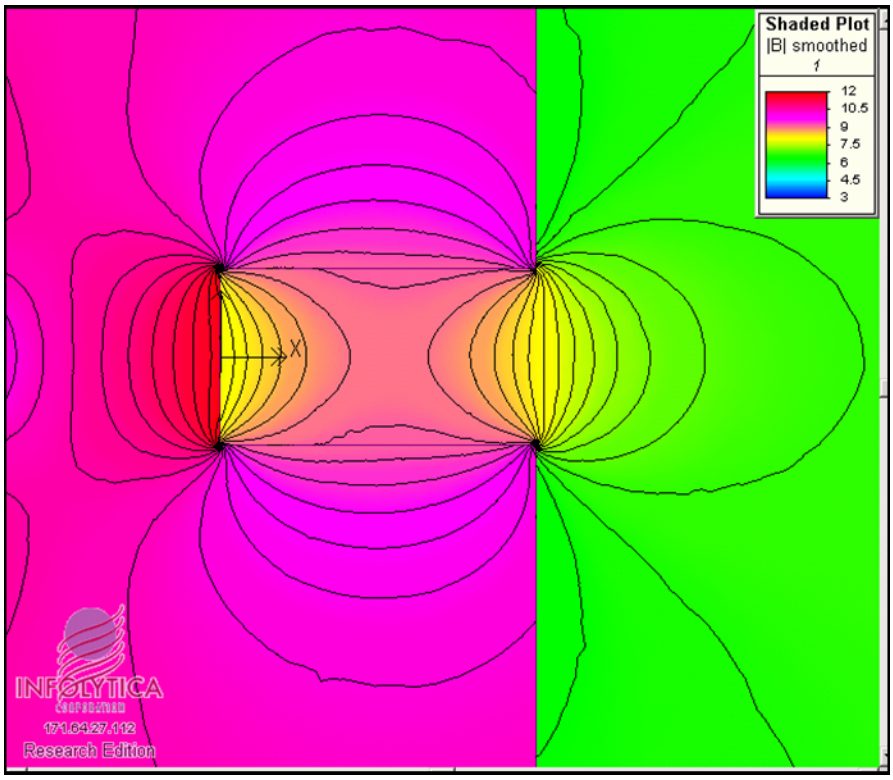

Figure 7.12: Simulation showing Voigt geometry. Notice that hear the void has an increase in the magnetic field strength instead. This simulated result was confirmed by our experiments.

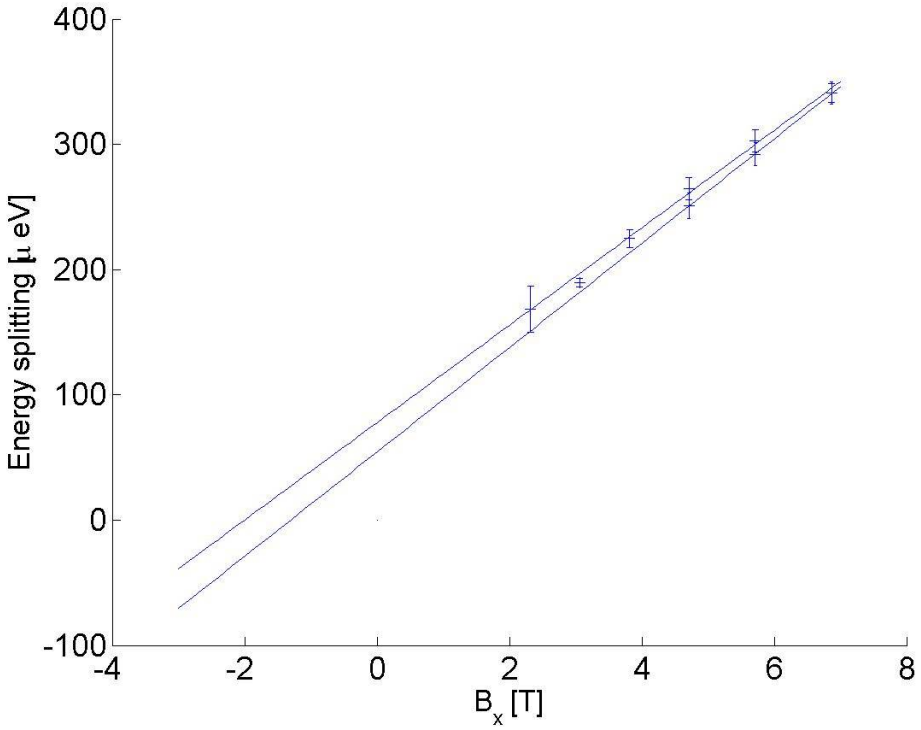

Figure 7.13: Here we observed that indeed the magnetic field produced by the void in the Voigt gemoetry was additive. This can be seen by finding the x-intercept of the lines drawn. At this point the observed Δ would be 0 and thus $B_{\mu m} = B_0$ and so we can extrapolate what $B_{\mu m}$ assuming that it does not change with external magnetic field, B_0.

7.6 Blinking and Spectral Stability

The emission spectra from quantum dots sometimes changed significantly from second to second or between different days. Generally, we tried to avoid working with dots which exhibited poor stability in their emission spectra. However, we found that sometimes things just changed for unexplained reasons. For one dot we studied the emission spectra remained stable for a few weeks and then after removing the sample to room temperature, remounting the sample and then reloading it into the VTI, the emission changed. In fact for mesa 1175, the emission spectra we show in Sec. 8.4 disappeared. This change may be due to strain from the way the sample is mounted.

Sometimes the change seemed to be correlated to pumping with high laser power over an extended period of time. This is highly speculative and not something we devoted effort in trying to quantify but a trend that we noticed. For one dot (mesa 1191), the emission spectra disappeared entirely when pumping in the wetting layer ($\sim$850nm) but after pumping using a red diode laser ($\sim$650nm) the emission returned to "normal" behavior. This may be indicative of some localized charge instability. Further evidence of this behavior was observed at the end of one day in a dot who subsequently never regained the spectrum we had first observed when we began to work with it. In fact, we took 5 second acquisitions every 5 seconds over the course of a few minutes and the result is plotted in Fig. 7.14. We interpret the jumping of the spectra as due to emission from different charge states. The emission could be due to a change in the local Coulombic environment or from different charge states of the quantum itself. The main point is that some further study could be pursued to understand this behavior and it may that this behavior could be utilized in some controllable way. Maybe a combination of charge states and change in local strain can allow one to tune the emission spectra of a quantum dot in a arbitrary way. This could be of practical importance to cavity QED experiments where mode matching between the cavity and the quantum dot remains a challenge.

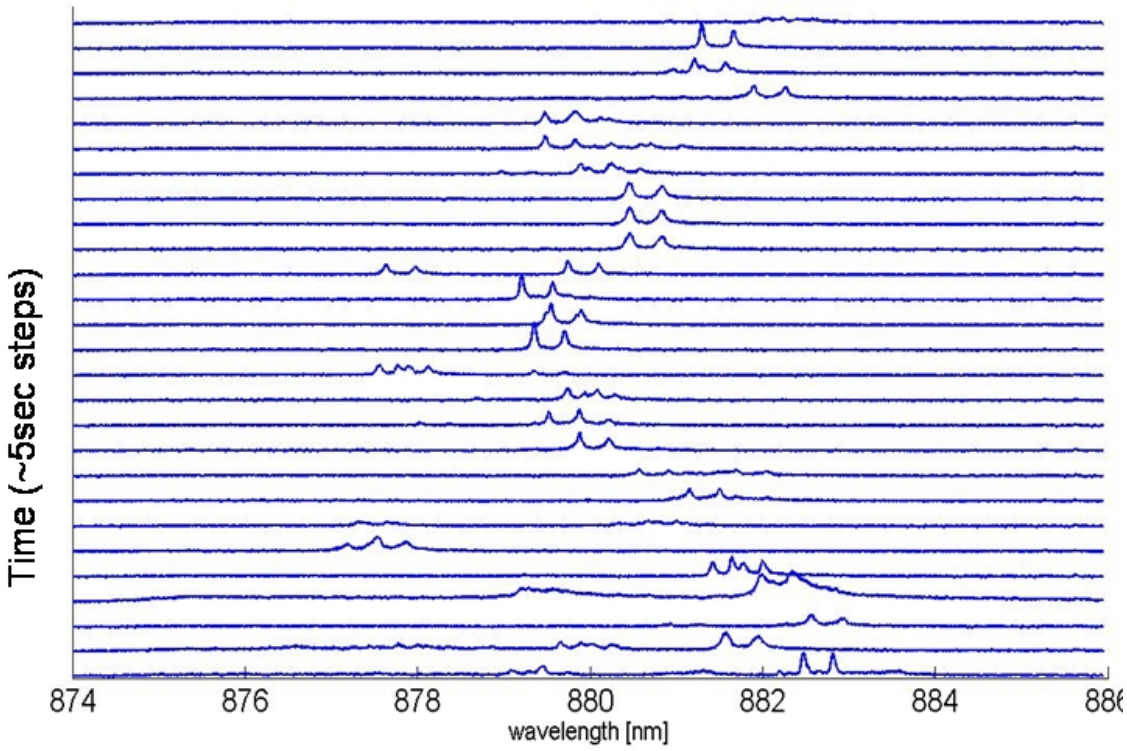

Figure 7.14: These spectra are from a dot who we noticed had an unstable emission spectra. The spectra shown are 5 second acquisitions taken roughly every 5 seconds. The emission appears to be hoping around. It appears that the emission is mostly stable for a few seconds and then jumps but over a 5 second interval it doesn't jump much. In that case we would see many more doublets in each acquisition.

Chapter 8

Optical Pumping Measurements

This chapter presents the results of the optical pumping experiments and compares these results to the theory developed in Sec. 3. These experiments require control of the pump laser polarization as well as shutters to control the timing of the pump polarization and the collected photoluminescence. The setup for this timing control is shown in Sec. 5.4.6 and details for the particular timings for each experiment is shown below with the experimental result. The data in this chapter present a novel way of probing the nuclear spin dynamics within a quantum dot. Previous work has used a depolarizing rf field to study the timescale of nuclear depolarization in the presence of rf [85], but this work is the first to study the timescale over which Overhauser shifts develop by observing the photoluminescence evolution.

8.1 Measurements

The primary objective of the experimental efforts presented in this section was to demonstrate that with a quantum dot it is possible to couple the nuclear spins and the electron forming the quantum dot exciton. In order to achieve this goal, we first set about trying to control the incident polarization of the pump light.

8.1.1 Typical Results

A typical spectra while pumping the quantum dots via wetting layer excitation under different pump polarizations is shown in Fig. 8.1. In these data the laser wavelength was set to 854.2nm and the pump power was measured at 2.1mW before a glass wedge which reflects 5% of the light. The data in the figure below is the result of the photoluminescence under two pump conditions. In one case the pump polarization was σ_+while in the other it was σ_-. The photoluminescence under these two pumping conditions leads to different Zeeman splitting values. For the result plotted in Fig. 8.1 the Zeeman splitting under $\sigma_+$is 0.0440nm $\pm$ 0.0021nm and for σ_- it is 0.0773nm $\pm$ 0.0015nm. The difference, $\Delta = |\Delta_{\sigma_+} - \Delta_{\sigma_-}|$, in this case is 0.0333nm $\pm$ 0.0026nm.

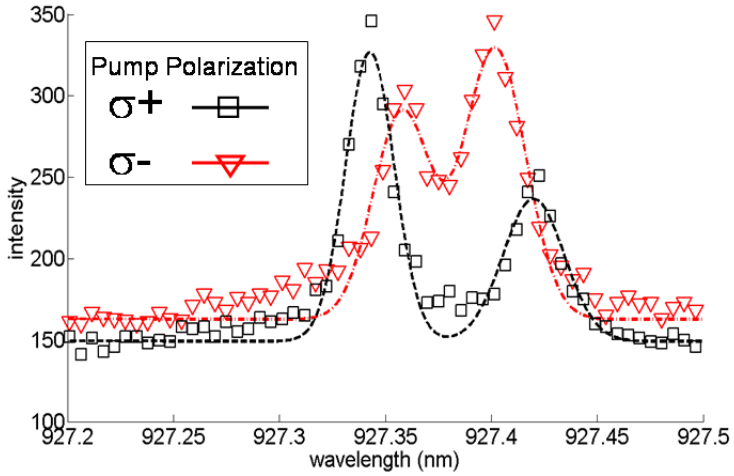

Figure 8.1: A typical PL spectrum under $\sigma_+$and σ_-pump polarization. These data was taken at 0.8 T.

The basic approach we take is to collect the data and apply a Gaussian curvefit to the spectra. From this fit we can extract the center positions $\lambda_0^{\sigma+}$ and $\lambda_0^{\sigma-}$, the widths $\Gamma^{\sigma+}$ and $\Gamma^{\sigma-}$, and the peak heights $I_0^{\sigma+}$ and $I_0^{\sigma-}$. We can also extract a confidence interval for each of these parameters. The confidence interval is the 95% likelihood bounds of a particular value for the fit. This bound is converted to an error bar. Then,

we repeat this experiment multiple times in order to improve the uncertainty of the center position of the curve-fit. One point is that we calculate Δ for a given Zeeman-split pair and then do the statistical analysis by comparing Δ between different runs. This approach helps us avoid difficulties arising from Coulombic shifts of the center position of the peaks or from temperature changes which give rise to different peak positions. However, the splitting is only affected by magnetic fields and is therefore insensitive to temperature fluctuations or different Coulombic environments. Discuss g-factor dependence. Discuss charge states.

8.1.2 Expected Shift

This section discusses the expected spectrum for different pump polarization assuming a model where the dark exciton state is involved in the nuclear polarization process. As presented in Chapter 3, the dark exciton state is populated due to a fast hole relaxation time. It is not known if the hole spin relaxes in the wetting layer or within the dot but either case leads to the same conclusion regarding the effect on the nuclear polarization.

The argument for what type of spectrum we expect to see is presented in the captions for Figures 8.2 and 8.3. Essentially, the g-factor is expected to be negative and we see spectra that typically look like that shown in Figure 8.2. In fact the spectrum shown in Figure 8.1 has the same asymmetry in the peak intensity and the direction of the peak movement is similar. This result is encouraging in that the peak movement is consistent with a shift due to nuclear polarization. However, the fact that the shift is consistent with a model that invokes a hyperfine interaction does not preclude the possibility that some other effect is at work. For instance could unpaired electrons in the wetting layer or bound to impurities be responsible for the Zeeman effect? This unknown prompted us to try both nuclear magnetic resonance and also timescale measurements. Nuclear magnetic resonance would manifest itself in a change of the Zeeman splitting and would prove that nuclei were responsible. It turned out that this approach would not work and the reasons are discussed in Section 8.3.2. Instead a timescale longer than μseconds would be a likely indicator

that nuclei were at play. In addition, we performed some measurement using timescale measurements that demonstrate a long lifetime for the shift which is indicative of nuclear polarization.

8.1.3 Power Dependence of observed shift

One of the first measurements we tried after observing the Overhauser shift was to explore the power dependence of this shift. That is, we can plot Δ versus laser pump power. The experimental result for one particular dot is shown in Fig. 8.5.

A model that might explain this data is one that assumes a simple picture of two states with transition rates between the two. By state I do not mean a quantum-mechanical state but a description of the status of the magnetic field creator. One extreme is the state of thermal-equilibrium, P_0 while the other extreme is the steady-state nuclear polarization, P_{ss}, achieved under a given laser power and applied external magnetic field, B_0. Let us label the transition rate from P_0 to P_{ss} to be a, and let b in the downward transition from P_{ss} to P_0 as shown in Fig. 8.6.

We can write the rate equations for this system as,

$$\begin{aligned} \dot{P_{ss}} &= aP_0 - bP_{ss} \\ \dot{P_0} &= -aP_0 + bP_{ss} \end{aligned}$$

We can simplify the picture further by noting that since the net polarization is normalized to 1, $P_{ss} + P_0 = 1$. Once we solve for the steady state, P_{ss}, we arrive at

$$P_{ss} = P_{max}\frac{a}{a+b}$$

Here, b is the relaxation rate which is independent of laser pump power, while a is directly proportional to pump power. These assumptions are reasonable although the actual physical system could be more complex that this model. Nonetheless, this behavior is consistent with the observed result as shown in the model. We can extract some fitted parameters for these numbers and here we find that $P_{max} = 0.097$nm and $b = 1.468$.

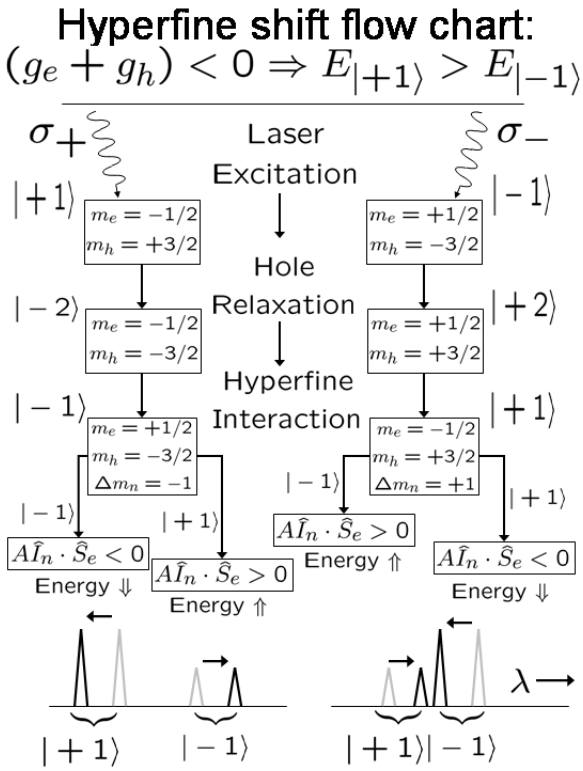

Figure 8.2: This flow-chart shows the effect of the nuclear spins on the emitted photon energy for g_{eff} <0. If excitons are created in the wetting layer under σ_+illumination predominantly $|+1\rangle$ excitons are created. Thus the grey peaks shown have a large intensity for the $|+1\rangle$ state which is at larger energy or shorter wavelength. Hole spins can easily flip which leads to dark exciton population build-up in the wetting layer. Alternatively, the hole-spin can flip even while the dot is populated by a bright exciton state. In any event once the hole relaxes, there is a possibility for the nuclear spin and electron spin to exchange spin direction via a hyperfine process as discussed in Chapter 3. In the case of σ_+pumping the nuclei tend to become negatively polarized after repeated spin flips. Then if a $|+1\rangle$ is present in the dot the nuclei that are spin-down and the electron that is spin down lead to a net positive hyperfine interaction. This means that the higher energy peak blue-shifts. Alternatively, if a $|-1\rangle$ exciton is trapped in the dot the hyperfine interaction is negative and thus it red-shifts. In summary the peaks become further separated under σ_+illumination. We can go through a similar analysis for pumping under σ_-polarization which leads to a compression of the peaks. Also note the longer wavelength peak, associated with the $|-1\rangle$ exciton state is dominant in this case.

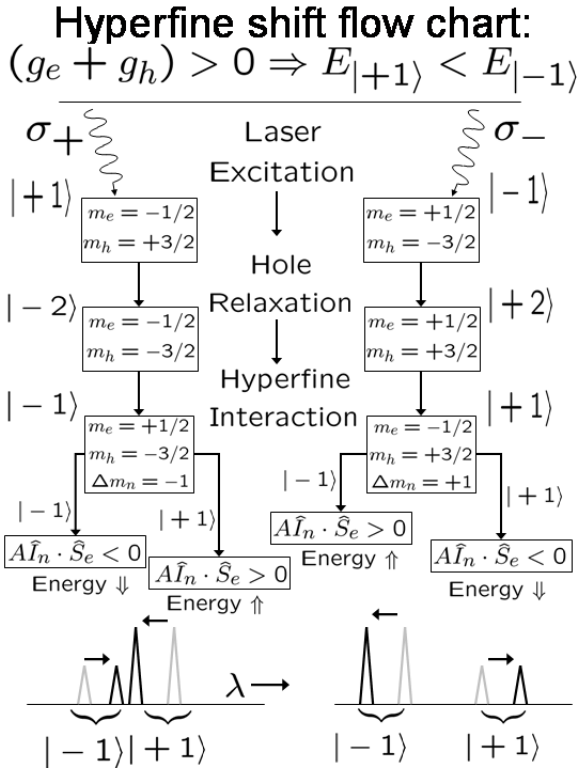

Figure 8.3: For the case of $g < 0$ similar spectra are observed but instead the peaks compress for σ_+pumping. Also note that now longer wavelength peak (smaller energy) peaks is more prevalent due to the lower probability of electron spin-flipping events. Thus, the peaks shift and the dominant peak is the higher energy peak to the right. For the case of σ_-pumping the peaks move further apart and the shorter wavelength peak (higher energy) has a greater intensity. Thus, the spectrum are completely reversed.

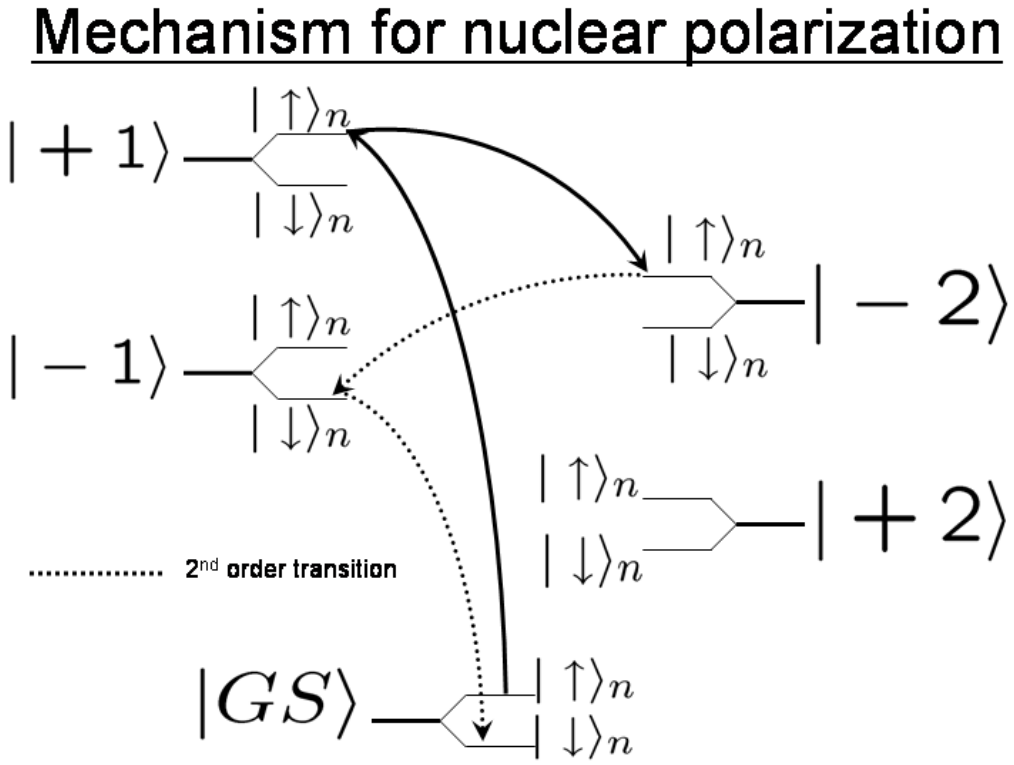

Figure 8.4: This diagram provides an pictorial model for the nuclear polarization under σ_+pumping. The bright state is populated in the dot and then the hole spin relaxes which causes the exciton the relax to the $|-2\rangle$ state. A flip-flop processe occurs which causes the electron and nucleus to exchange spin directions and this leads to a change in the nuclear spin direction to be in the downward direction. The process of the electron-spin flip and simultaneous nuclear-spin flip does not conserve energy and so the process is virtual and called a spin-flip assisted radiative recombination. To conserve energy the emitted photon will have an increase or decrease in its energy corresponding to the energy mismatch between the $|-2\rangle$ and the $|-1\rangle$ state. The

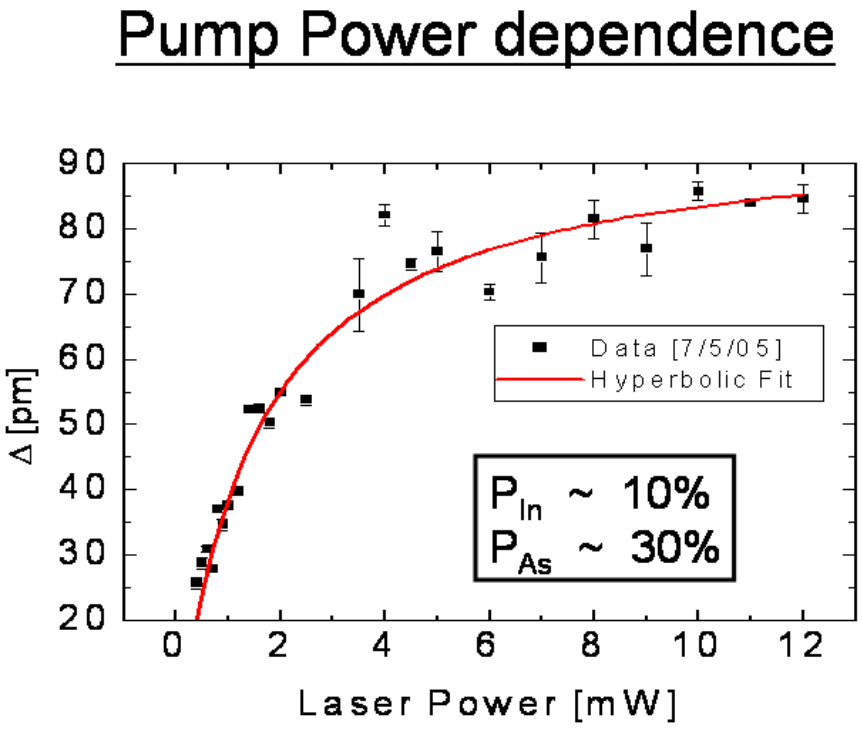

Figure 8.5: Power dependence of Δ. Typically, we would run the experiment at laser powers of 1-3mW, which is below the saturated region. At higher laser power the emission from the quantum dot becomes more broadband and biexciton peaks begin to appear and eventually dwarf the single exciton peak. At large pump powers the total shift Δ approaches 0.09nm, which can be converted to a nuclear polarization of 10% for indium and 30% for arsenic.

8.1.4 Resonant Excitation

Most of the work presented in this thesis involved pumping excitons into the wetting layer (850-860nm) and observing the photoluminescence (870-940nm) from single quantum dots. It should be noted, however, that we can excite resonantly or in an excited-state of the quantum dot. Spectroscopy where one varies the excitation laser wavelengths is called photoluminescence excitation spectroscopy. This is interesting because by scanning the laser pump wavelength we can change from creating excitons within the wetting layer to creating excitons in the n=2 or other higher excited

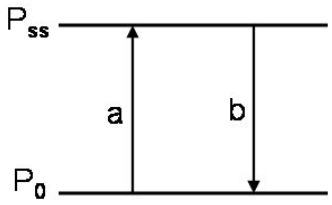

Figure 8.6: A two-state model for the system. P_{ss} is the steady-state polarization and P_0 is the thermal equilibrium polarization.

state of the dot itself. This offers less chance for the electron spin to flip. In fact the typical n=2 excited state for the dot is located 10-20 meV from the ground state recombination energy. Once an exciton is injected directly into this state there are fewer opportunities for the electron spin to flip so the emitted PL should have better spin conservation or more asymmetry in the peak height. Indeed, one mesa (1189) shows an increase in spin conservation. This experiment was challenging and we only studied a few dots using PLE. This line of research is more challenging since the resonance are often very narrow (0.1-0.5nm) and can easily be missed during a scan. In addition, the resonance can change due to nuclear polarization build-up and changes in the local charge configuration. Here I show two figures with spectra from the same dot under different pumping conditions.

8.2 Time-scale measurements

Using shutters to control the timing of the excitation laser and the photoluminescence collection we can gain access to dynamical behavior of the quantum dot emission. There are a number of variations of experiments but the basic principle is to observe the dynamic response of the photoluminescence.

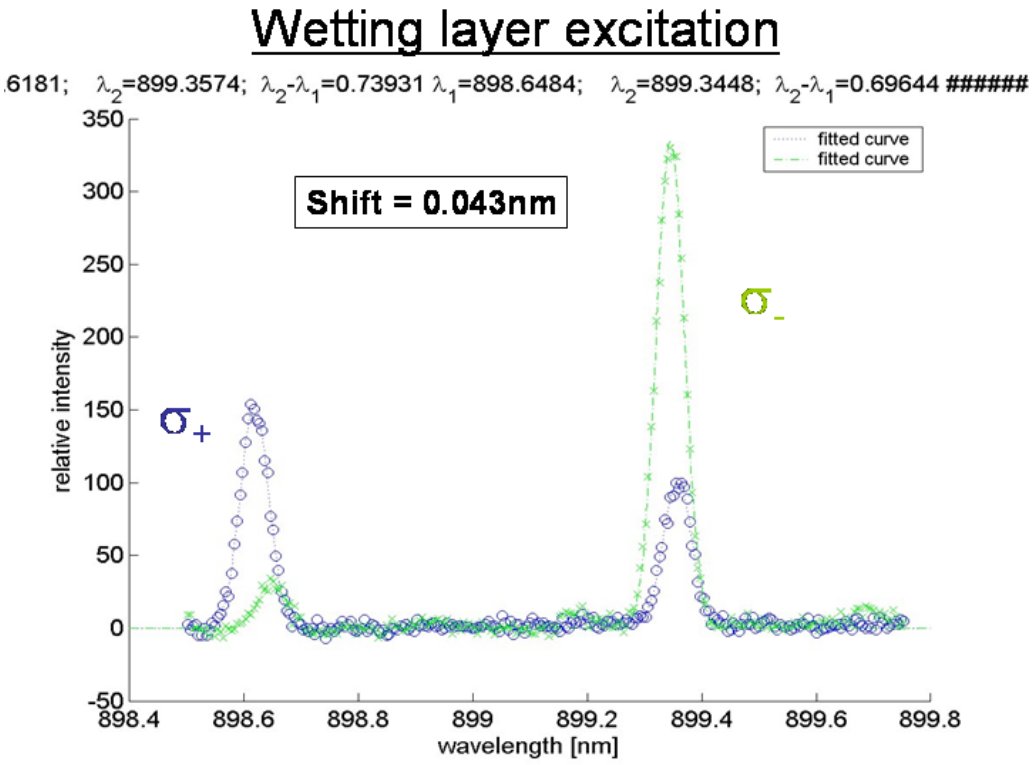

Figure 8.7: These data were taken under wetting layer excitation (852nm). NOtice that the longer wavelength (lower energy) peak is dominant under σ_-pumping. Under $\sigma_+$the higher energy peak is more dominant but the asymmetry in the peak heights is quite pronounced. Comare this to Figure 8.8

8.2.1 Polarization Timescale Measurement I

After observing the shift and power dependence we tried to determine the timescale over which the shift develops. The shift arises from observing the photoluminescence under different pump polarizations so if we excite the quantum dot with σ_+ and σ_- alternately and varied the period, f, of the square-wave that controlled the pump laser polarization we could measure the timescale over which the shift develops. The schematic shown in Fig. 8.9 shows how the pump alternated between the two polarizations, σ_+ and σ_-. Then, we collect the photoluminescence under only one polarization with the timing diagram shown in Fig. 8.10. We collect photons over many cycles in

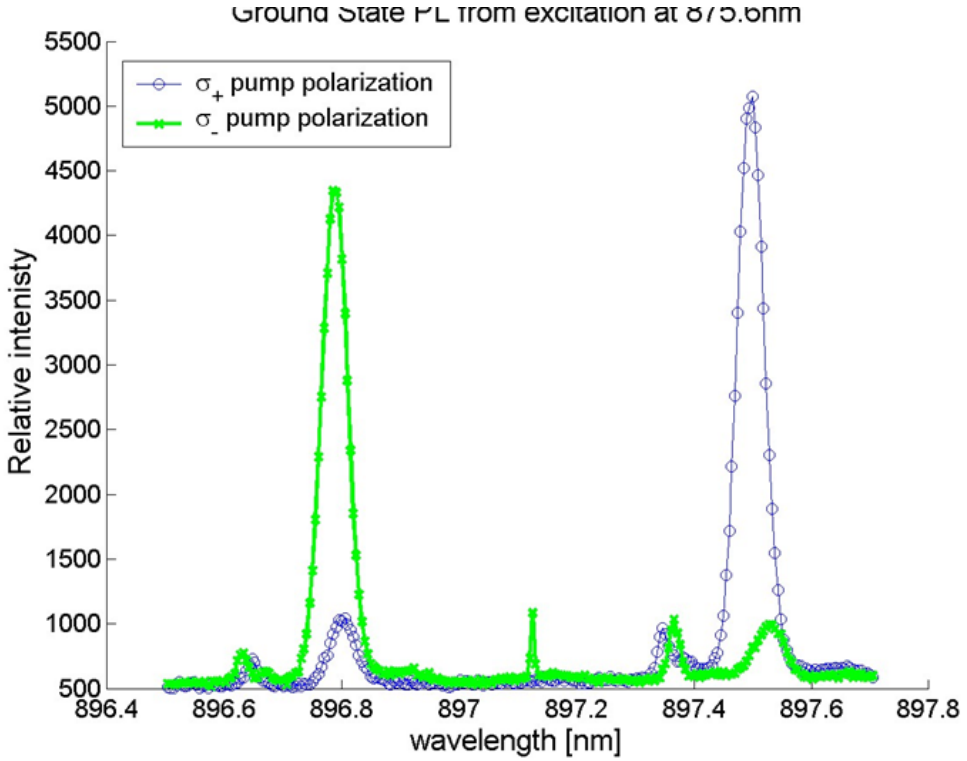

Figure 8.8: These data were taken from the same dot shown in Figure 8.7 but instead the dot was pumped with the laser tuned to 875.6nm. Notice now that the peak asymmetry is more symmetric. That is, when the laser is set to σ_+mostly σ_+light is emitted and vice-versa and this "spin-conservation" exists relatively equally for both pump polarizations.

order to collect a sufficient number of photons that can be detected by the nitrogen-cooled CCD attached to our monochrometer as described in Sec. 5.4.3. The observed Zeeman-split pair has a splitting which I will label, Δ_{σ_+}. We repeat this experiment under the same conditions but collect photons during the time that the laser polarization is set to σ_- as shown in Fig. 8.11. Thus we perform two experiments where we obtain two Zeeman splittings of Δ_{σ_+} and Δ_{σ_-}. Then for each given frequency f, we can calculate the difference between these two polarization, $\Delta = |\Delta_{\sigma_+} - \Delta_{\sigma_-}|$. We performed this experiment 10 times for each polarization and for each value of f. The results for one particular dot are shown in Fig. 8.12. I have included an exponential

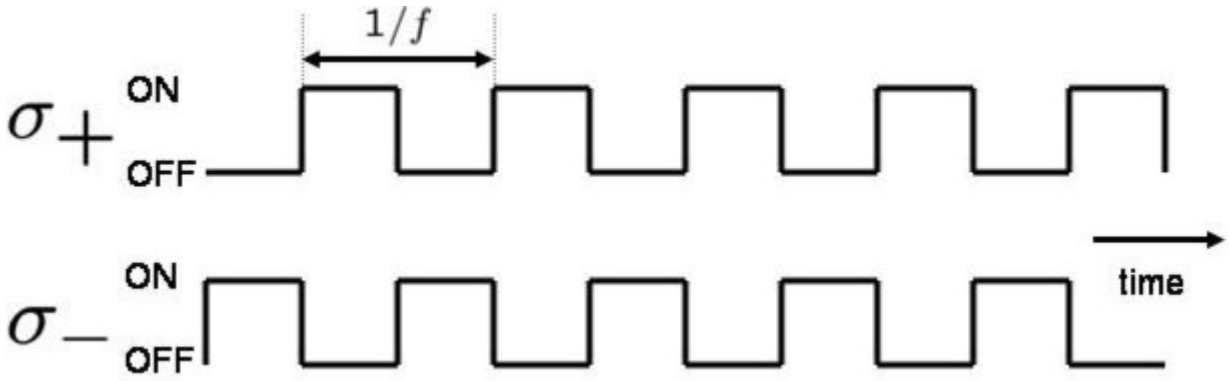

Figure 8.9: Timing Diagram for laser pump polarization

decay, $P_0 e^{-t/\tau}$, fit on the graph and obtain a decay of 77 ms. We have also seen this behavior in more than one dot. In fact we have seen it in different mesas and in multiple dots. In Figure 8.13 we show the data taken from a number of dots and include the associated decay times for each of them.

The first experiment we tried was to change the pump polarization alternately between σ_+ and σ_-. We collected the photoluminescence from only one polarization. At the extreme where the alternation between the two pump polarization prevented any nuclear spin polarization to develop we would expect no difference between the photoluminescence under σ_+ or σ_- pumping.

8.2.2 Polarization Timescale vs. Laser Pump Power

Data showing how the timescale measurement varied with increasing the laser pump power is shown in Fig. 8.14.

8.2.3 Polarization Timescale vs. External Magnetic Field

Data showing how the timescale measurement varied with increasing the external magnetic field is shown in Fig.8.15.

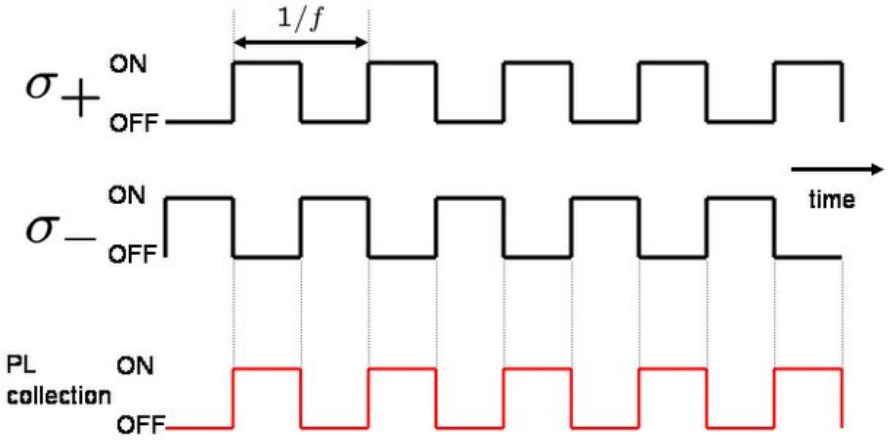

Figure 8.10: Timing diagram to collect σ_+ photoluminescence. The shutters controlling the laser path that creates σ_+ is synchronized with shutter controlling the PL collected.

8.2.4 Polarization Timescale Measurement II

The next variation on the timescale measurement we devised was a means to try to extract the timescales for each pump polarization. That is, what is the timescale to reach $P_{ss}^{\sigma+}$ and $P_{ss}^{\sigma-}$? It turns out that the timescales are not identical and there is a theoretical basis that supports this.

The idea is to momentarily probe the Zeeman splitting of the quantum dot emission without disturbing the polarization of the system. This may be possible with a weak laser field probe or equivalently observing the photoluminescence for a short window. The schematic, shown in Fig. 8.18, shows the timing diagram for the experiment. We chose a value for f to be sufficiently small that we were in a regime where Δ was maximized for that particular pump power, or in other words, we could assume that the system reached $P_{ss}^{\sigma+}$ or $P_{ss}^{\sigma-}$. At the same time we wanted to collect as many photons as possible so the larger f we selected the more photons we collected. According to the results from "Polarization Timescale Measurement I" Section we find that $f = 1$ Hz provides sufficient pumping time (500ms) to reach either $P_{ss}^{\sigma+}$ or $P_{ss}^{\sigma-}$. We probed the Zeeman splitting at a variable time, τ with σ_-probe light

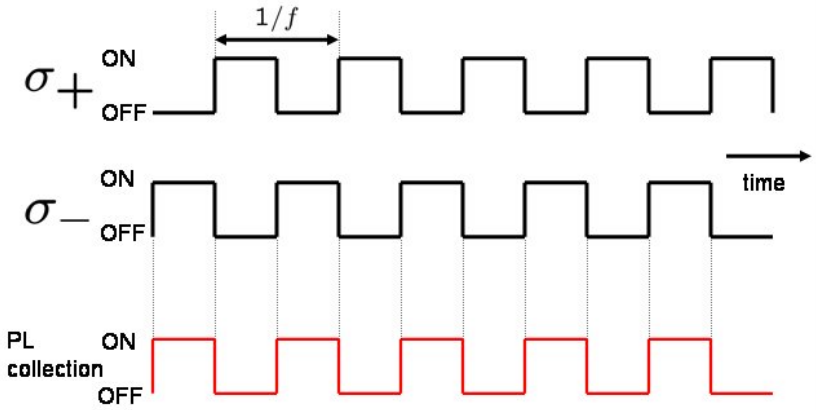

Figure 8.11: Timing diagram to collect σ_-photoluminescence. The shutters controlling the laser path that creates $\sigma_-$is synchronized to with shutter controlling the PL collected.

after having achieved $P_{ss}^{\sigma_+}$. We obtained results for the peak positions as shown in Fig. 8.19. Notice that the relative peak heights switch and as τ increase the peak shift together in the case of $\sigma_+$and apart for σ_-.

The plots in Figures 8.20 and 8.21 show the change in the Zeeman splitting versus delay τ.

8.2.5 Relaxation/Diffusion Timescale

Another variation of the timescale measurement we tried was to pump with σ_-until steady-state was reached. Then, we turn off the laser and wait a time, τ_w during which the nuclear spins might diffuse or relax to thermal equilibrium. As in the Polarization Timescale Measurement II, the probe had to be weak and the timing precise. The timing diagram is shown in Fig 8.23.

The result we observed was that the shift was always present even for the case where $T_w = 20$s. In Fig. 8.24 we show the raw data for $T_w = (0.1s, 5s, 10s, 20s)$. This experiment shows that the shift does not disappear while the laser is off even after 20 seconds. The longevity of the survival of the shift suggests that whatever leads to

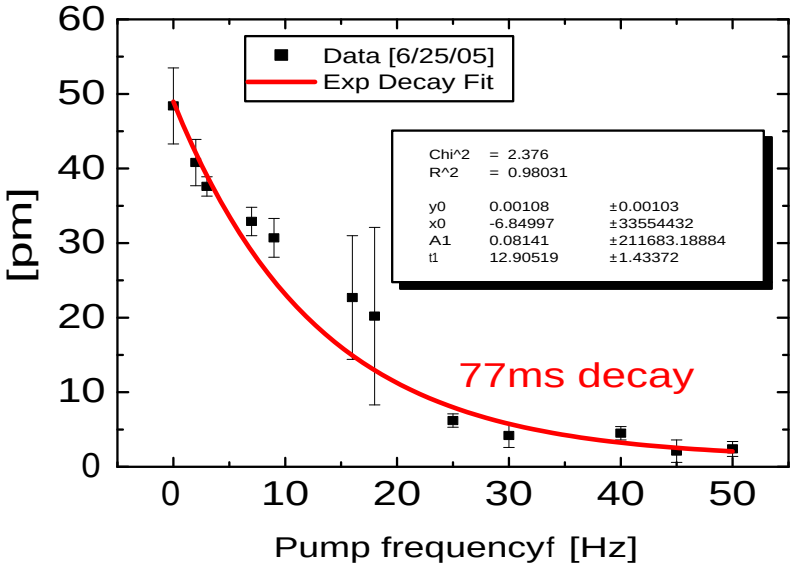

Figure 8.12: Plot of Δ vs. laser pump frequency f for dot located in mesa#1175

the shift has a long lifetime and the most likely candidate for such a long lifetime are nuclei.

8.3 Nuclear magnetic Resonance

In order to couple directly to the nuclear spin we can use radio frequency waves which can induce nuclear spin state transitions. In order to broadcast the rf an antenna, or coil, was placed near the the sample. We connected this coil to a transmission line which in turn was connected to our frequency generator and amplifier. Let me give a brief introduction to operational principle of nuclear magnetic resonance.

8.3.1 Past NMR efforts

Now that we have established a strong case that the mechanism is indeed due to nuclear spin, the obvious experiment to try is to remove the effect of the nuclear

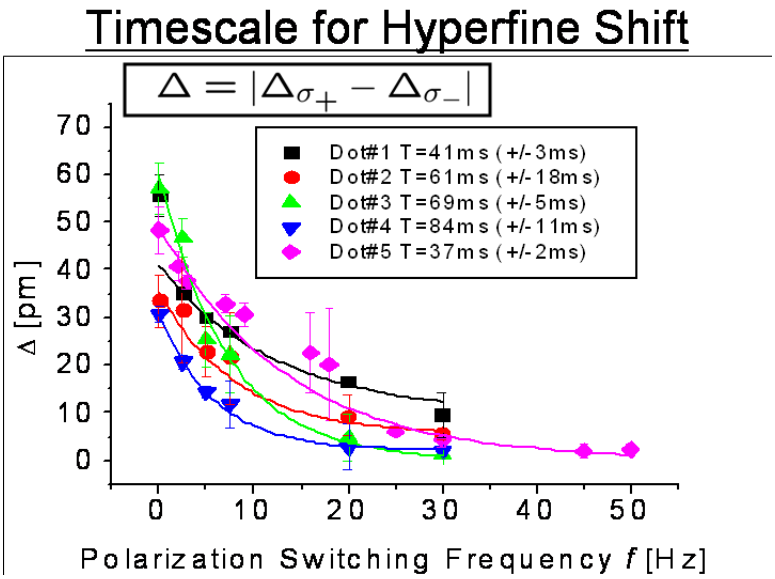

Figure 8.13: Plot of Δ vs. laser pump frequency f for multiple dots.

spins by using nuclear magnetic resonance as discussed in Sec. 3.6. We hoped that by using pulsed or cw NMR we could interact directly with the nuclei and observe an effect on the photoluminescence.

We have tried multiple methods including both pulsed and FM continuous wave rf. This was attempted in the old apparatus as well as the new one in 25D with different coils and different materials (aluminum and macor) to hold the sample. We also have introduced a chopper on the laser pump side in order ensure that for some period of each second there are no excitons present in the dot or in the wetting layer. We in fact have varied this chopper frequency from around 100 Hz down to 1 Hz. Another variable we have attempted to explore is the rf power. We have increased the power as high as we can with our existing apparatus. At the largest powers we have operated we start to introduce so much power that we can detect that the variable temperature insert (VTI) begins to warm by about 0.5 K using the VTI temperature sensor and fluctuates in time, which makes the system very unstable for doing measurements that require integrations greater than 5 seconds– which are the majority of the useful experiments. In addition the spectrum red-shifts

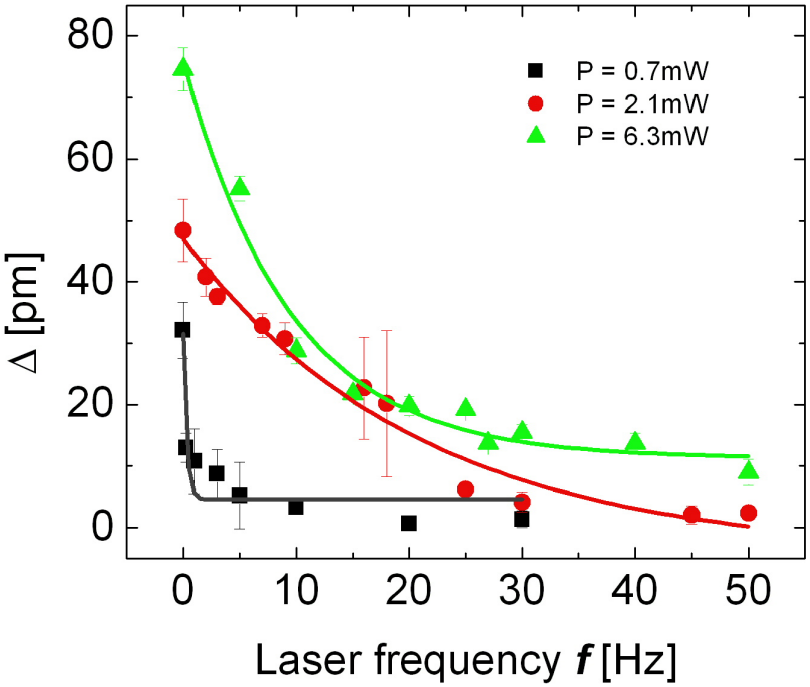

Figure 8.14: Plot of the dependence of the polarization timescale for different pump power condition

and becomes weaker which suggests that the true temperature at the sample is larger than measured by the VTI temperature sensor.

Recently, we tried an experiment using FM rf of the form $\omega(t) = \Omega \sin(\omega_c t) + \omega_0$. Here, Ω is the frequency excursion, ω_0 is the carrier frequency, and ω_c is the sweep rate of the frequency modulated rf. We tried to look only during the phase of the FM waveform so that we only collect photoluminescence when the nuclei are aligned to the external magnetic field or when they are anti-aligned. However, we could not observe any effect.

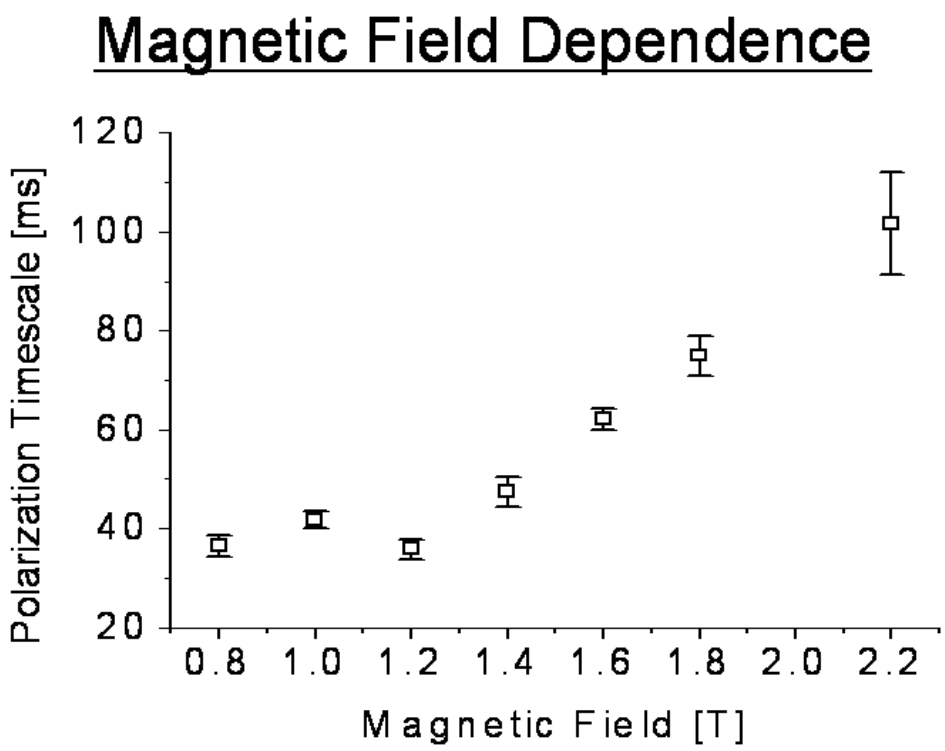

Figure 8.15: Plot of the dependence of the polarization timescale for different external magnetic field values. The laser pump power was kept constant for these measurements

8.3.2 Problems with RF

Given that the rf has not been successful and we have tried in one form or other during one year to get it to work there could be something intrinsic to the InAs quantum dot which will make NMR challenging. Some of the unknown parameters include:

- NMR linewidth γ: Gammon's result showed a resonance of 20 kHz for Ga and 20 kHz for As. He also reported that the linewidth of some dots was broadened by even up to a factor of 10. Typical bulk NMR results also suggest a dipolar broadening of the order 10's of kHz. This could lead to a further broadening beyond the typical solid-state nuclear dipolar broadening. In contrast the result by Gammon et al was taken with the laser on and maybe the 20 kHz

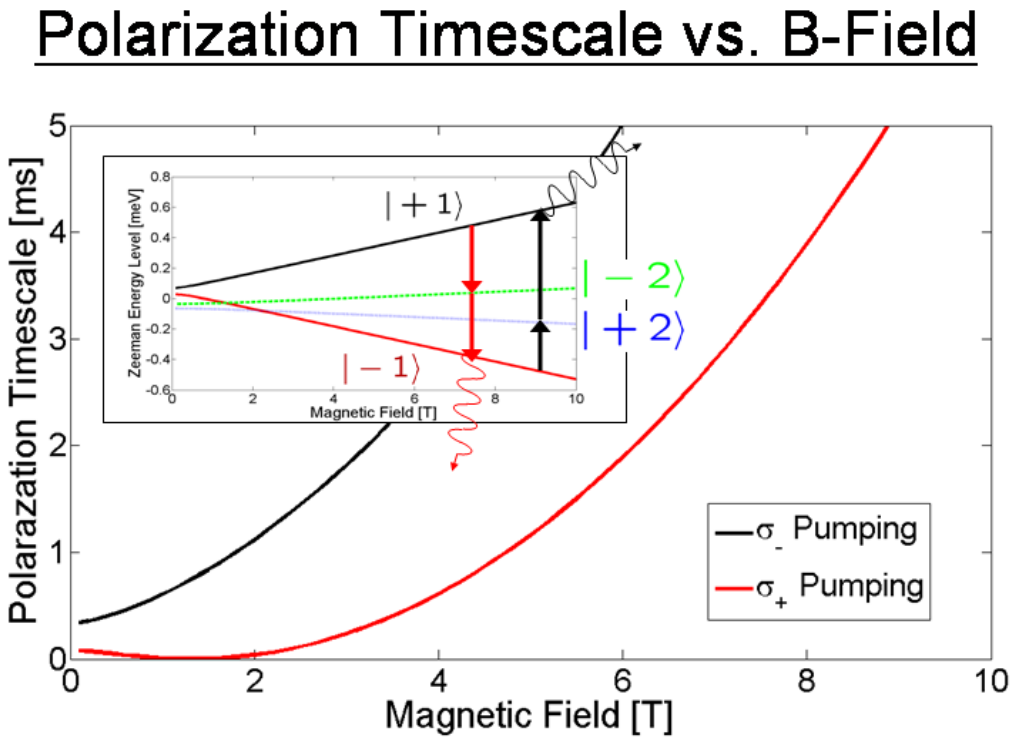

Figure 8.16: Plot of the theoretical polarization timescale for different external magnetic field values. The laser pump power was kept constant for this model. An important point to note is that σ_+pumping always polarizes the nuclei faster than $\sigma_-$and this can be explained from the difference in the energy mismatch between the dark state and the bright state involved in the second-order recombination. The insert shows the energy dependence of the exciton states versus magnetic field

broadened line was due primarily to a fluctuating magnetic field created by the exciton trapped in the dot. This makes choosing an appropriate value for the frequency excursion Ω or the pulse widths in pulsed NMR difficult.[ADD SECTION ABOUT STRAIN].

- Exact magnetic field, B_0. The exact field at the quantum dot could be off due to some local paramagnetic impurities in the sample could alter the field. Again, Gammon reported that the resonance frequency varied from dot to dot. An impurity could also lead to a broadening of the line. If the resonance frequency

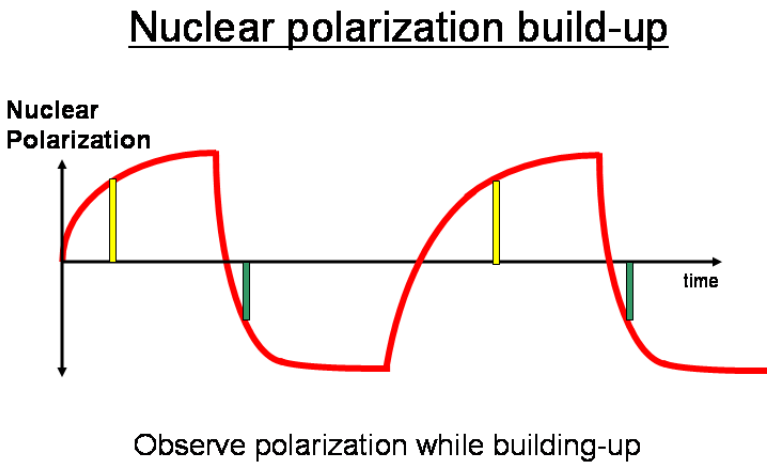

Figure 8.17: Snapshot of shift as it develops

is not precisely known as well as the linewidth it makes the parameter search challenging.

- rf power, B_1: The power created by the coil and seen by the nuclei in the quantum dot is unknown. Since this is non-conventional NMR and we have no direct *emf* to detect, it is difficult to calibrate pulses and estimate the power the nuclei are experiencing.

The overall point of this section is to list known possible reasons why the rf is not working. I would also like to point out that when I met Dan Gammon at the APS meeting this year he said that the last time he tried using rf to interact with the nuclear spins within their quantum dots they could not reproduce their earlier result and they did not have an explanation for their lack of success. This suggests to me that getting the rf operational is not a routine task as it is in conventional NMR where there is a well-established technique.

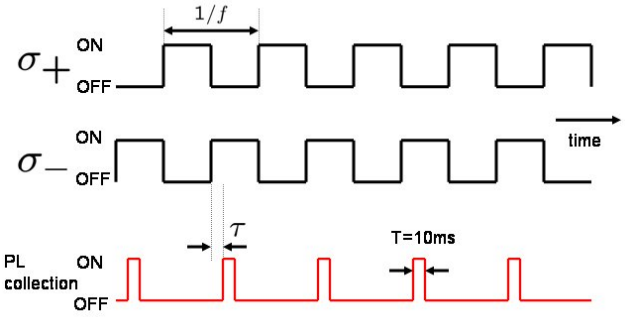

Figure 8.18: This is the timing diagram for Polarization Timescale Measurement II. We either collect after the start of the σ_+laser pulse or the σ_-laser pulse.

8.4 Trion States

. In Section 8.1.2 we explained how the data shown in Section 8.1.1 can be explained. We found additional dots that had different behavior in terms of the relative peak heights. An apparent Overhauser shift was still present but instead when we pumped with σ_+

8.4.1 Nuclear Polarization

Santori reported that a given can alternate between being a negative trion, positive trion, neutral, and a bi-exciton mode among possibly other multi-particle complexes. Thus, a dot could achieve nuclear polarization through the means discussed in Chapter 3 and when we probe the dot while it is in a charge state we would still see the effect of the nuclear spins on the emission wavelength of the photoluminescence.

8.4.2 Summary of Timescale Behavior

The shift we have observed is most likely due to nuclear spin because:

1. The timescale is of the order of milliseconds to tens of milliseconds.

- This timescale is extremely long to be due to electron spins in the wetting layer reservoir. The exciton lifetime in the wetting layer is on the order of picoseconds. This result is based on Santori's result [3] with the streak camera where he observed that the photoluminescence from the wetting layer disappears within 25 picoseconds. Thus, the spin direction of the electrons in the wetting layer follows the optical field polarization with a lag of < 25ps.
- If the effect is due to some charge trap state then we would expect a sudden shift in the photoluminesence energy. Instead, we observe a gradual change in the peak positions as shown in the section titled Polarization Timescale Measurement II.
- Another possibility is the build-up of electrons trapped on the surface of the mesa. However, we have been working with 1 micron x 1 micron mesas and the dipolar field from electrons at this distance is very weak.

2. We have observed a similar timescale in multiple dots. We can conclude, then, that the mechanism causing this behavior is intrinsic to the material and not a random unexplained local charge state in one particular dot. For the effect to be universal would require that the mechanism be do something like the electron reservoir, but as discussed in the above point, this timescale is much faster than the observed timescale of milliseconds.

3. The shift remains even after the laser field is removed for 20 seconds. This suggests that the mechanism leading to the shift is long-lived. Nuclear spin polarization is known to be long-lived in solid crystals at low temperatures.

These results are interesting because this is the first reported measurement for the nuclear polarization timescale in single self-assembled InAs quantum dots. Previous work measured the depolarization rate of nuclei (namely Ga and As) in GaAs quantum dots under cw rf of 3.5sec but no one has directly observed the nuclear polarization timescale within a single quantum dot. Additionally, we have reported about the

charged quantum dot and nuclear polarization within it. This type of dot holds tremendous interest for the community for its use in quantum information devices.

One can think about the nuclear polarization with a back-of-the-envelope approach as well. Assuming that roughly 10^9 excitons can be captured in the dot per second then in theory there could be 10^9 spin exchange between nuclei and electrons per second. The dot is now quite saturated so the number of excitons injected into the dot is actually lower and the probability of a spin flip-flop process is much less than 1. Also, there are 10^4 to 10^5 nuclei within the dot. Roughly speaking with a 10% nuclear polarization there are between 10^3 and 10^4 nuclear m_I sublevels that advance during the polarization process. Roughly then the probability of the flip-flop process needs to be about 10^{-5} to 10^{-4} in order to polarize the nuclei to 10%. These numbers are thus reasonable.

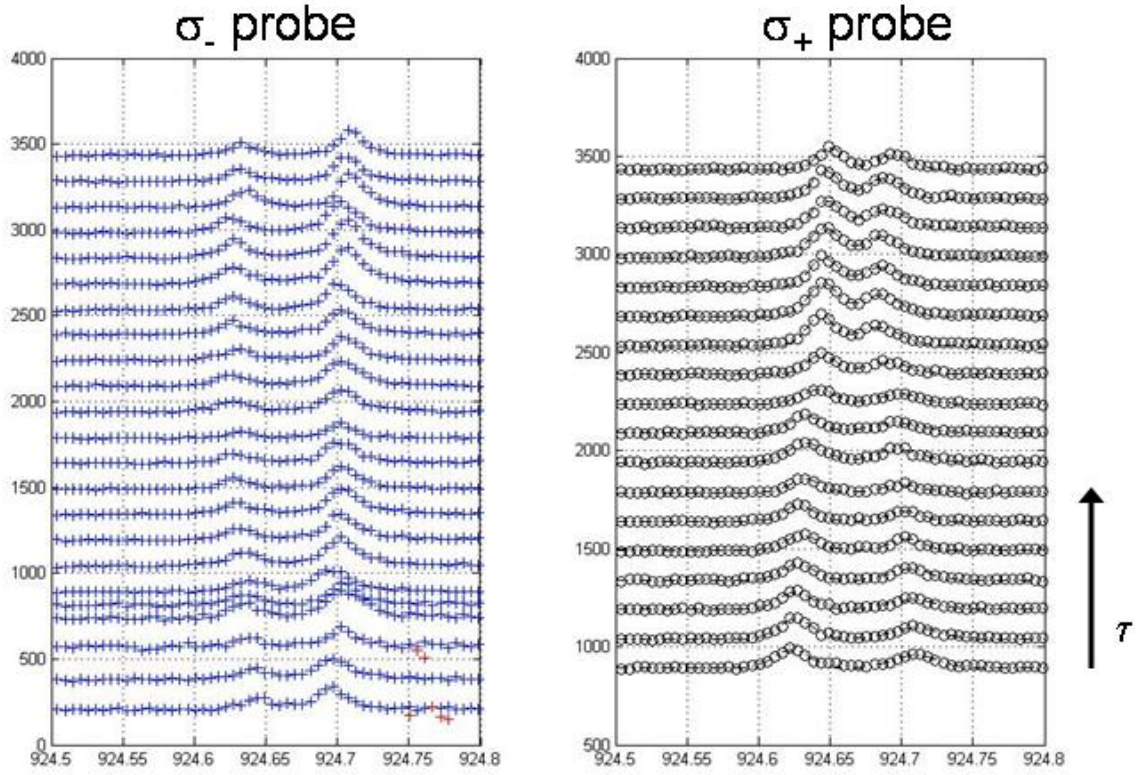

Figure 8.19: A plot showing the peak evolution of the peaks under different pump polarization

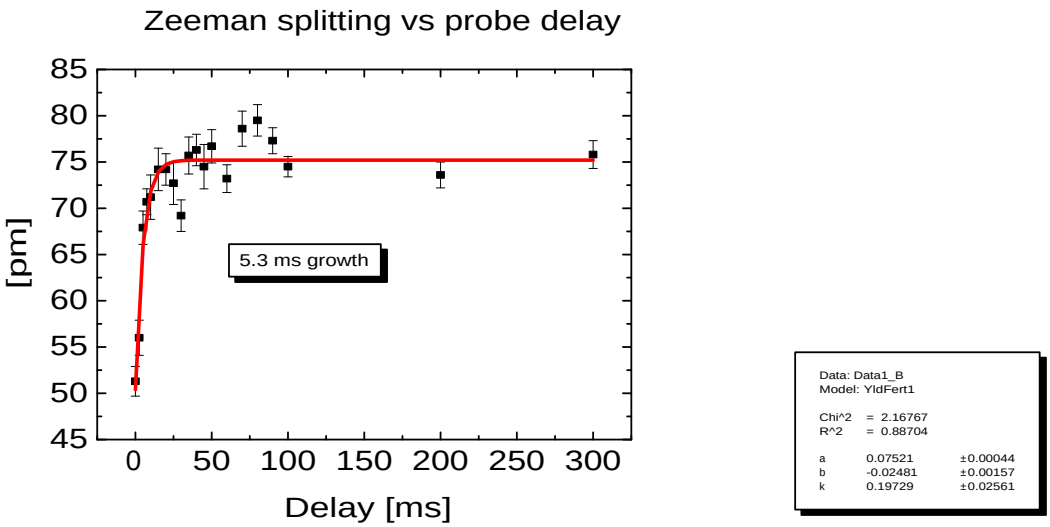

Figure 8.20: A plot of Δ_{σ_+} vs. delay τ.

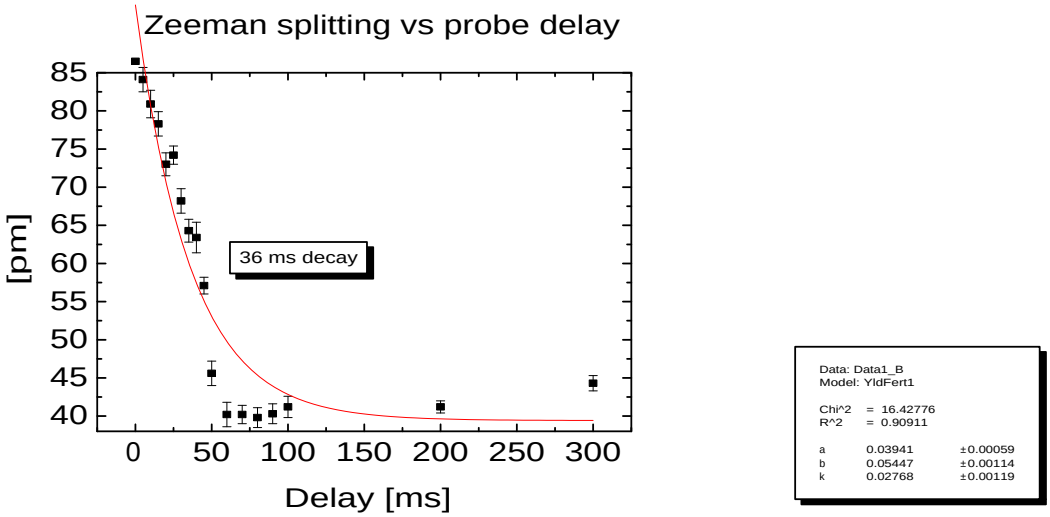

Figure 8.21: A plot of Δ_{σ_-} vs. delay τ.

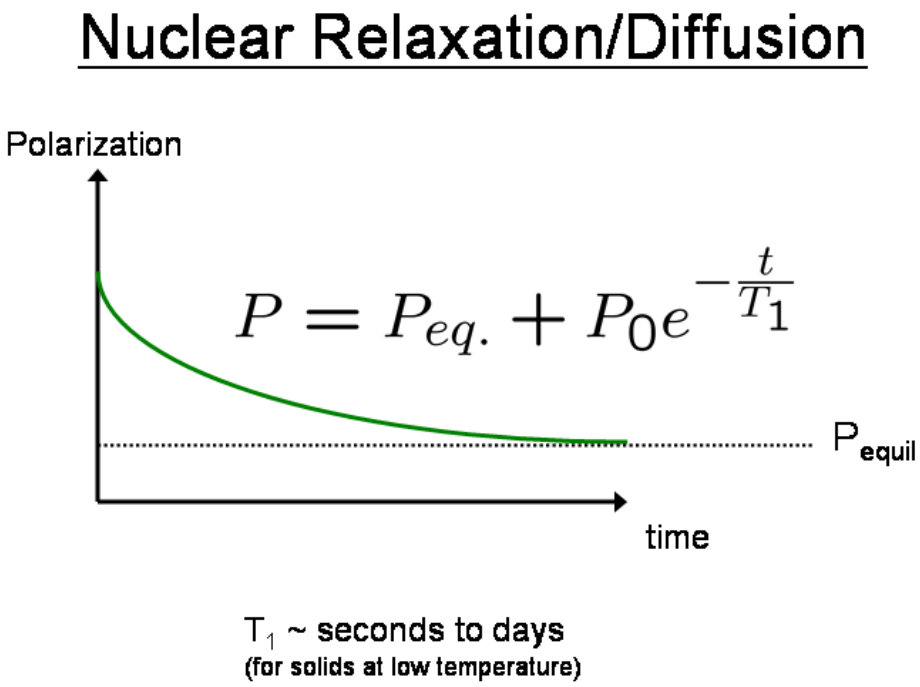

Figure 8.22: Idea behind nuclear relaxation and spin decay

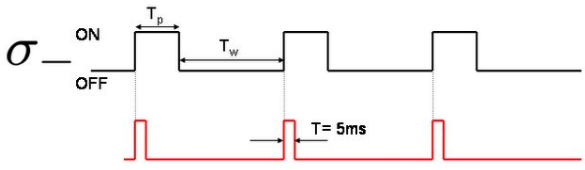

Figure 8.23: Relaxation timescale measurement timing diagram.

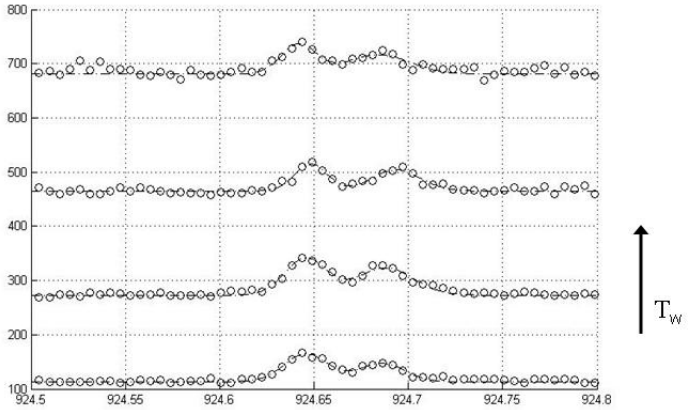

Figure 8.24: A plot of the raw data from the relaxation experiment with $T_w = (0.1s, 5s, 10s, 20s)$

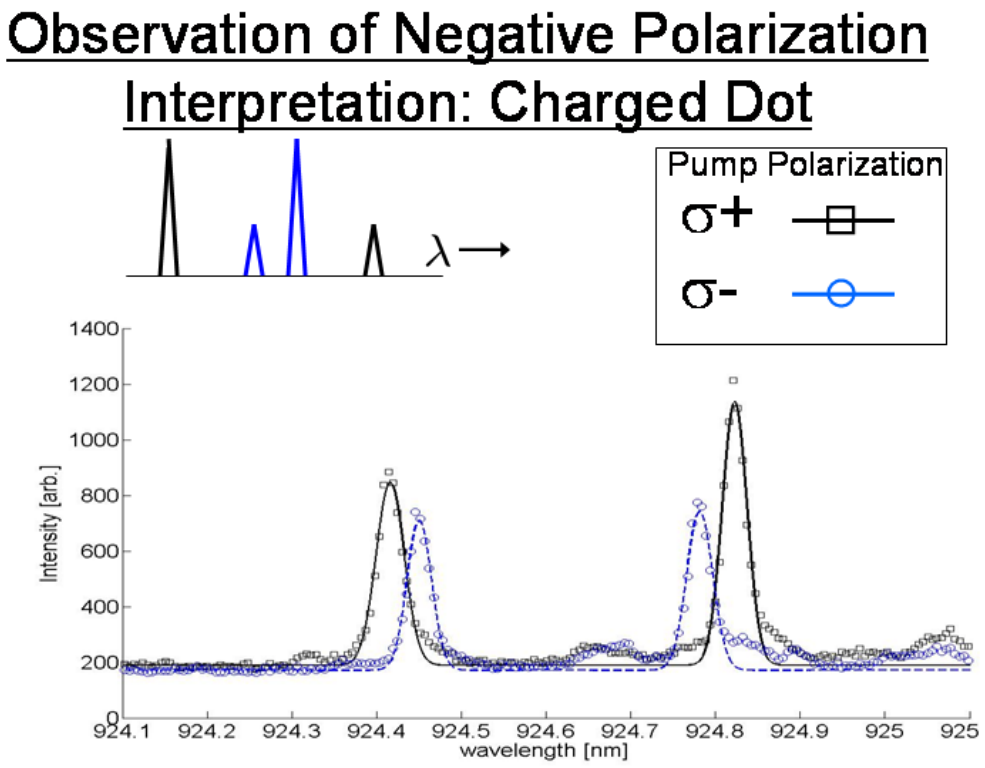

Figure 8.25: Charge State

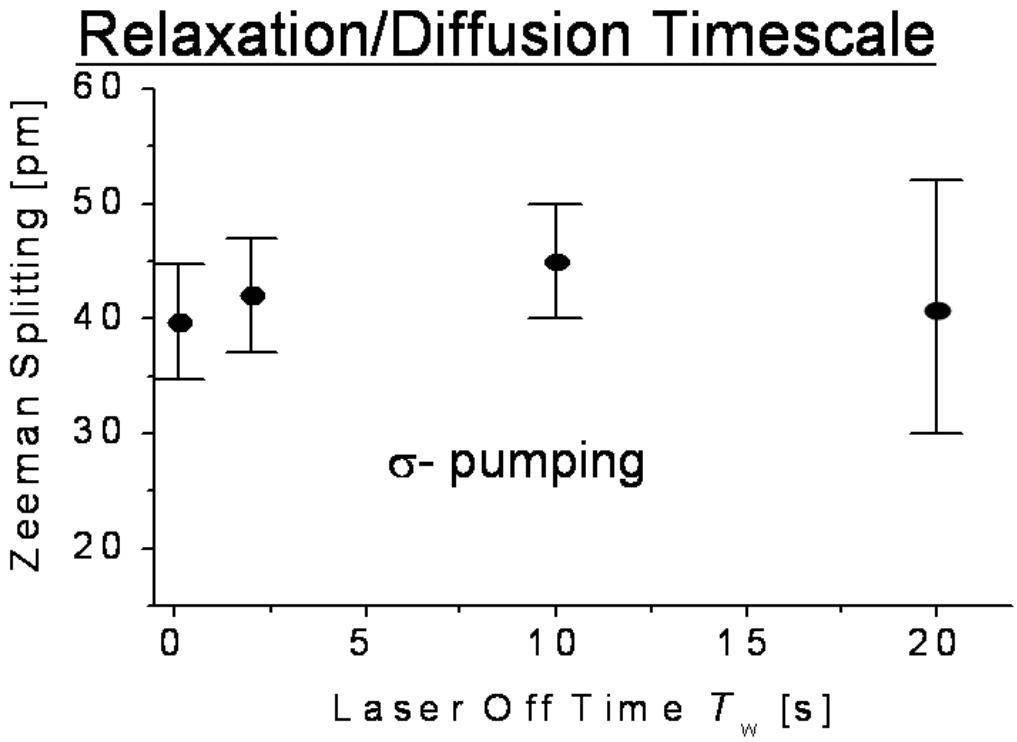

Figure 8.26: Nuclear Relaxation/decay for charge state. This plot shows the peak splitting under σ_-pumping as a function of wait time according to Figure 8.23

Chapter 9

Future Directions

9.1 Interferometer

Considerable effort was made by myself, Masayuki Shirane, Shinichi Koseki, and Kaoru Sanaka to install an interferometer for performing high spectral resolution measurements. The intent was to do a lock-in type detection of the photoluminescence emission with the applied rf. In this way we could observe the effect of the nuclear spins on the photon emission. This equipment had marginal operational performance and given the difficulties we discovered with rf in InAs quantum dots its success will require considerable improvements. Here I will review briefly the operational principle of a Mach-Zender interferometer and the basic idea of how to use digital lock-in detection to observe nuclear spin effects. Such a system will be necessary for any future directions

9.2 Increased Collection Efficiency

In addition to new instrumentation, such as the interferometer or better photon detectors, we can make improvements on the collection efficiency by improving geometrical aspects of the setup. Although this sounds intuitive and simple it actual leads to some experimental challenges. Already we have inserted a lens into the re-entrant bore of the magnet and the lens is very near the window. This lens is a compound microscope

objective and experiences a field near that of the cental region (∼11 T at maximal field) and so large forces are exerted on the housing and steel screws holding together this compound system. The bore has a limited diameter of 30mm as well so the lens must sit inside the bore and be mounted in such a way that there is some travel. The sample can move vertically by lowering or raising the sample probe. However, lateral motion is only available currently by moving the first lens and this further limits the size of the lens. The lens is about 40mm from the sample and has a diameter of roughly 10mm.

In the current experiment we can only a tiny fraction of all the photons emitted from the quantum dot mesa. The photons are emitted in all directions yet we only collect about 1 percent of them with our current geometry. This limitation is due to the distance the lens is placed from the sample and the diameter of this first lens. The numerical aperture in our system is only 0.18. We can increase this by moving the first lens closer to the sample and adding reflectors to reflect all photons towards the collection optics. In fact one major improvement currently being undertaken is to install a small lens directly on the sample holder which will collimate photoluminescence from quantum dots. This requires, then, careful design in order to properly illuminate the sample with laser light and collect as much available photoluminescence. The current methodology being pursued is to install a micro-stage with non-magnetic parts on the end of the sample rod which can be remotely moved by applying a voltage on a feed-through line. In this way the imaging optics are kept fixed and the sample is moved in order to study different quantum dots. However, the range or motion is limited by the small sample space housing the stages. Such a system is challenging and must work in an extreme environment of 1 K and 11.5T.

9.3 Feedback Stabilization

In addition, to improving the collection efficiency the next most important need is feedback stabilization. We have observe the sample drift and on some evenings the drift was $\sim 1\mu$m/sec which made experiments very tedious and the results unreliable. Recall that in our setup the lens both focuses the laser on the sample and collects

the photoluminescence. As the sample drifts the power delivered to a mesa changes since the focus spot on the sample is drifting. As we observed in Chapter 8 the Overhauser shift is laser power-dependent and so if our delivered laser power is unstable it is difficult to vary other parameters independently. Thus, the mechanical stability of the sample holder is a requirement. Additionally, in order collect sufficient photons under similar conditions we sometimes needed very long integration times. For example, in the experiment described in Section 8.2.4 where we tried to probe the relaxation/diffusion timescale we needed to collect approximately 0.4sec worth of photons. However, with this experiment we could only open a shutter for 5msec every cycle so that we didn't perturb what we were trying measure. Thus, for example, when we let t_w be 30 sec, we required a total integration time on the CCD of approximately, 2480 seconds. This long time is much too long for the system to maintain stability.

It is possible with image processing and piezo-actuators to maintain stability of the sample position assuming the long-term drift of the probe is sufficiently small. The range of motion of the piezo-actuators may not be sufficient to compensate for hundreds of micron of movement. The basic operational principle is to capture an image of the field of view using an image capture card. Then this image or a cropped region is sent to some data processing software (e.g. Matlab or LabView) where relative motion between frames is detected. The relative motion detected can then provide a signal to send to the piezo-actuators to compensate for the sample position drift. Such a system has been implemented in other photoluminescence setups within our research group an in principle it can be implemented in our setup. However, the geometry makes the imaging more difficult in that the same path is used for the pump laser and the collected light. Thus, we rely on optical filters to attenuate the pump laser while transmitting the photoluminescence. Image processing may work with an illumination source that is not going to create excitons ($> 1\mu$m) or on a portion of the sample not being studied but with a higher energy light source. In the former, the difficulty arises in finding with a CCD array that operates well at such long wavelengths while for the latter the difficulty is creating a suitable optical setup that such an optical path can be integrated into the optical setup as shown in

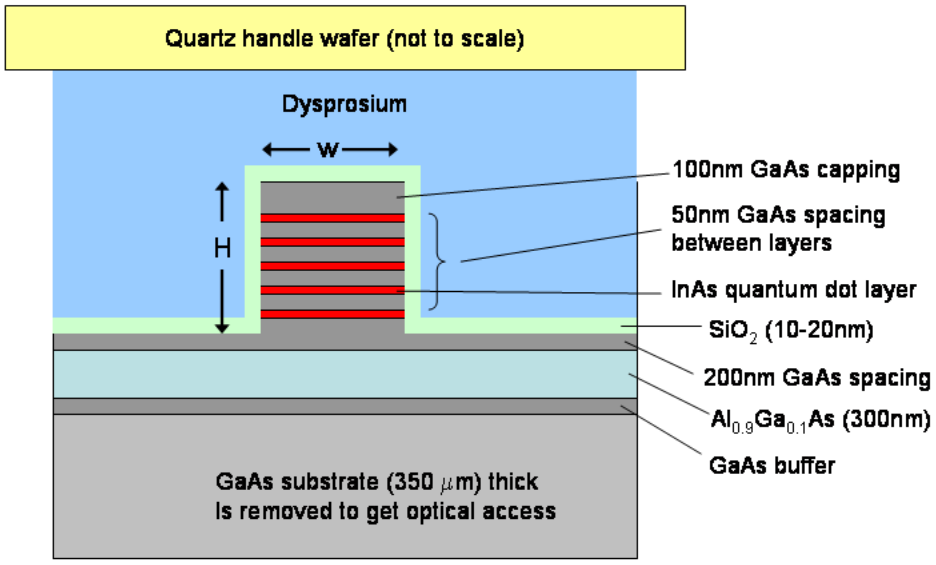

Figure 9.1: 5 Layer device

Figure 5.8.

9.4 5-layer structure

For direct observation of the magnetic field variation within a nano-void of magnetic material, a multi-layer quantum dot structure can be used. The structure, as depicted in 9.1 has been grown by Dr. Bingyang Zhang and individual quantum dots from this structure have been observed 9.4. An integrated device with the magnetic structure has been fabricated but no detectable effect from the magnetic material was observed.

9.5 GaP quantum computer

A promising new direction of research that is being pursued is the insertion of a monolayer of P within a GaAs quantum dot. This structure is also being grown by Dr. Zhang using MBE techniques and by collaborator Prof. Charles Tu at UC San Diego. Many areas need to be addressed including detection of single nuclear spins, 2-d field gradient design, etching process, and implementation of a logical buffer region.

9.6 Magnetic Resonance Force Microscopy

Although we abandoned our research effort with magnetic resonance force microscopy (MRFM), this avenue or work still holds promise and may in the long run be a more versatile means of detecting nuclear spins from an arbitrary crystal. It seems that our philosophy has shifted to using materials where optical detection is possible since if a material can be detected optically there is hope that nuclear polarization can be achieved using optical injection of of excitons or free carriers. However, there many be other means of polarizing nuclear spins (EXAMPLE and REF) or in certain geometries the coupling between individual nuclear spins is too weak for detection by optical means. Given the importance and favorable scaling behavior some discussion of magnetic resonance force microscopy is warranted.

9.7 Nanowires

The discussion so far has focused exclusively on engineering large magnetic field gradients using ferromagnetic materials. Large field gradients may also be achievable using current carrying wires. These wires have the added advantage that the magnetic field can be tuned and the field gradient can be completely removed by changing the amount of current that flows through them. An absence of any magnetic field variation allows for some decoupling pulse sequences which have a more favorable scaling behavior than decoupling pulse sequences which operate in the presence of magnetic field gradients.

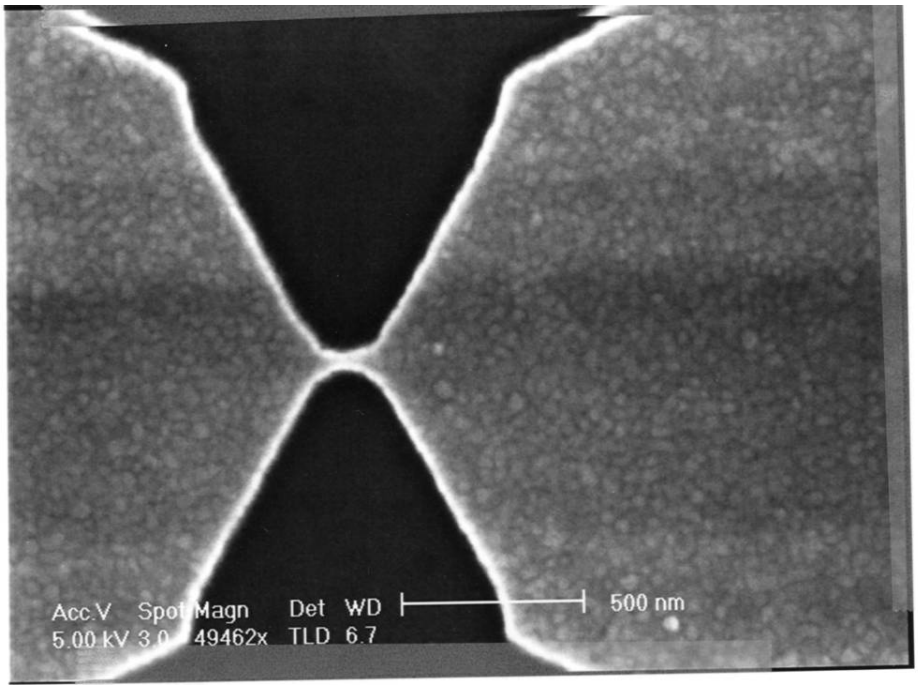

Figure 9.2: SEM showing the gold nanowires.

Some preliminary work was done in collaboration with Dr. Mark Topinka who was pursuing post-doctoral research under Prof. Goldhaber-Gordon. We fabricated some nanowires (see figure) of dimension 150nm long with a cross-section of 50nm X 50nm made from deposited gold. Graduate student Jon Schuller tested these devices in a low temperature probe station operating at 4 K.

Devices failed between 100 mA and 500 mA and by failure I mean an open circuit was observed. The observed resistance values before breakage were R = 10 20 Ohms and afterward failure it became infinite. The current densities present are extremely large at 10^{13} to 10^{14} Am^2 which is 3 to 4 orders of magnitude larger than what is present in a pentium chip.

This line of research, and similar unpublished work done previously by Prof. David Goldhaber-Gordon could lead to useful devices. Already with gold nanowires large current densities have been achieved and it is believed that other metals such as copper will not suffer from electromigration in the way that soft metals like gold

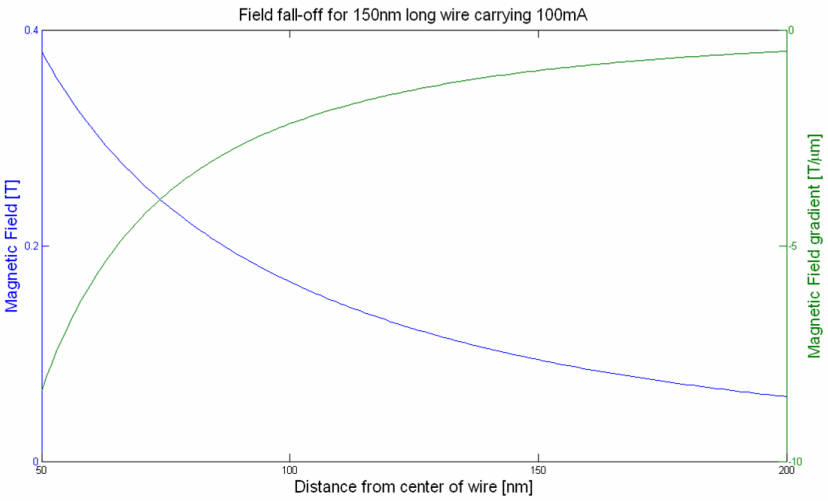

Figure 9.3: Field and Field gradient near a nanowire

do. Future ideas may include using multi-walled carbon nanotubes which are even smaller than metallic nanowires. The multi-walled nanotubes may be able to carry larger current densities.

Chapter 10

Conclusions

To following are the main results presented in this thesis:

1. We have presented designs for magnets that provide sufficient magnetic field gradients for addressing single nuclear spins.

2. We have demonstrated that single quantum dots can be used to measure magnetic fields with high spatial resolution.

3. We have measured the effect of a small magnet on the photoluminescence from single quantum dots and have concluded that they are consistent with our calculations and therefore the magnets should provide the necessary field gradients

4. We have observed nuclear spin polarization due to circularly polarized pump light. We have determined the timescale over which the nuclear spin polarization develops. Additionally, we have observed that the shifts we have observed remain for at least 20 seconds which provides strong evidence that the mechanism at play is indeed nuclear spin interaction.

5. We have presented a model which is consistent with the observed timescales of order $\sim$ 1ms to tens of milliseconds which is the fastest measured timescale of any known solid-state system.

6. We have observed nuclear polarization among the indium nuclei reach 10% and for arsenic it saturates at about 30%.

7. We have observed negative polarization in single self-assembled InAs quantum dots. This, we believe, can be attributed a negative trion states. In addition we have observed nuclear polarization behavior in charge states similar to the neutral dots.

Appendix A

Fluorapatite based quantum computer

A proposal for a solid-state implementation of a quantum computer is presented. Qubits are nuclear spins arranged as one-dimensional chains with resonant frequencies separated by a large field gradient. Initialization is accomplished by optical pumping, algorithmic cooling, and pseudo-pure state techniques. Quantum logic is accomplished using nuclear-nuclear dipolar couplings with RF pulse sequences. Magnetic resonance force microscopy is used for readout. This proposal takes advantage of many of the successful aspects of solution NMR quantum computation, including ensemble measurement and long decoherence times, but it allows for more qubits and improved initialization. Two systems are proposed: One uses fluorine nuclear spins in a natural solid crystal of fluorapatite [$Ca_5F(PO_4)_3$] while the other uses isotope engineering to construct ideal one-dimensional chains of ^{29}Si nuclear spins in a ^{28}Si (spin-0) matrix.

A.1 Introduction

An increasing number of theoretical developments have recently motivated the construction of a quantum computer with a large number of qubits. The potential for efficient simulation of quantum systems [14], the discoveries of algorithms for fast

factorization [86] and database searching [8], and the development of quantum error correction [87] have helped to spur a large number of proposals for experimental implementations of a quantum computer. However, any physical implementation of a quantum computer must battle the fact that well-isolated quantum systems are difficult to couple and to measure, whereas the introduction of necessary couplings and probes leads to the devastating effects of decoherence.

To date, the most successful experimental realization of a multi-qubit quantum computer (or at least a simulation thereof) has been in room-temperature solution NMR [19]. Here, the spin-states of molecular nuclei in a solution are well isolated, as demonstrated by long thermal relaxation times (T_1) of many seconds. The nuclei of each molecule are weakly coupled by scalar couplings. Measurement without substantial decoherence is made possible by the large ensemble of $\sim 10^{22}$ uncoupled, identical molecules in the solution. There is much debate, however, as to whether solution NMR currently does or ever will exhibit the signatures of truly *quantum* information processing [88]. The presence of a large, mixed ensemble renders quantum entanglement and wave-function collapse of individual spins unmeasurable. Certain manipulations allow the processing of an "effective pure state" in which the ensemble behaves nearly identically to a single quantum system [19, 89]. However, it has been shown that the evolution of effective pure states of existing solution NMR computers can be described without any entanglement, and either more qubits or much larger nuclear polarizations will be needed before entanglement is demonstrable [90]. Even if we neglect the debate of what is "quantum" and what is not, the principal limitation due to the small polarizations in solution NMR quantum computation is that the usable signal decreases exponentially with the number of qubits, leaving this method unlikely to exceed the 10 qubit level without extensive modification [91].

In this letter, we propose an implementation using solid-state NMR. In a solid crystal there exists the potential for polarization of the nuclear spins by cooling of the network of spins to extremely low temperatures. This is most readily achieved by the introduction of polarized electrons which can interact via a hyperfine coupling with the nuclear spins and transfer their polarization to them. Additionally, the thermal relaxation time T_1 can be dramatically lengthened when moving from

a solution to an insulating, nonmagnetic crystal, and the nuclear-nuclear coupling can be faster. Hence, a solid crystal has great potential for quantum computation in terms of timescales [38] and scalability.

These advantages, however, come at a cost: several difficult and related problems arise in implementing a solid-crystal NMR computer. This letter, although not the first proposal for quantum computation in a crystal lattice [2], provides new approaches to these problems. One problem is the complicated network of dipolar couplings in a solid, which must be suppressed to slow T_2 decoherence but selectively retained for logic. We address this problem with both "selective averaging" radio frequency (RF) pulse sequences and a well-chosen crystal structure. Another problem arises from the need to distinguish and detect nuclei in the periodic lattice of a crystal; for this we establish a very large, static, one-dimensional magnetic field gradient with a microfabricated, high-magnetization ferromagnet [92]. Only a small ensemble of nuclei may fit into the area over which the gradient field is homogeneous, and therefore a more sensitive means than standard inductive pick-up is needed to measure the nuclear spin states. We propose using magnetic resonance force microscopy (MRFM).

A general schematic for the solid-crystal quantum computer we propose appears in Fig. **??**. The quantum computer is an ensemble of N one-dimensional chains of n spin-1/2 nuclei. Due to the field gradient, the resonant frequencies of the nuclear spins within a chain are different. Hence the secular component of the dipolar Hamiltonian which couples the ith spin to the jth spin within the mth chain is written [75]

$$\begin{aligned} \hat{\mathcal{H}}_{ijmm} &= \frac{\mu_0}{4\pi}\gamma^2\hbar^2\frac{1-3\cos^2\phi}{[|j-i|a]^3}\hat{I}^z_{im}\hat{I}^z_{jm} \\ &\equiv \hbar\delta\omega_{ij}\hat{I}^z_{im}\hat{I}^z_{jm}, \end{aligned} \tag{A.1}$$

where γ is the gyromagnetic ratio ($2\pi \times 40$ MHz/T for ^{19}F and), a is the distance between spins in a chain, and ϕ is the angle between the chain of spins and the large applied magnetic field, which is taken to be in the z-direction. Other terms of the dipolar Hamiltonian average to zero on a timescale of $1/\Delta\omega_{ij}$ or faster, where $\Delta\omega_{ij} = \gamma a|\nabla B^z_{ij}|$ is the separation of the ith and jth resonant frequencies caused

by the field gradient ∇B_{ij}^z between them. The Hamiltonian of Eq. (A.1) may be "switched off" by applying a periodic succession of narrow band π pulses at, for instance, the ith resonant frequency [75]. Simultaneous decoupling of more than two qubits may be accomplished by timing the selective π pulses according to the entries of an appropriately sized Hadamard matrix; a pair of qubits may be selectively recoupled in order to implement two-bit gates [93].

A.2 Decoupling and Quantum Logic

Non-disturbing measurement is possible in this scheme because, orthogonal to the chain direction, a nucleus of resonant frequency ω_i has a large plane of copies with equal frequency. The coupling between copies has a different form; the nth and mth nucleus of identical resonant frequency ω_i are coupled by the Hamiltonian [75]

$$\hat{\mathcal{H}}_{iimn} = \frac{1}{2}\frac{\mu_0}{4\pi}\gamma^2\hbar^2\frac{1-3\cos^2\theta_{mn}}{(a\lambda_{mn})^3}\left(3\hat{I}_{im}^z\hat{I}_{in}^z - \hat{\mathbf{I}}_{im}\cdot\hat{\mathbf{I}}_{in}\right),$$

where λ_{mn} is the distance between the two nuclei in units of a, and θ_{mn} is the angle between the vector which connects them and the direction of the applied field. This coupling between copies must be "switched off" to prevent interference between ensemble members. Decoupling these spins may be done by any number of pulse sequences which have been developed over the past 40 years in solid-state NMR, the simplest of which is the WAHUHA pulse sequence. Such sequences can reduce dipolar broadening by more than three orders of magnitude [94].

Fortunately, the different forms of $\hat{\mathcal{H}}_{ijmm}$ and $\hat{\mathcal{H}}_{iimn}$ allow constant decoupling of copies without adverse effect on the manipulations of couplings within individual computers. The qubit-qubit coupling of Eq. (A.1) may in general be rescaled and rotated by the broadband WAHUHA-type sequence, but it may still be controlled for logic gates with suitably phased π pulses. The broadband WAHUHA-type pulse sequence which decouples all copies is unaffected by the addition of selective π-pulses, insofar as those π-pulses are sufficiently short in comparison to the pulse spacing. This criterion is difficult to meet, since the π pulses must last a time of about $1/\Delta\omega_{i,i+1}$

to be frequency selective.

The only problematic dipolar couplings which remain after applying the pulse sequences described above are those between qubits with different resonant frequencies ($i \neq j$) and in different chains ($m \neq n$). These couplings only arise when two planes of qubits are selectively recoupled during a two-bit gate. The needed time duration for a logic operation may be minimized by maximizing the desired qubit-qubit coupling – this is accomplished by first letting a be the smallest nuclear distance in the crystal. Second, we set $\phi = 0$, hence putting the gradient parallel to the applied field. Third, only nearest-neighbor qubit couplings are used ($j = i + 1$), with longer distance couplings accomplished by bit-swapping [95]. After making these choices, we have $\delta\omega \equiv \delta\omega_{i,i+1} = -\mu_0\gamma^2\hbar/2\pi a^3$, and the target qubit of frequency ω_i in the mth chain is coupled to control qubit copies at ω_{i+1} in the other chains by the Hamiltonian

$$\begin{aligned} \hat{\mathcal{H}}^*_{im} &= -\hbar\delta\omega \sum_n \frac{\lambda_{mn}^2 - 2}{2(1+\lambda_{mn}^2)^{5/2}} \hat{I}^z_{im}\hat{I}^z_{i+1,n} \\ &\equiv -\hbar\delta\omega \sum_n b_{mn}\hat{I}^z_{im}\hat{I}^z_{i+1,n}. \end{aligned} \tag{A.2}$$

The decoherence caused by this undesired Hamiltonian is minimized if the coupling constants are sufficiently small to obey

$$\frac{\sigma}{\delta\omega} = \frac{1}{2}\sqrt{\sum_n b_{mn}^2} \ll 1, \tag{A.3}$$

where σ (the square root of the second moment [94]) is the effective linewidth of the qubit ensemble during recoupling, which we demand to be much smaller than the splitting $\delta\omega$. This inequality is best satisfied by a crystal whose nuclei couple only in isolated chains.

A.3 Candidate Crystalline Systems

A crystal which approximates this description is fluorapatite, $Ca_5F(PO_4)_3$, whose ^{19}F. In fluorapatite, we find $\sigma/\delta\omega \approx 1/58$, roughly six times smaller than in a simple

cubic crystal such as CaF_2. The one-dimensional nuclear structure of fluorapatite has been recognized in several NMR experiments. Decoherence timescales in this crystal are analagous to the well-known case of CaF_2. The T_2 time is limited by dipolar broadening; if dipolar couplings are perfectly controlled, the timescale for internal decoherence is pushed toward the spin-lattice relaxation time constant T_1, which is limited by thermal fluctuations of paramagnetic impurities (rare-earth substitutions, for example) and can easily be several hours for reasonable crystal purities and temperatures.

The advantages of an all silicon implementation are many. Foremost, the crystal growth and processing technology for silicon are highly matured. In particular, the most sensitive structures for force detection have been made from pure silicon. Also, it is good fortune that the family of stable nuclear isotopes of silicon is quite simple: 95.33% of natural silicon is ^{28}Si or ^{30}Si, which are both spin-0, and 4.67% is ^{29}Si, which is spin-1/2, perfect for the qubit. Thus silicon is well suited for isotope engineering [96]. Another crucial motivation for the choice of silicon is the observation that nuclei in a semiconductor may be polarized by cross-relaxation with optically excited, spin-polarized conduction electrons [97]. Although there are many other means for dynamic nuclear polarization, optical pumping in semiconductors has one important feature: the electrons whose hyperfine couplings make the polarization possible recombine shortly thereafter and hence do not contribute to decoherence during computation. The lack of any spurious spins, nuclear or electronic, should leave the ^{29}Si nuclei well decoupled from their environment. Finally, we note that the use of silicon for a quantum computer opens the door for integration of quantum information processing technology with silicon CMOS and SET circuits.

A.4 Initialization and achieving an low spin temperature

For initialization of the quantum computer, we employ optical pumping, algorithmic cooling, and pseudo-pure state techniques. The premise of optical pumping is that

nuclei exchange Zéeman energy with a bath of photoexcited electrons and thereby relax thermally to an effective spin temperature corresponding to the non-equilibrium electron-spin polarization. Once those electrons recombine, the nuclei retain their spin polarization for the "dark" T_1 time, which is extremely long (200 hours in Ref. [97]). In low-field experiments ($\sim$ 1 G), the electron spin polarizations which have been obtained in pure silicon have been limited due to unfavorable selection rules. Also, the long recombination time due to the indirect bandgap prevents rapid recooling of the electron bath. Consequently, nuclear polarizations have not exceeded 0.1% in these experiments. Improved nuclear polarization may be observable in higher magnetic fields ($\sim$10 T) and in smaller structures where rapid recombination of surface states is important.

A.5 Field Gradient

The field gradient is accomplished by a micron-sized ferromagnetic parallelopiped. Calculations similar to those in Ref. [92] show that such a magnet, made of dysprosium and placed in a 7 T external field can produce a field gradient of 1.4 T/μm at a distance of 2.07 μm above the magnet, which leads to $\Delta\omega \equiv \Delta\omega_{i,i+1} = 2\pi \times 19.2$ kHz. A 1 μm by 10 μm fluorapatite crystal above the magnet contains $N = 10^7$ equivalent-frequency qubit copies in each xy-plane. The field variation along the y-direction is negligible since the magnet is much longer than the crystal. The field variation along the x-axis is sufficiently small that all of the equivalent-frequency nuclei lie within a bandwidth of $\Delta\omega$. We also note that inhomogeneous broadening is constantly refocused in this scheme by the narrow-band π pulse sequences during both decoupling and selective recoupling.

A.6 Readout

The presence of a large magnetic field gradient provides a natural means for performing MRFM on a magnetization M^z, since this technique is sensitive to the gradient

force given by $F = M^z \nabla B^z$ [**?**]. The crystal is mounted on a microfabricated cantilever which oscillates in the z-direction. The long axis of the crystal-cantilever heterostructure and magnet are aligned. The experiment is performed in high vacuum ($< 10^{-5}$ torr) and at low temperatures. A coil is used to generate the RF pulses for logic operations and decoupling sequences; it also generates the continuous-wave radiation for readout. An optical fiber-based displacement sensor is used to monitor deflection of the cantilever using interferometry. Sub-Ångstrom oscillations can be detected; larger oscillations can be damped with active feedback which avoids additional broadening while maintaining high sensitivity.

Readout is performed using cyclic adiabatic inversion [49], which modulates the magnetization of a plane of nuclei at a frequency near or on resonance with the cantilever. The spins of resonant frequency ω_i are irradiated with the RF field $B^x = 2B_1 \cos\{\omega_i t - (\Omega/\omega_m)\cos(\omega_m t)\}$, where ω_m is the modulation frequency chosen to be near the resonance of the cantilever, and Ω is the frequency excursion, which should be much smaller than $\Delta\omega$ [98]. Simultaneous detection of signal from multiple planes is possible if the different planes to be measured are driven at distinct modulation frequencies ω_m.

The force resolution for MRFM is limited by thermal fluctuations of the cantilever. Force resolutions of 5.6×10^{-18} N/$\sqrt{\text{Hz}}$ have been reported for single crystal cantilevers at 4 K [**?**]. To estimate the force involved in a measurement following a quantum computation, we consider the case in which initialization is imperfect, so that the temperature T is non-zero and an effective pure state must be used [19, 89]. The usable magnetization is estimated [91] as

$$M^z = \gamma\hbar \frac{N}{2^n} \frac{\sinh(n\hbar\gamma B_0/2k_{\mathrm{B}}T)}{\cosh^n(\hbar\gamma B_0/2k_{\mathrm{B}}T)}.$$

In the high temperature limit, this magnetization approximates to $(\gamma^2\hbar^2 B_0/2k_{\mathrm{B}}T)Nn2^{-n}$ showing the exponential downscaling which plagues solution NMR. Even in this limit, with the relatively small N of 10^7 and using the field gradient described above in a 7 T field at 4 K, the force which needs to be measured works out to about $10^{-15}n2^{-n}$ newtons, allowing $n \sim 10$ qubits. The density matrix of such a system would be outside

the neighborhood in which it has been shown that all density matrices are separable. The situation is improved in larger fields and at lower temperatures, where M^z improves exponentially in B_0/T. In the realistic laboratory extreme $B_0 = 20$ T and $T = 10$ mK, this design may scale to $n \sim 300$ qubits; in this regime entanglement is shown to be demonstrable.

A.7 Scalability

A primary limitation to the long-term scalability of this scheme is the number of logic gates which can fit into the decoherence time when there is a large number of qubits. The decoupling/recoupling pulse scheme based on Hadamard matrices has a cycle time $t_c(n)$ of $Ln^2/\Delta\omega$, where the parameter L depends on the length of the homonuclear decoupling subsequence and only weakly on the number of qubits n [93]. Since single spin rotations must occur between cycles, the clock speed is set by this cycle time. The number of logic gates we may perform is approximately $t_c(n)$ divided into the remaining decoherence time T_2^0. This timescale T_2^0 is due to residual homonuclear couplings, cantilever thermal drift, and thermal relaxation resulting from magnetic impurities; these contributions are limited by the experimental performance of the homonuclear decoupling pulse sequence, cantilever feedback stabilization, and crystal growth technique, respectively. Figure **??** shows the number of logic gates possible for several values of T_2^0. The bottom dashed trace ($T_2^0 = 100$ ms) corresponds to the case in which homonuclear couplings are perfectly controlled but cantilever drift is completely unsuppressed, while the middle ($T_2^0 = 10$ s) and top ($T_2^0 = 1000$ s) traces assume suppression by 20 and 40 dB with a negative feedback circuit. The limited number of gates at high numbers of qubits is a remaining problem which may be addressed through error correcting codes [87], more sophisticated pulse sequences, or the use of a more one-dimensional system .

A.8 Summary

This proposal features two important advantages over schemes using solid-state NMR with impurity dopants [26, 99]. The fabrication difficulty of artificially implanting controlled arrays of spins is avoided in our proposal by using nuclei that are naturally organized into a crystal structure. Also, the use of an ensemble of 10^7 spins avoids the need for the daunting task of reading and initializing single nuclear spins. Indeed, ensemble measurement has given solution NMR a developmental head-start against other existing proposals for quantum computation, and it is hoped that the scheme presented here will carry NMR quantum computation onward to the many-qubit regime.

Appendix B

Matlab Rate Equation Code

The code below was used to calculate the nuclear polarization timescale versus pump laser power.

```
clear all
% pumping rates
x=-11:0.1:-7;
lp = 10.^x; %effective laser power
% lp=10^-9;
for i=1:length(lp)
    laser_power=lp(i);
%sigma plus pumping
P_plus1_down = 1/laser_power; P_plus1_up = 1/laser_power;
P_minus1_down = 0; P_minus1_up = 0;
%sigma minus pumping
P_plus1_down = 0; P_plus1_up = 0; P_minus1_down = 1/laser_power;
P_minus1_up = 1/laser_power;
%
% radiative recombination
w_r=1/0.5e-9; %(same for all bright states)
```

```
B=10;

%
% phonon rates
muB = 5.7e-6; % eV
kb=8.617e1; % microeV/K
beta = muB*kb;
T=1.5; %Kelvin
d0=100e-6; d1=50e-6; d2=50e-6; ge=-2; gh=-1; beta1=muB*(ge+gh)*B;
beta2=-muB*(ge-gh)*B; E_plus1 = 0.5*d0+0.5*sqrt(d1^2+beta1^2);
E_minus1 = 0.5*d0-0.5*sqrt(d1^2+beta1^2); E_plus2 =
-0.5*d0+0.5*sqrt(d2^2+beta2^2); E_minus2 =
-0.5*d0-0.5*sqrt(d2^2+beta2^2);

% spin-flip assisted radiative recombination
w_plus = nulcear_polarization_rate((E_plus2-E_plus1)); w_minus =
nulcear_polarization_rate((E_minus2-E_minus1));

% w_plus=1/0.2e-3; %spin-flip radiative recombination from plus2 via plus1
% w_minus=1/1e-3; %spin-flip radiative recombination from minus2 via minus1

% Hole spin relaxation due to phonon interaction
w_1_a=1/1e-9; %going from +1 to -2
w_1_b=w_1_a*exp(-beta*(E_minus2-E_plus1)); %going from -2 to +1
w_2_a=1/1e-9; %going from -1 to +2
w_2_b=w_2_a*exp(-beta*(E_minus1-E_plus2)); %going from +2 to -1
%
%
% n_GS_down
```

```
% n_GS_up
% n_plus1_down
% n_plus1_up
% n_minus1_down
% n_minus1_up
% n_plus2_down
% n_plus2_up
% n_minus2_down
% n_minus2_up
%

M=zeros(10,10);

M(1:10,1:2) = [-(P_plus1_down+P_minus1_down)                    0;
               0                       -(P_plus1_up+P_minus1_up);
               P_plus1_down                                     0;
               0                                         P_plus1_up;
               P_minus1_down                                    0;
               0                                       P_minus1_up;
               0                                                0;
               0                                                0;
               0                                                0;
               0                                                0;
               ];

M(1:10,3:6) = [w_r          0          w_r          0;
               0            w_r        0           w_r;
             -w_r-w_1_a     0          0           0;
               0        -w_r-w_1_a     0           0;
               0            0       -w_r-w_2_a     0;
               0            0          0        -w_r-w_2_a;
```

```
                0           0          w_2_a       0;
                0           0          0           w_2_a;
              w_1_a         0          0           0;
                0         w_1_a        0           0;
                ];

M(1:10,7:10) = [0           0          0           w_minus;
                w_plus      0          0           0;
                0           0          w_1_b       0;
                0           0          0           w_1_b;
                w_2_b       0          0           0;
                0          w_2_b       0           0;
            -w_plus-w_2_b   0          0           0;
                0         -w_2_b       0           0;
                0           0         -w_1_b       0;
                0           0          0       -w_1_b-w_minus;
                ];

[V,D]=eig(M);

n0 = [0.5 0.5 0 0 0 0 0 0 0 0]';

c=inv(V)*n0;


% t=10.^[-9:0.2:0];
% n=zeros(10,length(t));
% for i=1:length(t)
% for k=1:10
%  n(:,i)=n(:,i)+c(k)*V(:,k)*exp(V(k,k)*t(i));
% end
```

```
% end



decay_rates=D*ones(10,1); ordered_decay_rates=sort(decay_rates);

for j=9:-1:1
    j;
 if (ordered_decay_rates(j)~=0)
    p(i)=abs(1/ordered_decay_rates(j));
    break
 end
end

end loglog(1./lp,1e3*p,'ko') XLABEL = 'Exciton Capture Rate
[s^{-1}]'; YLABEL = 'Polarization Timescale [ms]';
set(get(gca,'XLabel'), 'String', XLABEL, 'FontSize', 30);
set(get(gca,'YLabel'), 'String', YLABEL, 'FontSize', 30); set(gca,
'Fontsize', 26);
```

Bibliography

[1] J. E. M. Haverkort W. van der Vleuten J. Brbach, A. Yu. Silov and J. H. Wolter. Coupled ultrathin inas layers in gaas as a tool for the determination of band offsets. *Superlattices and Microstructures*, 20:527–532, 1997.

[2] Y. Yamamoto F. Yamaguchi. Crystal lattice quantum computer. *Appl. Phys. A*, 68.

[3] Charles M. Santori. *Generation of Nonclassical Light Using Semiconductor Quantum Dots*. PhD thesis, Stanford University, 2002.

[4] C. Santori, M. Pelton, G. Solomon, Y. Dale, and E. Yamamoto. Triggered single photons from a quantum dot. *Physical Review Letters*, 86(8):1502 – 5, 2001 2001.

[5] C. Santori, D. Fattal, J. Vuckovic, G. S. Solomon, and Y. Yamamoto. Indistinguishable photons from a single-photon device. *Nature*, 419(6907):594 – 7, OCT 2002.

[6] M. Bruchez, M. Moronne, P. Gin, S. Weiss, and A. P. Alivisatos. Semiconductor nanocrystals as fluorescent biological labels. *Science*, 281(5385):2013 – 16, Sep 1998.

[7] W. C. W. Chan and S. M. Nie. Quantum dot bioconjugates for ultrasensitive nonisotopic detection. *Science*, 281(5385):2016 – 18, Sept. 1998.

[8] L. K. Grover. Quantum mechanics helps in searching for a needle in a haystack. *Physical Review Letters*, 79(2):325 – 8, JUL 1997.

[9] T.D. Ladd, J. R. Goldman, F. Yamaguchi, Y. Yamamoto, E. Abe, and K.M. Itoh. All-silicon quantum computer. 89:17901, 2002.

[10] T. D. Ladd, Y. Yamamoto, J. R. Goldman, and F. Yamaguchi. Solid-state crystal lattice NMR quantum computation. *Quantum Information and Computation*, 1:56, 2001.

[11] K-M. C. Fu, T. D. Ladd, C. Santori, and Y. Yamamoto. Optical detection of the spin state of a single nucleus in silicon. 69:125306, 2004.

[12] J. M. Taylor, C. M. Marcus, and M. D. Lukin. Long-lived memory for mesoscopic quantum bits. *Physical Review Letters*, 90(20):206803/1 – 206803/4, May 2003.

[13] Isaac L. Chuang Michael A. Nielsen. *Quantum Computation and Quantum Information*. Cambridge University Press, 2000.

[14] S. Lloyd. Universal quantum simulators. *Science*, 273(5278):1073 – 8, AUG 1996.

[15] R.P. Feynman. Simulating physics with computers. *Int. J. Theor. Phys.*, 21.

[16] D. P. DiVincenzo. The physical implementation of quantum computers. *Fortschr. Physik*, 48(9-11):771–783, 2000.

[17] Thaddeus D. Ladd. *Quantum Computing with Nuclear Spins in Seminconductors*. PhD thesis, Stanford University, 2005.

[18] T. F. Havel D. G. Cory, A. F. Fahmy. *Proceedings of the Fourth Workshop on Physics and Computation*, 1996.

[19] N. A. Gershenfeld and I. Chuang. Testing 123. *Science*, 275, 1997.

[20] J. I. Cirac and P. Zoller. Quantum computations with cold trapped ions. 74:4091, 1995.

[21] D. Kielpinski, C. Monroe, and D. J. Wineland. Architecture for a large-scale ion-trap quantum computer. *Nature*, 417:709, 2002.

[22] P. Domokos, J. M. Raimond, M. Brune, and S. Haroche. Simple cavity-qed two-bit universal quantum logic gate: the principle and expected performances. *Physical Review A (Atomic, Molecular, and Optical Physics)*, 52(5):3554 – 9, 1995.

[23] Cooling the collective motion of trapped ions to initialize a quantum register. 81:1525, 1998.

[24] Y. Yamamoto, M. Kitagawa, and K. Igeta. Quantum mechanical aspects of optical communication and optical computing., 1988.

[25] I. L. CHUANG and Y. YAMAMOTO. Simple quantum computer. *Physical Review A (Atomic, Molecular, and Optical Physics)*, 52(5):3489 – 96, NOV 1995.

[26] B. E. Kane. A silicon-based nuclear spin quantum computer. *Nature*, 393(6681):133 – 7, May 1998.

[27] J. E. Mooij. The 24th international conference on the physics of semiconductors.

[28] S. Bandyopadhyay and V. Roychowdhury. Computational paradigms in nanoelectronics: quantum coupled single electron logic and neuromorphic networks. *Japanese Journal of Applied Physics, Part 1 (Regular Papers, Short Notes & Review Papers)*, 35(6A):3350 – 62, Jun 1996.

[29] V. P. Roychowdhury, D. B. Janes, S. Bandyopadhyay, and X. D. Wang. Collective computational activity in self-assembled arrays of quantum dots: a novel neuromorphic architecture for nanoelectronics. *IEEE Transactions on Electron Devices*, 43(10):1688 – 99, Oct 1996.

[30] Lieven M. K. Vandersypen. *Experimental Quantum Computation with Nuclear Spins in Liquid Solution*. PhD thesis, Stanford University, 2001.

[31] J. A. SIDLES. Noninductive detection of single-proton magnetic resonance. *Applied Physics Letters*, 58(24):2854 – 6, JUN 1991.

[32] D. RUGAR, C. S. YANNONI, and J. A. SIDLES. Mechanical detection of magnetic resonance. *Nature*, 360(6404):563 – 6, Dec 1992.

[33] J. A. SIDLES and D. RUGAR. Signal-to-noise ratios in inductive and mechanical detection of magnetic resonance. *Physical Review Letters*, 70(22):3506 – 9, MAY 1993.

[34] D. Rugar, R. Budakian, H. J. Mamin, and B. W. Chui. Single spin detection by magnetic resonance force microscopy. *Nature*, 430(6997):329 – 32, Jul 2004.

[35] J. Wrachtrup, A. Gruber, L. Fleury, and C. von Borczyskowski. Magnetic resonance on single nuclei. 267:179, 1997.

[36] Yoshihisa Yamamoto. The quantum optical repeater. *Science*, 263:1295–198, 1997.

[37] J. Vučković and Y. Yamamoto. Photonic crystal microcavities for cavity quantum electrodynamics with a single quantum dot. 82:2374, 2003.

[38] T. D. Ladd, J. R. Goldman, F. Yamaguchi, and Y. Yamamoto. Decoherence in crystal lattice quantum computation. *Appl. Phys. A: Mater. Sci. Process.*, 71:27, 2000.

[39] A. S. Oja and O. V. Lounasmaa. Nuclear magnetic ordering in simple metals at positive and negative nanokelvin temperatures. *Reviews of Modern Physics*, 69(1):1 – 136, JAN 1997.

[40] A Zunger L.W. Wang, J. Kim. Electronic structures of self-organized inas/gaas quantum dots bounded by 136 facets. *Physical Review B*, 61:2784, 2000.

[41] A Zunger L.W. Wang, J. Kim. Electronic structures of [110]-faceted self-assembled pyramidal inas/gaas quantum dots. *Physical Review B*, 59:5678, 1999.

[42] D. Bimberg O. Stier, M. Grundmann. Electronic and optical properties of strained quantum dots modeled by 8-band $k \cdot k$ theory. *Physical Review B*, 59:5688, 1999.

[43] C. Pryor. Eight-band calculations of strained inas/gaas quantum dos compared with one-,four-, and six-band approximations. *Physical Review B*, 57:7190, 1998.

[44] Paolo Zanardi Fausto Rossi Eliana Biolatti, Irene D'Amico. Electro-optical properties of semiconductor quantum dots: Application to quantum information processing. *Physical Review B*, 65:075306, 2002.

[45] Shun Lien Chuang. *Physics of Optoelectronic Devices*. john Wiley & Sons, Inc., 1995.

[46] A. Shabaev, Al. L. Efros, D. Gammon, and I. A. Merkulov. Optical readout and initialization of an electron spin in a single quantum dot. *Physical Review B (Condensed Matter and Materials Physics)*, 68(20):201305 – 1, 2003.

[47] Pochung Chen, C. Piermarocchi, L. J. Sham, D. Gammon, and D. G. Steel. Theory of quantum optical control of a single spin in a quantum dot. *Physical Review B (Condensed Matter and Materials Physics)*, 69(7):75320 – 1, 2004.

[48] A. S. Bracker, E. A. Stinaff, D. Gammon, M. E. Ware, J. G. Tischler, A. Shabaev, Al. L. Efros, D. Park, D. Gershoni, V. L. Korenev, and I. A. Merkulov. Optical pumping of the electronic and nuclear spin of single charge-tunable quantum dots. *Physical Review Letters*, 94(4):047402 – 4, 2005.

[49] A. Abragam. *Principles of Nuclear Magnetism*. Clarendon Press, 1961.

[50] J. C. PHILLIPS. Ionicity of the chemical bond in crystals. *Reviews of Modern Physics*, 42(3):317 – 54, 1970.

[51] J. C. PHILLIPS. Ionicity of the chemical bond in crystals. *Reviews of Modern Physics*, 42(3):317 – 54, 1970.

[52] D. Paget, G. Lampel, B. Sapoval, and V. I. Safarov. Low field electron-nuclear spin coupling in gallium arsenide under optical pumping conditions. *Physical Review B (Solid State)*, 15(12):5780 – 96, 1977.

[53] R. E. Watson and L. H. Bennett. Calculation of atomic hyperfine-field coupling constants. *Physical Review B (Solid State)*, 15(1):502 – 3, 1977.

[54] K. H. Hellwege. *Landolt-Boörnstein Numerical Data and Functional Relationships in Science and Technology*, volume 17a. Springer.

[55] Zeeman spin splittings in semiconductor nanostructures.

[56] T. C. DAMEN, L. VINA, J. E. CUNNINGHAM, J. SHAH, and L. J. SHAM. Subpicosecond spin relaxation dynamics of excitons and free carriers in gaas quantum wells. *Physical Review Letters*, 67(24):3432 – 5, DEC 1991.

[57] T. C. DAMEN, K. LEO, J. SHAH, and J. E. CUNNINGHAM. Spin relaxation and thermalization of excitons in gaas quantum wells. *Applied Physics Letters*, 58(17):1902 – 4, APR 1991.

[58] J.J. Sakurai. *Modern Quantum Mechanics*, page 333. Addison Wesley Longman, revised edition edition, 1994.

[59] David J. Griffiths. *Introduction to Quantum Mechanics*, page 150. Prentice Hall, 1st edition, 1994.

[60] S. Cortez, O. Krebs, S. Laurent, M. Senes, X. Marie, P. Voisin, R. Ferreira, G. Bastard, J. M. Gerard, and T. Amand. Optically driven spin memory in n-doped inas-gaas quantum dots. *Physical Review Letters*, 89(20):207401 – 4, NOV 2002.

[61] D. Gammon, S. W. Brown, E. S. Snow, T. A. Kennedy, D. S. Katzer, and D. Park. Nuclear spectroscopy in single quantum dots: nanoscopic raman scattering and nuclear magnetic resonance. *Science*, 277(5322):85 – 8, JUL 1997.

[62] M. GRUNDMANN, O. STIER, and D. BIMBERG. Inas/gaas pyramidal quantum dots: strain distribution, optical phonons, and electronic structure. *Physical Review B (Condensed Matter)*, 52(16):11969 – 81, OCT 1995.

[63] D. J. Guerrier and R. T. Harley. Calibration of strain vs nuclear quadrupole splitting in ill-v quantum wells. *Applied Physics Letters*, 70(13):1739 – 41, MAR 1997.

[64] R. K. Sundfors. Experimental gradient-elastic tensors and chemical bonding in iii-v semiconductors. *Physical Review B (Solid State)*, 10(10):4244 – 52, 1974.

[65] J. D. WEINSTEIN and K. G. LIBBRECHT. Microscopic magnetic traps for neutral atoms. *Physical Review A (Atomic, Molecular, and Optical Physics)*, 52(5):4004 – 9, NOV 1995.

[66] V. Vuletic, T. Fischer, M. Praeger, T. W. Hansch, and C. Zimmermann. Microscopic magnetic quadrupole trap for neutral atoms with extreme adiabatic compression. *Physical Review Letters*, 80(8):1634 – 7, Feb 1998.

[67] J. Reichel, W. Hansell, and T. W. Hansch. Atomic micromanipulation with magnetic surface traps. *Physical Review Letters*, 83(17):3398 – 401, OCT 1999.

[68] M. Drndic, K. S. Johnson, J. H. Thywissen, M. Prentiss, and R. M. Westervelt. Micro-electromagnets for atom manipulation. *APPLIED PHYSICS LETTERS*, 72(22):2906 – 2908, JUN 1998.

[69] A. MATULIS, F. M. PEETERS, and P. VASILOPOULOS. Wave-vector-dependent tunneling through magnetic barriers. *Physical Review Letters*, 72(10):1518 – 21, MAR 1994.

[70] I. S. Ibrahim and F. M. Peeters. Two-dimensional electrons in lateral magnetic superlattices. *Physical Review B (Condensed Matter)*, 52(24):17321 – 34, DEC 1995.

[71] K. Tsubaki. Longitudinal magnetoresistance in magnetic barrier systems. *PHYSICA B*, 258:392 – 396, DEC 1998.

[72] V. STEPANKIN. Magnetically aligned polycrystalline dysprosium as ultimate saturation ferromagnet for high magnetic field polepieces. *Physica B*, 211(1/4):345 – 7, MAY 1995.

[73] A. V. ANDRIANOV, Y. P. GAIDUKOV, A. N. VASILEV, and E. FAWCETT. The magnetic phase diagrams of dysprosium. *Journal of Magnetism and Magnetic Materials*, 97(1/3):246 – 50, Jun 1991.

[74] M. T. Alkhafaji and N. Ali. Magnetic phase diagram of dysprosium. *Journal of Alloys and Compounds*, 250(1/2):659 – 61, Mar 1997.

[75] C. P. Slichter. *Principles of Magnetic Resonance*. Springer,, third edition, 1990.

[76] A. MATSUTANI, F. KOYAMA, and K. IGA. 3-dimensional electron-probe roughness analysis of inp sidewalls processed by reactive ion-beam etching. *APPLIED PHYSICS LETTERS*, 66(1):64 – 66, JAN 1995.

[77] Chih-Wen Chen. *Magnetism and Metallurgy of Soft Magnetic Materials*, page 100. Dover Books, 1st edition, 1986.

[78] Naushad Ali M.T. Alkhafaji. Magnetic phase diagram of dysprosium. *Journal of Alloys and Compounds*, 250:659–661, 1997.

[79] V. A. SHCHUKIN, N. N. LEDENTSOV, P. S. KOPEV, and D. BIMBERG. Spontaneous ordering of arrays of coherent strained islands. *Physical Review Letters*, 75(16):2968 – 71, OCT 1995.

[80] C. Heyn and C. Dumat. Formation and size evolution of self-assembled quantum dots. *Journal of Crystal Growth*, 227/228:990 – 4, July 2001.

[81] C. Heyn. Critical coverage for strain-induced formation of inas quantum dots. *Physical Review B (Condensed Matter and Materials Physics)*, 64(16):165306 – 7, OCT 2001.

[82] M. Bayer, S. N. Walck, T. L. Reinecke, and A. Forchel. Exciton binding energies and diamagnetic shifts in semiconductor quantum wires and quantum dots. *Physical Review B (Condensed Matter)*, 57(11):6584 – 91, MAR 1998.

[83] P. P. Paskov, P. O. Holtz, B. Monemar, J. M. Garcia, W. V. Schoenfeld, and P. M. Petroff. Magnetoluminescence of highly excited inas/gaas self-assembled quantum dots. *Physical Review B (Condensed Matter)*, 62(11):7344 – 9, SEP 2000.

[84] P. D. Wang, J. L. Merz, S. Fafard, R. Leon, D. Leonard, G. MEdeirosRibeiro, M. Oestreich, P. M. Petroff, K. Uchida, N. Miura, H. Akiyama, and H. Sakaki. Magnetoluminescence studies of insub yalsub 1-yas self-assembled quantum dots in alsub xgasub 1-xas matrices. *Physical Review B (Condensed Matter)*, 53(24):16458 – 61, JUN 1996.

[85] D. Gammon, A. L. Efros, T. A. Kennedy, M. Rosen, D. S. Katzer, D. Park, S. W. Brown, V. L. Korenev, and I. A. Merkulov. Electron and nuclear spin interactions in the optical spectra of single gaas quantum dots. *Physical Review Letters*, 86(22):5176 – 9, May 2001.

[86] P. W. Shor. Algorithms for quantum computation: discrete logarithms and factoring. In *Proceedings, 35th Annual Symposium on Foundations of Computer Science*. IEEE Press, 1994.

[87] P. W. SHOR. Scheme for reducing decoherence in quantum computer memory. *Physical Review A (Atomic, Molecular, and Optical Physics)*, 52(4):R2493 – 6, OCT 1995.

[88] R. Schack and C. M. Caves. Classical model for bulk-ensemble nmr quantum computation. *Physical Review A (Atomic, Molecular, and Optical Physics)*, 60(6):4354 – 62, DEC 1999.

[89] E. Knill, I. Chuang, and R. Laflamme. Effective pure states for bulk quantum computation. *Physical Review A (Atomic, Molecular, and Optical Physics)*, 57(5):3348 – 63, MAY 1998.

[90] S. L. Braunstein, C. M. Caves, R. Jozsa, N. Linden, S. Popescu, and R. Schack. Separability of very noisy mixed states and implications for nmr quantum computing. *Physical Review Letters*, 83(5):1054 – 7, AUG 1999.

[91] W. S. Warren. The usefulness of NMR quantum computing. *Science*, 277:1688, 1997.

[92] J. R. Goldman, T. D. Ladd, F. Yamaguchi, and Y.Yamamoto. Magnet designs for a crystal-lattice quantum computer. *Appl. Phys. A: Mater. Sci. Process.*, 71:11.

[93] D. W. Leung, I. L. Chuang, F. Yamaguchi, and Y. Yamamoto. Efficient implementation of coupled logic gates for quantum computation. *Physical Review A (Atomic, Molecular, and Optical Physics)*, 61(4):042310 – 7, APR 2000.

[94] M. Mehring U. Haeberlin. *High Resolution NMR in Solids: Selective Averaging.* Academic Press, 1976.

[95] S. LLOYD. A potentially realizable quantum computer. *Science*, 261(5128):1569 – 71, Sep 1993.

[96] K. M. Itoh and E. E. Haller. Isotopically engineered semiconductors - new media for the investigation of nuclear spin related effects in solids. *Physica E*, 10(1/3):463 – 6, May 2001.

[97] G. LAMPEL. Nuclear dynamic polarization by optical electronic saturation and optical pumping in semiconductors. *PHYSICAL REVIEW LETTERS*, 20(10):491, 1968.

[98] D. RUGAR, O. ZUGER, S. HOEN, C. S. YANNONI, H. M. VIETH, and R. D. KENDRICK. Force detection of nuclear magnetic resonance. *Science*, 264(5165):1560 – 3, Jun 1994.

[99] G. P. Berman, G. D. Doolen, P. C. Hammel, and V. I. Tsifrinovich. Solid-state nuclear-spin quantum computer based on magnetic resonance force microscopy. *Physical Review B (Condensed Matter)*, 61(21):14694 – 9, JUN 2000.

[100] Editor E. H. C. Parker. *The Technology and Physics of Molecular Beam Epitaxy.* Plenum Press, 1985.

[101] 7th Edition Introduction to Solid State Physics. *Charles Kittel*, page 100. John Wiley and Sons, Inc, 7th edition, 1996.

[102] 7th Edition Introduction to Solid State Physics. *Charles Kittel*, page 200. John Wiley and Sons, Inc, 7th edition, 1996.

[103] D. GAMMON, E. S. SNOW, and D. S. KATZER. Excited state spectroscopy of excitons in single quantum dots. *Applied Physics Letters*, 67(16):2391 – 3, OCT 1995.

[104] S. W. Brown, T. A. Kennedy, D. Gammon, and E. S. Snow. Spectrally resolved overhauser shifts in single gaas/alsub xgasub 1-xas quantum dots. *Physical Review B (Condensed Matter)*, 54(24):R17339 – 42, 1996.

[105] D. Gammon, E. S. Snow, and D. S. Katzer. Naturally formed gaas quantum dots. *Surface Science*, 361/362:814 – 17, 1996.

[106] D. Gammon, E. S. Snow, and B. V. Shanabrook. Optical spectroscopy of a single naturally formed gaas quantum dot., 1996.

[107] D. Gammon, E. S. Snow, B. V. Shanabrook, S. W. Brown, T. A. Kennedy, D. S. Katzer, and D. Park. Single quantum dot spectroscopy., 1996.

[108] S. W. Brown, T. A. Kennedy, and D. Gammon. Optical nmr from single quantum dots., 1997.

[109] D. Gammon. High-resolution spectroscopy of individual quantum dots in wells. *MRS Bulletin*, 23(2):44 – 8, Feb 1998.

[110] G. Chen, N. H. Bonadeo, E. A. Tabak, D. Gammon, D. S. Katzer, D. Park, and D. G. Steel. Magneto-optical studies of excitons in single gaas quantum dots., 1999.

[111] D. Gammon and D. G. Steel. Optical studies of single quantum dots. *Physics Today*, 55(10):36 – 41, October 2002.

[112] R. I. Dzhioev, K. V. Kavokin, V. L. Korenev, M. V. Lazarev, B. Ya. Meltser, M. N. Stepanova, B. P. Zakharchenya, D. Gammon, and D. S. Katzer. Low-temperature spin relaxation in n-type gaas. *Physical Review B (Condensed Matter and Materials Physics)*, 66(24):245204 – 1, 2002.

[113] A. S. Bracker, D. Gammon, J. G. Tischler, M. E. Ware, A. L. Efros, and D. Gershoni. Hyperfine interactions in a charged quantum dot., 2003.

[114] A. K. Paravastu. Optical polarization of nuclear spins in gaas. 69:075203, 2004.

[115] A. K. Paravastu, P. Coles, T. D. Ladd, R. S. Maxwell, and J. A. Reimer. Photocurrent-modulated optical nuclear polarization in bulk GaAs. 2005. in preparation.

[116] M. Bayer, G. Ortner, O. Stern, A. Kuther, A. A. Gorbunov, A. Forchel, P. Hawrylak, S. Fafard, K. Hinzer, T. L. Reinecke, S. N. Walck, J. P. Reithmaier, F. Klopf, and F. Schafer. Fine structure of neutral and charged excitons in self-assembled in(ga)as/(al)gaas quantum dots. *Physical Review B (Condensed Matter and Materials Physics)*, 65(19):195315 – 23, MAY 2002.

[117] M. Bayer, A. Kuther, A. Forchel, A. Gorbunov, V. B. Timofeev, F. Schafer, J. P. Reithmaier, T. L. Reinecke, and S. N. Walck. Electron and hole g factors and exchange interaction from studies of the exciton fine structure in insub 0.60gasub 0.40as quantum dots. *Physical Review Letters*, 82(8):1748 – 51, FEB 1999.

[118] R. I. Dzhioev, V. L. Korenev, B. P. Zakharchenya, D. Gammon, A. S. Bracker, J. G. Tischler, and D. S. Katzer. Optical orientation and the hanle effect of neutral and negatively charged excitons in gaas/alsub xgasub 1-xas quantum wells. *Physical Review B (Condensed Matter and Materials Physics)*, 66(15):153409 – 1, OCT 2002.

[119] J. G. Tischler, A. S. Bracker, D. Gammon, and D. Park. Fine structure of trions and excitons in single gaas quantum dots. *Physical Review B (Condensed Matter and Materials Physics)*, 66(8):81310 – 1, 2002.

[120] J. G. Tischler, A. S. Bracker, and D. Gammon. Optical spectroscopy of single trions., 2002.

[121] J. G. Tischler, A. S. Bracker, and D. Gammon. Magneto-optical spectroscopy of single trions., 2003.

[122] A. S. Bracker, J. G. Tischler, V. L. Korenev, and D. Gammon. Polarized electrons, trions, and nuclei in charged quantum dots. *Physica Status Solidi B*, 238(2):266 – 72, JUL 2003.

[123] M. E. Ware, A. Bracker, D. Gammon, and D. Gershoni. Polarization spectroscopy of charged single self-assembled quantum dots., 2004.

[124] A. S. Bracker, J. G. Tischler, D. Gammon, and B. Z. Nosho. Spectroscopy and mechanical modification of single strain-induced quantum dots. *Physica Status Solidi B*, 224(1):133 – 7, MAR 2001.

[125] T. Yokoi, S. Adachi, H. Sasakura, S. Muto, H. Z. Song, T. Usuki, and S. Hirose. Polarization-dependent shift in excitonic zeeman splitting of self-assembled insub 0.75alsub 0.25as/alsub 0.3gasub 0.7as quantum dots. *Physical Review B (Condensed Matter and Materials Physics)*, 71(4):41307 – 1, 2005.

[126] C. R. Bowers. Microscopic interpretation of optically pumped nmr signals in gaas. *Solid State Nuclear Magnetic Resonance*, 11(1/2):11 – 20, MAR 1998.

[127] John A. McNeil and W. Gilbert Clark. Nuclear quadrupolar spin-lattice relaxation in some iii-v compounds. *Physical Review B (Condensed Matter)*, 13(11):4705 – 13, JUN 1976.

[128] D. V. Regelman, E. Dekel, D. Gershoni, E. Ehrenfreund, A. J. Williamson, J. Shumway, A. Zunger, W. V. Schoenfeld, and P. M. Petroff. Optical spectroscopy of single quantum dots at tunable positive, neutral, and negative charge states. *Physical Review B (Condensed Matter and Materials Physics)*, 64(16):165301 – 7, OCT 2001.

[129] E. Dekel, D. V. Regelman, D. Gershoni, E. Ehrenfreund, W. V. Schoenfeld, and P. M. Petroff. Radiative lifetimes of single excitons in semiconductor quantum dots-manifestation of the spatial coherence effect. *Solid State Communications*, 117(7):395 – 400, Jan 2001.

[130] D. V. Regelman, D. Gershoni, W. V. Schoenfeld, and P. M. Petroff. Charging and switching the charge sign of single semiconductor quantum dots by all optical means., 2001.

[131] D. V. Regelman, E. Dekel, D. Gershoni, W. V. Schoenfeld, and P. M. Petroff. Dynamics of excitons in single semiconductor quantum dots probed by time-resolved optical spectroscopy. *Physica Status Solidi B*, 224(2):343 – 8, MAR 2001.

[132] A. C. Johnson, J. R. Petta, J. M. Taylor, A. Yacoby, M. D. Lukin, C. M. Marcus, M. P. Hanson, and A. C. Gossard. Triplet-singlet spin relaxation via nuclei in a double quantum dot. *Nature*, 435(7044):925 – 928, Jun 2005.

[133]

[134] T. D. Ladd, D. Maryenko, Y. Yamamoto, E. Abe, and K. M. Itoh. Coherence time of decoupled nuclear spins in silicon. 71:14401, 2005.

[135] B. Cowan. *Nuclear Magnetic Resonance and Relaxation*. Cambridge, 1997.

[136] E. Fukushima and S. B. W. Roeder. *Experimental Pulse* NMR*: A Nuts and Bolts Approach*. Addison-Wesley, 1981.

[137] D. Deutsch. Quantum theory, the Church-Turing principle, and the universal quantum computer. *Proc. R. Soc. London A*, 400:97, 1985.

[138] A. M. Turing. On computable numbers, with an application to the Entscheidungsproblem. *Proc. Lond. Math. Soc. 2*, 42:230, 1936.

[139]

[140]

[141] Q. A. TURCHETTE, C. J. HOOD, W. LANGE, H. MABUCHI, and H. J. KIMBLE. Measurement of conditional phase shifts for quantum logic. *Physical Review Letters*, 75(25):4710 – 13, DEC 1995.

[142] A. Sørensen and K. Mølmer. Quantum computation with ions in thermal motion. 82:1971, 1999.

[143] C. Monroe, D. M. Meekhof, B. E. King, W. M. Itano, and D. J. Wineland. Demonstration of a fundamental quantum logic gate. 75:4714, 1995.

[144] P. T. H. Fisk. *IEEE Trans. Instrum. Measurement*, 44:113, 1995.

[145] R.J. Rafac, B.C. Young, J.A. Beall, W. M. Itano, D. J. Wineland, and J. C. Bergquist. Sub-dekahertz ultraviolet spectroscopy of $^{199}Hg^{+}$. 85:2462, 2000.

[146] S.Bize. Testing the stability of fundamental constants with the $^{199}Hg^{+}$ single-ion optical clock. 90:150802, 2003.

[147] A. M. Steane and D. M. Lucas. Quantum computing with trapped ions, atoms and light. *Fortschr. Phys.*, 48:839, 2000.

[148] D.Liebfried. Experimental demonstration of a robust, high-fidelity geometric two ion-qubit phase gate. *Nature*, 422:412, 2003.

[149] F.Schmidt-Kaler. Realization of the cirac-zoller cnot quantum gate. *Nature*, 422:408, 2003.

[150] F.Schmidt-Kaler. The coherence of qubits based on single Ca^{+} ions. *J. Phys. B: At. Mol. Opt. Phys.*, 36:623, 2003.

[151] S.Gulde. Implementation of the Deutsch-Jozsa algorithm on an ion-trap quantum computer. *Nature*, 421:48, 2003.

[152] L.-M. Duan, M. Lukin, J. I. Cirac, and P. Zoller. Long-distance quantum communication with atomic ensembles and linear optics. *Nature*, 414:413, 2001.

[153] B. B. Blinov, D. L. Moehring, L.-M. Duan, and C. Monroe. Observation of entanglement between a single trapped atom and a single photon. *Nature*, 428:153, 2004.

[154] 1 M. A. Rowe 1 C. A. Sackett 1 W. M. Itano 1 C. Monroe 2 D. J. Wineland D. Kielpinski, 1* V. Meyer. A decoherence-free quantum memory using trapped ions. *Science*.

[155] M. Riebe H. Hffner W. Hnsel S. Gulde C. Becher J. Eschner F. Schmidt-Kaler C. F. Roos, G. P. T. Lancaster and R. Blatt. Bell states of atoms with ultralong lifetimes and their tomographic state analysis. 92:220402, 2004.

[156] N. A. Gershenfeld and I. L. Chuang. Bulk spin-resonance quantum computation. *Science*, 275:350, 1997.

[157] D. G. Cory, A. F. Fahmy, and T. F. Havel. Ensemble quantum computing by NMR spectroscopy. *Proc. Natl. Acad. Sci.*, 94:1634, 1997.

[158] I. L. Chuang, L. M. K. Vandersypen, X. Zhou, D. W. Leung, and S. Lloyd. Experimental realization of a quantum algorithm. *Nature*, 393:143, 1998.

[159] L. M. K. Vandersypen, C. S. Yannoni, M. H. Sherwood, and I. L. Chuang. Realization of logically labeled effective pure states for bulk quantum computation. 83:3085, 1999.

[160] L. M. K.Vandersypen. Experimental realization of Shor's quantum factoring algorithm using nuclear magnetic resonance. *Nature*, 414:883, 2001.

[161] E. Knill, I. Chuang, and R. Laflamme. Effective pure states for bulk quantum computation. 57:3348, 1998.

[162] D. E. Chang, L. M. K. Vandersypen, and M. Steffen. NMR implementation of a building block for scalable quantum computation. 338:337, 2001.

[163] P. Hübler, J. Bargon, and S. J. Glaser. Nuclear magnetic resonance quantum computing exploiting the pure spin state of *para* hydrogen. 113:2056, 2000.

[164] A. S. Verhulst, O. Liivak, M. H. Sherwood, H. M. Vieth, and I. L. Chuang. Non-thermal nuclear magnetic resonance quantum computing using hyperpolarized xenon. 79:2480, 2001.

[165] S. L. Braunstein. Separability of very noisy mixed states and implications for NMR quantum computing. 84:1054, 1990.

[166] N. C. Menicucci and C. M. Caves. Local realistic model for the dynamics of bulk-ensemble NMR information processing. 88:167901, 2002.

[167] N. Linden and S. Popescu. Good dynamics versus bad kinematics: Is entanglement needed for quantum computation? 87:047901, 2001.

[168] R. Schack and C. M. Caves. Classical model for bulk-ensemble NMR quantum computation. 60:4354.

[169] D. P. DiVincenzo. Quantum computation. *Science*, 270:255, 1995.

[170] F. Yamaguchi and Y. Yamamoto. Crystal lattice quantum computer. *Applied Physics A*, 68:1, 1999.

[171] T. D. Ladd, J. R. Goldman, A. Dâna, F. Yamaguchi, and Y. Yamamoto. Quantum computation in a one-dimensional crystal lattice with nmr force microscopy. eprint: quant-ph/0009122, 2000.

[172] V. Privman, I. D. Vagner, and G. Kventsel. Quantum computation in quantum-hall systems. *Phys. Lett. A*, 239:141, 1998.

[173] D. Mozyrsky, V. Privman, and M. L. Glasser. Indirect interaction of solid-state qubits via two-dimensional electron gas. 86:5112, 2001.

[174] D. Mozyrsky, V. Privman, and I. D. Vagner. Nuclear-spin qubit dephasing time in the integer quantum Hall effect regime. 63:85313, 2001.

[175] R. G. Mani, W. B. Johnson, and V. Narayanamurti. Nuclear spin based quantum information processing at high magnetic fields. *Nanotechnology*, 14:515, 2003.

[176] M. Mehring, J. Mende, and W. Scherer. e-print: quant-ph/0209137.

[177] B.E. Kane. A silicon-based nuclear spin quantum computer. *Nature*, 393:133, 1998.

[178] T. M. Buehler, D. J. Reilly, R. Brenner, A. R. Hamilton, A.S. Dzurak, and R.G. Clark. Correlated charge detection for readout of a solid-state quantum computer. *Appl. Phys. Lett.*, 82:577, 2003.

[179]

[180] G. D. Sanders, K. W. Kim, and W. C. Holton. Optically driven quantum-dot quantum computer. 60:4146, 1999.

[181] G. D. Sanders, K. W. Kim, and W. C. Holton. Scalable solid-state quantum computer based on quantum dot pillar structures. 60:4146, 1999.

[182] J. H. Reina, L. Quiroga, and N. F. Johnson. Quantum entanglement and information processing via excitons in optically driven quantum dots. 62:012305, 2000.

[183] G. Chen, N. H. Bonadeo, D. G. Steel, D. Gammon, D. S. Katzer, D. Park, and L. J. Sham. Optically induced entanglement of excitons in a single quantum dot. *Science*, 289:1906, 2000.

[184] P. Chen, C. Piermarocchi, L. J. Sham, D. Gammon, and D. G. Steel. Theory of quantum optical control of a single spin in a quantum dot. 69:75320, 2004.

[185] D. Loss and D. P. DiVincenzo. Quantum computation with quantum dots. 57:120, 1998.

[186] D. Loss, G. Burkard, and D.P. DiVincenzo. Coupled quantum dots as quantum gates. 59:2070, 1999.

[187] T. Tanamoto. Quantum gates by coupled asymmetric quantum dots and controlled-not-gate operation. 61:022305, 2000.

[188] C. H. W. Barnes, J. M. Shilton, and A. M. Robinson. Quantum computation using electrons trapped by surface acoustic waves. 62:8410, 2000.

[189] S. Bandyopadhyay. Self-assembled nanoelectronic quantum computer based on the Rashba effect in quantum dots. 61:13813, 2000.

[190] V. Cerletti, W. A. Coish, O. Gywat, and D. Loss. Recipes for spin-based quantum computing. *Nanotechnology*, 16:R27, 2005.

[191] B. E. Kane, N. S. McAlpine, A. S. Dzurak, R. G. Clark, G. J. Milburn, H. B. Sun, and H. Wiseman. Single-spin measurement using single-electron transistors to probe two-electron systems. 61:2961, 2000.

[192] R. Vrijen, E. Yablonovitch, K. Wang, H. W. Jiang, A. Balandin, V. Roychowdhury, T. Mor, and D. DiVincenzo. Electron-spin-resonance transistors for quantum computing in silicon-germanium heterostructures. 62:012306, 2000.

[193] G. P. Berman, G. D. Doolen, P. C. Hammel, and V. I. Tsifrinovich. Solid-state nuclear-spin quantum computer based on magnetic resonance force microscopy. 61:14694, 2000.

[194] S.A. Empedocles, D.J. Norris, and M. G. Bawendi. Photoluminescence spectroscopy of single cdse nanocrystallite quantum dots. 77:3873, 1996.

[195] N.H.Bonadeo. Coherent optical control of the quantum state of a single quantum dot. *Science*, 282:1473–1476, 1998.

[196] P.Borri. Ultralong dephasing time in InGaAs quantum dots. 87:157401, 2001.

[197] P. Palinginis, S. Tavenner, M. Lonergan, and H. Wang. Spectral hole burning and zero phonon linewidth in semiconductor nanocrystals. 67:201307, 2003.

[198] M.Bayer. Coupling and entangling of quantum states in quantum dot molecules. *Science*, 291:451–453, 2001.

[199] X.Li. An all-optical quantum gate in a semiconductor quantum dot. *Science*, 301:809–811, 2003.

[200] M.S. Sherwin, A. Imamoḡlu, and T. Montroy. Quantum computation with quantum dots and terahertz cavity quantum electrodynamics. 60:3508, 1999.

[201] A. Imamoḡlu, D.D. Awschalom, G. Burkard, D.P. DiVincenzo, D. Loss, M. Shermin, and A. Small. Quantum information processing using quantum dot spins and cavity QED. 83:4204, 1999.

[202] A.M. Tyryshkin, S. A. Lyon, A. V. Astashkin, and A. M. Raitsimring. Electron spin-relaxation times of phosphorous donors in silicon. 68:193207, 2003.

[203] A. M. Tyrishkin, S. A. Lyon, W. Jantsch, and F. Schäffler. Spin manipulation of free two-dimensional electrons in Si/SiGe quantum wells. 94:126802, 2005.

[204] R. De Sousa, J. D. Delgado, and S. Das Sarma. Silicon quantum computation based on magnetic dipolar coupling. 70:052304, 2004.

[205] M. S. Shahriar, P. R. Hemmer, S. Lloyd, P. S. Bhatia, and A. E. Craig. Solid-state quantum computing using spectral holes. 66:032301, 2002.

[206] F. Jelezko, T. Gaebel, I. Popa, M. Domhan, A. Gruber, and J. Wrachtrup. Observation of coherent oscillation of a single nuclear spin and realization of a two-qubit conditional quantum gate. 93:130501, 2004.

[207] C. Kurtziefer, S. Mayer, P. Zarda, and H. Weinfurter. Stable solid-state source of single photons. 85:290, 2000.

[208] D. V. Averin. Adiabatic quantum computation with Cooper pairs. *Solid State Communications*, 105:659, 1998.

[209] L. B. Ioffe, V. B. Geshkenbein, M. V. Feigel'man, A. L. Fauchere, and Gy Blatter. Environmentally decoupled sds-wave Josephson junctions for quantum computing. *Nature*, 398:679, 1999.

[210] Y. Makhlin, G. Schön, and A. Shnirman. Josephson-junction qubits with controlled couplings. *Nature*, 398:305, 1999.

[211] Y. Nakamura, Yu. A. Pashkin, and J.S. Tsai. Coherent control of macroscopic quantum states in a single-Cooper-pair box. *Nature*, 398:786, 1999.

[212] Yu. A.Pashkin. Quantum oscillations in two coupled charge qubits. *Nature*, 421:823–826, 2003.

[213] D.Vion. Manipulating the quantum state of an electrical circuit. *Science*, 296:886–889, 2002.

[214] T. Yamamoto, Yu. A. Pashkin, O. Astaflev, Y. Nakamura, and J. S. Tsai. Demonstration of conditional gate operation using superconducting charge qubits. *Nature*, 425:941, 2003.

[215] D. I. Schuster. AC stark shift and dephasing of a superconducting qubit strongly coupled to a cavity field. 94:123602, 2005.

[216] L. Tian, P. Rabl, R. Blatt, and P. Zoller. Interfacing quantum-optical and solid-state qubits. 92:247902, 2004.

[217] I. Chiorescu, Y. Nakamura, C.J.P.M. Harmans, and J.E. Mooij. Coherent quantum dynamics of a superconducting flux qubit. *Science*, 299:1869–1871, 2003.

[218] J.E.Mooij. Josephson persistent-current qubit. *Science*, 285:1036, 1999.

[219] E.Il'ichev. Continuous monitoring of Rabi oscillations in a Josephson flux qubit. 91:097906, 2003.

[220] J.M. Martinis, S. Nam, J. Aumentado, and C. Urbina. Rabi oscillations in a large Josephson-junction qubit. 89:117901, 2002.

[221] Y. Yu, S. Han, X. Chu, S-I. Chu, and Z. Wang. Coherent temporal oscillations of macroscopic quantum states in a Josephson junction. *Science*, 296:889–892, 2002.

[222] A. J.Berkley. Entangled macroscopic quantum states in two superconducting qubits. *Science*, 300:1548–1550, 2003.

[223] P.M. Platzman and M. I. Dykman. Quantum computing with electrons floating on liquid helium. *Science*, 284:1967, 1999.

[224] J.A. Gupta, D.D. Awschalom, X. Peng, and A.P. Alizisatos. Spin coherence in semiconductor quantum dots. 59:10421, 1999.

[225] R. J. Epstein, D. T. Fuchs, W. V. Schoenfield, P. M. Petroff, and D. D. Awschalom. Hanle effect measurements of spin lifetimes in InAs self-assembled quantum dots. 78:733, 2001.

[226] E. Knill, R. Laflamme, and G. J. Milburn. A scheme for efficient quantum computation with linear optics. *Nature*, 409:46, 2001.

[227] D. Gottesman and I. L. Chuang. Demonstrating the viability of universal quantum computation using teleportation and single-qubit operations. *Nature*, 402:390, 1999.

[228] R. M. Gingrich, P. Kok, H. Lee, F. Vatan, and J. P. Dowling. All linear optical quantum memory based on quantum error correction. 91:217901, 2003.